1.2 QUANTUM DYNAMICS DIVISION

Gerhard Rempe

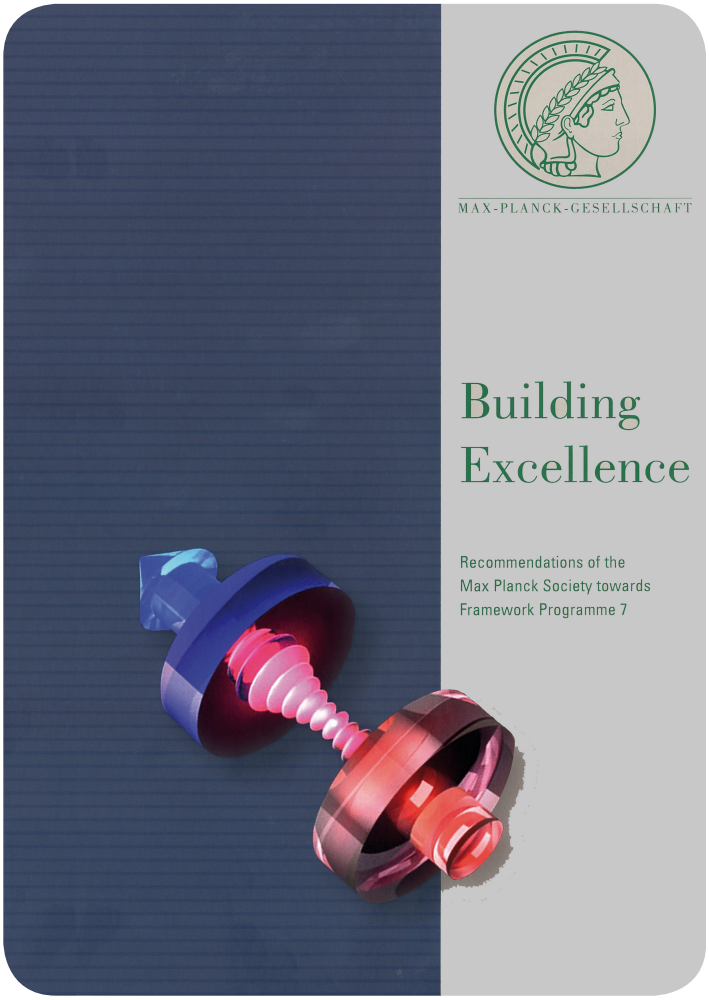

SCIENTIFIC STAFF
S. Dürr, A. Kuhn*, P.W.H. Pinkse
(*now at Oxford University)

POSTDOCS
L.D. van Buuren, K. Murr, S.C. Webster

PH.D. CANDIDATES
D.M. Bauer, J. Bochmann, M. Hijlkema, T. Junglen*, A. Kubanek, T. Legero*, P. Maunz*, M. Motsch, S. Nußmann*, T. Puppe, T. Rieger, I. Schuster, H. Specht, N. Syassen, T. Volz, B. Weber, T. Wilk
(* received Ph.D. during report period)

DIPLOMA CANDIDATES
J. Almer, C. Erbel, A. Grothe*, E. Hansis*, G. Langfahl, S. Pohle, H. Specht*, S. Teichmann*, P. Windpassinger*, M. Zeppenfeld
(* received Diploma during report period)

SCIENTIFIC COLLABORATORS
J. Bulthuis (Amsterdam/NL), C. Foot (Oxford/UK), H. Friedrich (Munich/DE), S.A. Rangwala (Bangalore/IN), S. Kokkelmans (Eindhoven/NL), T. Köhler (Oxford/UK), B.J. Verhaar (Eindhoven/NL), D. Vitali (Camerino/IT)

JUNIOR RESEARCH GROUP
T. Schätz (leader), A. Friedenauer (Ph.D.), S. Kahra (Ph.D.), H. Schmitz (Ph.D.), G. Leschhorn (Diploma) L. Petersen (Diploma)

1.2.1 SUMMARY OF SCIENTIFIC ACTIVITIES

The last two years from mid 2004 to mid 2006 have seen a large number of scientific achievements in all the different research fields cultivated in the Quantum Dynamics Division, namely

- Bose-Einstein Condensation,
- Cavity Quantum Electrodynamics,
- Quantum Information Processing,
- Cold Molecules.

Our research is documented in about 25 publications, more than 100 oral presentations and nearly 50 posters.

Success is also documented by the fact that Axel Kuhn has been offered a new position at the University of Oxford in combination with Christ College. He accepted this honourable offer in April 2006 and is now setting up his own research group. We all thank him very much for many successful years with us, and wish him all the best for his future activities as a researcher and teacher at one of the best universities worldwide.

Another change concerns the establishment of a Junior Research Group headed by Tobias Schätz, who concentrates his activities on

- Quantum Simulation with Trapped Ions

He joined us in October 2004 and is mainly funded by the German Science Foundation (DFG) in the framework of the Emmy-Noether Programme, with support from the Max-Planck Institute for Quantum Optics and the Max-Planck Society. We all wish him good luck in setting up his new experiments.

Another very successful research programme, aimed to understand the light forces a single atom experiences in a high-finesse optical resonator, is pursued by Karim Murr who joined us in September 2004. His theoretical expertise turned out to be extremely valuable in understanding the various experimental results in two of our cavity experiments.

Last but not least, Laurens van Buuren joined us in October 2005, bringing expertise in buffer-gas cooling of neutral particles to the group. He is presently setting up a new generation of experiments with the goal to produce a dense sample of electrically trapped cold polar molecules.

Title: Cooling of an Atom in an Optical Resonator

The following pages briefly summarize the most interesting results and research topics. A selection of reprints can be found at the end.

1.2.1.1 BOSE-EINSTEIN CONDENSATION

The creation of ultracold molecules with Feshbach resonances in 2003 opened up new perspectives in the field of ultracold gases [1]. Our work in this field focussed on two topics. The first one concerns the dissociation of the Feshbach molecules into atom pairs. The second one addresses the question whether a Mott insulator of ultracold molecules can be created in an optical lattice. In addition, we measured three-body recombination in the vicinity of a Feshbach resonance.

Dissociation of Feshbach Molecules

Ultracold atoms of a Bose-Einstein condensate can be associated to molecules in a controlled way by means of a magnetically tuneable Feshbach resonance. Such a Feshbach resonance occurs when the energy of an atom pair equals the energy of a (highly excited) vibrational state of the dimer, provided there is a coupling between the atomic state and the molecular state. If the atomic state and the molecular state have a different spin configuration, the Zeeman effect allows one to tune the two states with respect to each other, and thus tune them into resonance. By slowly changing the magnetic field over the resonance, molecules can be adiabatically turned into atoms.

After associating ultracold molecules with a magnetic-field ramp across a Feshbach resonance, the molecules can be dissociated by ramping the magnetic field back across the (same) Feshbach resonance. Above the Feshbach resonance, the molecular state is resonantly coupled to a continuum of unbound atom-pair states. This leads to spontaneous dissociation of the molecules and thus to a decay of the molecular sample. A time- or energy-resolved measurement of the dissociation process can be used to experimentally determine the width of the Feshbach resonance [2]. This technique works particularly well for very narrow Feshbach resonances, as in this case the decay of the molecules is relatively slow. We emphasize that other techniques for the determination of the width fail, e.g., because of technical fluctuations of the magnetic field. We demonstrated the power of our technique by making for the first time measurements on three extremely narrow Feshbach resonances in ^{87}Rb exhibiting a width as low as 1.3 mG at a magnetic field of 912 G [3]. The unparalleled resolution approaching 10^{-6} provides new insight into the details of the interaction potential between two ^{87}Rb atoms.

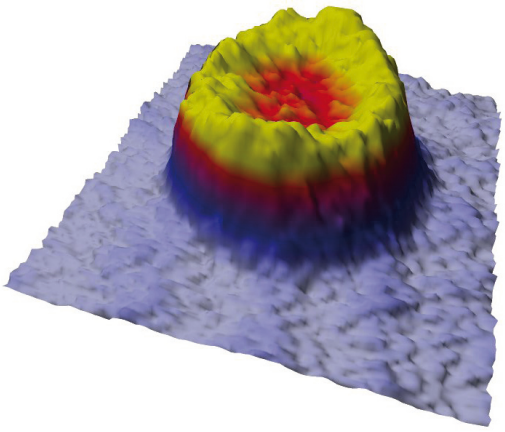

Figure 1: Creation of a mono-energetic atomic wave by dissociation of Feshbach molecules. After dissociation, the atoms fly apart on the surface of a hollow sphere. The absorption-imaging beam integrates the three-dimensional density profile along one direction. The observed two-dimensional image therefore shows a ring, with a nonzero density in the centre [3]. The figure shows a three-dimensional representation of this two-dimensional image.

The dissociation of molecules can also be used to create a mono-energetic outgoing atomic wave, as shown in Fig. 1.

Collisions in ultracold atomic gases have a pure s-wave character. However, the molecular state involved in the Feshbach resonance can be a rotating state. When using such a Feshbach resonance in the molecular association and dissociation process, one can create an outward going rotating wave of atoms. We performed such an experiment with a molecular d-wave state, where dissociation into both an atomic s-wave and an atomic d-wave can occur. Remarkably, the two outgoing partial waves form a spatial interference pattern, demonstrating a fixed phase relationship between the two decay channels. Interestingly, the outgoing d-wave exhibits a shape resonance due to the presence of a (quasi-)bound state inside the centrifugal barrier of the atom-atom interaction potential. This shape resonance enhances the decay of the molecules into atomic d-waves and, moreover, leads to a complex behaviour of the branching ratio and the relative phase of the dissociated partial waves as a function of the magnetic field. We have investigated this behaviour in great detail both theoretically and experimentally, see Fig. 2. The key to a theoretical model lies in the observation that the association and dissociation of molecules can be regarded as the first half and the second half of one collision. This makes it possible to use results from scattering theory to model the dissociation process. Our technique can be used as a high-resolution spectroscopic tool for the investigation of shape resonances [4, 5].

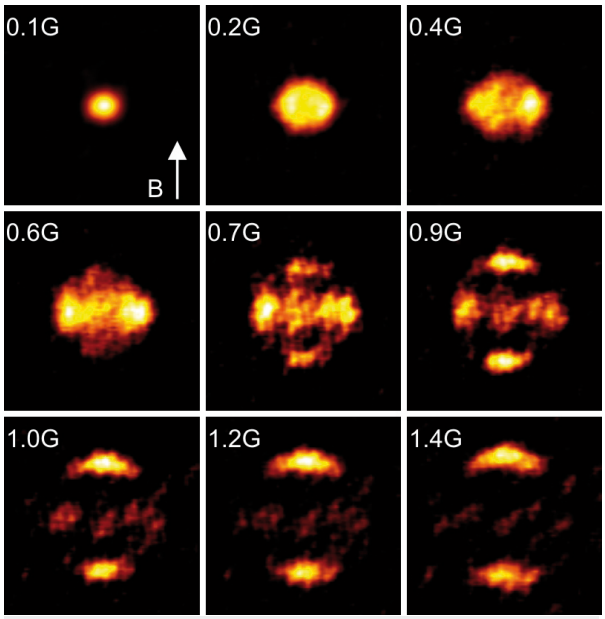

Figure 2: Interference between atomic s- and d-waves. A Feshbach resonance is used to create ultracold molecules in a d-wave bound state. These molecules are dissociated into a coherent superposition of an atomic s-wave and an atomic d-wave. This superposition creates interference patterns which are shown in the figure. The relative phase between the partial waves depends on how far the magnetic field is held above the Feshbach resonance (values in the top left corner). At low magnetic field a flattened disk is visible, whereas at high magnetic field the disk essentially vanishes due to destructive interference. In this regime two lobes at the top and bottom appear [4].

Mott State of Molecules

Standard laser-cooling techniques are not applicable to molecules. Cooling molecular gases from room temperature to quantum degeneracy is therefore a difficult problem, which has not been solved yet. This problem can be circumvented by associating the molecules from pre-cooled atomic gases. This makes the creation of molecular quantum gases feasible with existing technology.

We have created for the first time a Mott state of molecules, which is a quantum degenerate state of a gas in an optical lattice [6]. The experiment started from an atomic Mott insulator, with a core region with exactly two atoms per lattice site surrounded by a shell where the lattice sites are occupied by one atom each. A magnetic-field ramp across the Feshbach resonance associates atom pairs to molecules. Sites containing one atom are unaffected by the ramp. This creates a Mott state of molecules, where each lattice site is occupied by exactly one molecule. If needed, the sites containing one atom

(outside the sphere of molecules) can be emptied by means of radiation pressure from a laser which is resonant to an atomic transition and thus does not affect the molecules.

Three-Body Recombination

Improved understanding of three-body physics will be important for future studies geared towards the creation of trimers. We performed measurements of three-body loss near the Feshbach resonance at 1007.4 G in ^{87}Rb. The measured loss coefficient changes by four (!) orders of magnitude in the vicinity of the Feshbach resonance. We compared our measurements with a numerical model developed by T. Köhler and coworkers at the University of Oxford. Their model is a numerically exact solution of the three-atom problem and does not contain any free fit parameters. The model agrees very well with our data. The model also predicts atom-molecule collision properties and the energies of trimer states [7], and hence will be a valuable resource in future research.

Inelastic Collisions

Inelastic collisions limit the lifetime of trapped ultracold gases. In the case of Feshbach molecules made from bosonic atoms, the corresponding collision rates are large compared to other systems and the resulting lifetimes at typical in-trap densities are a mere few milliseconds. We measured the loss-rate coefficients for inelastic atom-molecule and molecule-molecule collisions. These numbers represent valuable input for models of three-atom and four-atom systems.

1.2.1.2 CAVITY QUANTUM ELECTRODYNAMICS

Light-matter interactions are ubiquitous in nature. Having a light field and an atom that are coupled strongly and that can be studied down to the single quantum level, however, is rare. The cavity quantum electrodynamics project investigates exactly such a system in its laboratory: a single rubidium atom strongly coupled to a high-finesse optical cavity. The aim is to do fundamental quantum optics, both in theory and in experiments. In the past, we have successfully trapped a single rubidium atom in a near-resonant and a far-red-detuned intracavity light field. With such good control over the atom-cavity system, we have now been able to investigate the atom-cavity system by means of spectroscopy. The measured spectra carry information on the residual motion of the atom inside the cavity. By comparing experiment and theory, we have been able to shed new light on the forces influencing this motion, in particular their random character as induced by fluctuations of the light force. Further theoretical studies also lead us to new predictions regarding the use of optical cavities for the purpose of laser cooling and trapping of atoms.

Atom-Cavity Spectroscopy

A single atom that is coupled to a high-finesse optical cavity will have an absorption spectrum different from that of an atom in free space. Vice versa, the transmission spectrum of the cavity is also different from that of an empty cavity. For strong coupling between the atom and the cavity, both spectra display two clearly separated resonances instead of the usual single absorption or transmission resonance. These two resonances can no longer be identified with either the cavity or the atom. Theory for an atom at rest predicts such a normal-mode splitting and the characteristic width of the two lines. However, in a real experiment the atom is not motionless. The atom moves and leaves a fingerprint of this motion in the spectrum. Large spatial excursions comparable to the optical wavelength, in particular, lead to a line broadening comparable to the splitting. But with the cavity cooling and trapping methods recently developed in our laboratory [8], we are now able to localize a single atom inside the cavity so well that a normal-mode spectrum with two well-resolved peaks can be observed [9]. The experiment is a tour-de-force, as spectrum-taking time slots had to be interwoven with cooling time slots in a carefully orchestrated manner.

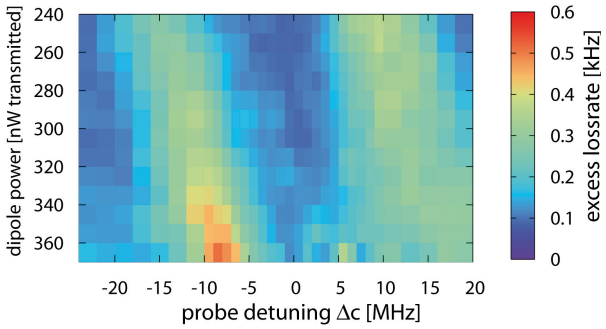

Figure 3: Observed excess loss rate from an intracavity dipole trap as a function of the power of the trap (which shifts the atomic resonance via the Stark shift) and of the detuning of the probe light with respect to the empty cavity resonance. Two separated peaks characterizing the normal modes are clearly visible. The enhanced loss rate on the normal modes can only be understood by taking into account the additional heating caused by the presence of the cavity [9,10].

When examined in detail, the spectra provide a wealth of information about the motional dynamics of the atom in the cavity. It is heated and cooled by different light forces while being trapped in a far-red-detuned dipole trap. Typically, all these forces are enhanced in

the immediate vicinity of the normal-mode resonances. This leads to a strong dependence of the trapping time on the frequencies of the laser, cavity and atom. Results displayed in Fig. 3 show a clearly resolved normal-mode spectrum.

Light-Force Fluctuations in a Cavity

The theory of heating of atomic motion in the presence of light in free space has a long history. Typically, heating is expressed in terms of fluctuations of the light forces. In some geometries like that with a running-wave laser beam, physical interpretations exist where this heating can be understood as the result of random momentum kicks caused by absorbed and emitted photons. In the node of a standing wave, however, the atom will not be excited so that this intuitive picture breaks down. In a cavity the situation is more complex and has features which are even harder the grasp: we have shown, for instance, that an atom at rest at a node of the cavity and excited by a laser transverse to the cavity axis, is rapidly heated in a direction along the cavity axis although it cannot scatter photons into this direction [10]. Another remarkable consequence is that the heating at the normal-mode peaks is dramatically larger than predicted by a free-space theory, as is confirmed by the presence of the normal-mode peaks displayed in Fig. 3. We have shown that the equations describing this strongly coupled atom-cavity system can be decoupled, allowing us to map the heating in a cavity to that in free space. This non-trivial correspondence also allows us to unify the descriptions of the field and the atom. From this a deeper insight is obtained, namely that the enhanced heating coefficient in a cavity can be interpreted as being due to the vacuum fluctuations of the cavity field.

Optical Cavities for Capturing and Cooling Atoms

While cavities offer a platform for fundamental studies, they can also be used as tools. We have shown theoretically that an optical cavity could be appropriate for capturing and cooling hot atoms [11]. The idea is to use cavities with mirrors having a not-too-high reflectivity, such that the light confined in the cavity is efficiently dissipated. The cooling force depends on this dissipation channel, and would then act over a larger range of velocities. If now the atom is at the same time strongly coupled to the cavity, this force will be very large as compared to the standard Doppler force. While the velocity capture range is increased (it is given by the cavity linewidth), the final temperature can nevertheless be maintained close to the standard Doppler limit (which is given by the atomic linewidth). This property is specific to optical cavities: indeed, conventional laser cooling techniques allow the reaching of low temperatures but at the price of a low velocity capture range. Lastly, the developed theory is the first one where the force is analytically derived for all orders of the velocity and coupling between atom and cavity.

Outlook

It would be desirable to confine the atom even better, in order to approach the ideal coupled oscillator system even further. One idea to achieve this is to trap the atom not in a red-detuned field but in a blue-detuned light field. As blue-detuned light fields are repulsive, several higher-order cavity modes [12] are necessary to enclose the atom. This would have the advantage that the atom sits in the darkest spot of the trap, avoiding Stark shifts and enhancing cooling near the centre of the trap.

The experiments so far are done with a high-finesse cavity that was one of the first in its kind. For the future we plan to construct a new generation of cavities that allows more optical access from the side and better length-control capabilities without compromising on finesse or coupling strength.

1.2.1.3 QUANTUM INFORMATION PROCESSING

One major issue in quantum computing is to increase the scale of current experimental implementations so that many quantum bits (qubits) can be handled at once. One way to get there is to establish a network of stationary quantum systems and to interconnect them by flying qubits.

We are investigating the feasibility of linking single atoms and single photons with each other. Our activities focus on an adiabatic coupling between atoms and photons in high-finesse optical cavities [13, 14, 15], the use of such coupled atom-cavity systems as single-photon sources [16, 17, 18], the study of multi-photon interference phenomena [19, 20], and the quantum control and manipulation of individual atoms [21, 22].

Atom-Photon Coupling in Optical Cavities

We have thoroughly investigated the photon statistics of the light emerging from a high-finesse cavity that is coupled to one or many atoms exposed to classical laser light, as shown in Fig. 4.

When a single atom is exposed to a sequence of laser pulses, the cavity emits a stream of single photons in a controlled manner. Such an atom-cavity system is now routinely being operated as a deterministic source of narrowband single-photon pulses [16, 17]. The photons

are emitted on demand into a well-defined mode of the radiation field. They are generated by an adiabatically driven Raman transition, with the vacuum field of the cavity stimulating one branch of the transition, and laser pulses driving the other. The photon statistics shows antibunching, and the photons have excellent coherence properties. These qualify them for applications in quantum information processing.

The interaction of many atoms via a cavity mode is the essential prerequisite for intracavity quantum gates. To investigate such coupling schemes, we have analysed the photon statistics of the light emitted from an atomic

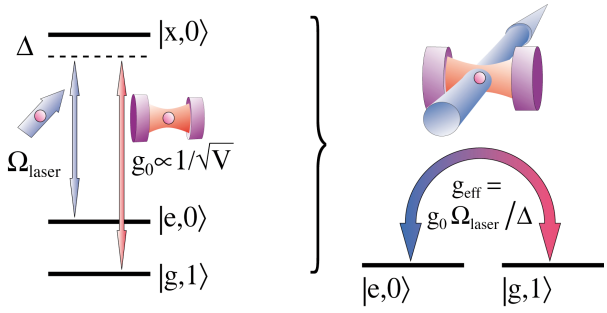

Figure 4: Atom-photon coupling in high-finesse cavities. Laser and cavity drive a Raman transition of the atom. This goes hand-in-hand with a change of the intra-cavity photon number. Modulation of the laser's amplitude and phase allows one to control this process.

ensemble into the cavity as a function of the number of atoms [18]. The light is produced in a Raman transition driven by a pump laser and the cavity vacuum, and a recycling laser is employed to repeat this process continuously. A smooth transition from antibunching to bunching is found for about one intracavity atom. Remarkably, as shown in Fig. 5, the bunching peak develops within the antibunching dip. This well-resolved transition between the quantum and the classical regime is an important step towards many-atom cavity systems under full control. In particular, the pronounced impact of the atom number on the photon statistics impressively shows that the atoms couple to the same mode. The extension of this work to a controlled many-atom cavity system would therefore allow one to perform quantum gate operations in the cavity.

Multi-Photon Quantum Interference

Worldwide, major steps have been taken towards the measurement-induced entanglement [23] and teleportation [24] of atomic states, and towards linear optical quantum computing [25]. In fact, all these ideas rely

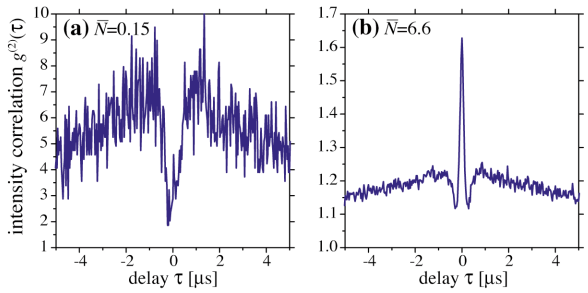

Figure 5: Photon statistics of the light emerging from a continuously driven atom-cavity system. The intensity correlation is shown as a function of the photon-detection time delay in a Hanbury-Brown and Twiss experiment. For a mean atom number below one, antibunching is observed (a), while photon bunching occurs with many atoms in the cavity (b) [18].

on multi-photon interference phenomena that occur if independently generated and indistinguishable photons impinge on separate entrance ports of a beam splitter. Yamamoto has successfully demonstrated two-photon interference [26] and a Bell measurement [27] on photons emerging from a single quantum dot. We have now performed a first experiment in which the interference of two independent photons was investigated in a time-resolved manner [19, 20]. With this tool at hand, we can now characterise the phase evolution and also the mutual dephasing of independent photons as a function of time.

To actually carry out such measurements with only one atom-cavity system available as single-photon emitter, we used pairs of successive photons and an optical delay of the first photon in each pair. In this way we realized that two photons impinge simultaneously on the entrance ports of a beam splitter. With properly shaped and tuned single-photon wave packets, we have observed two-photon interference effects of the Hong-Ou-Mandel type, shown in Fig. 6. As expected, we found that indistinguishable photons coalesce and leave the beam splitter as a pair in one or the other output port. However, most surprisingly, simultaneous photon detections in both output ports do not occur even if the incoming photons are distinguishable, e.g. in the sense that the difference of their centre frequencies exceeds the bandwidths of the single-photon pulses. In this case, we observe a pronounced oscillation of the probability to detect photons in both output ports of the beam splitter as a function of the detection-time difference. The signal oscillates at the difference frequency of the two interfering photons, and has a visibility close to unity, which exceeds the classical limit by a factor of two. The time-dependent amplitude of the beat is a measure for the mutual coherence of the photons;

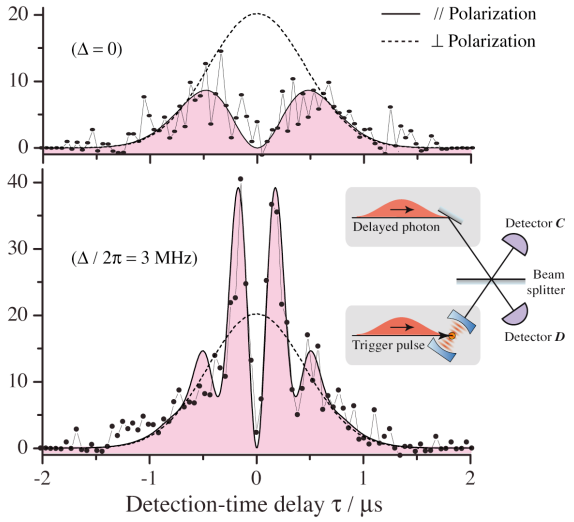

Figure 6: Time-resolved two-photon interference. Two photons impinge simultaneously on a beam splitter. Shown is the number of coincidences in which the photons are found in different output ports (Detectors C and D) as a function of the time delay between photo detections. In the upper panel, the photons have identical centre frequencies. The finite dip width can be attributed to the mutual decoherence of the photons. In the lower panel, the photons have different frequencies. This gives rise to a pronounced beat signal [20].

hence we can use it to trace the loss of coherence in a photonic system as a function of time.

Last but not least, we emphasise that simultaneous photo detections in two different output ports are never observed, i.e. the photons can be found in different ports of the beam splitter only if there is a time lag between the photo detections. Hence, one can apply a temporal filter suitably adapted to the mutual decoherence time of the photons to ensure perfect (post-selected) two-photon coalescence in a non-perfect world.

Manipulation and Control of Single Atoms

Full control of light-matter interactions at the single-atom and single-photon level can be achieved in cavity quantum electrodynamics, in particular in the regime of strong coupling where atom and cavity form a single entity [13, 14, 15, 16, 17]. In the optical domain, this requires a single atom at rest inside a microcavity. Optical dipole traps allow for a deep confinement of atoms but provide no significant cooling. We have shown both experimentally [21] and theoretically [28] that the addition of a probe laser and an optical cavity leads to a strong cooling force acting along the steep gradients of the dipole trap. The reason for this cooling mechanism is that the optical cavity has a resonance frequency which is close to that of the probe laser. Thus, even if the atom is effectively far detuned from the probe laser, it will nevertheless efficiently transfer the radiation from this laser into the cavity. The cavity then dissipates the radiation via its mirrors, which gives a force that depends essentially on the cavity characteristics and, hence, can be made independent of the trap depth. Combined with light forces acting along the probe laser and cavity axis, one obtains 3-dimensional cooling.

The arrangement is illustrated in Fig. 7. Rubidium atoms are transferred from a magneto-optical trap over a distance of 14 mm into the mode volume of a cavity by means of a dipole-force trap, formed by a single horizontal beam of an Yb:YAG laser. The motion is stopped as soon as the atoms arrive in the cavity by changing the trapping potential into a standing-wave trap.

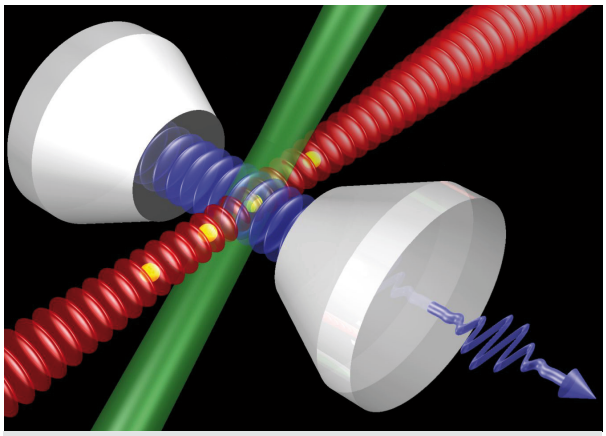

Figure 7: Atoms excited by counter-propagating pump beams (green) scatter photons into a surrounding cavity mode (blue). This goes hand-in-hand with light-induced forces that cool the atoms into the potential wells of a deep standing-wave dipole trap (red).

A pair of counter-propagating laser beams transverse to the cavity axis continuously excites the atom(s). With the spontaneous emission into the cavity being Purcell-enhanced, the rate of fluorescence photons that are emitted first into and then from the cavity mode is a measure of the atom-cavity coupling. With an appropriate detuning of the pump laser frequency from the cavity resonance the atomic motion is cooled whenever photons are scattered. The photon rate can be used to discriminate the exact number of atoms in the cavity. The signal shows individual steps that occur whenever an atom enters or leaves the cavity. The high efficiency of the cooling scheme is also evident from the mean lifetime of the atoms. A dipole-trapped atom remains trapped for 2.7 s without the pump. Only if the pump

laser continuously illuminates an atom, does the average lifetime increases to about 17 s. In addition to these long trapping times, we also reach very low temperatures close to the ground state of the trapping potential. This is unprecedented for a strongly coupled atom, and can be considered as a major step towards a quantum network, with optical links connecting atoms trapped in microcavities [23, 24, 25].

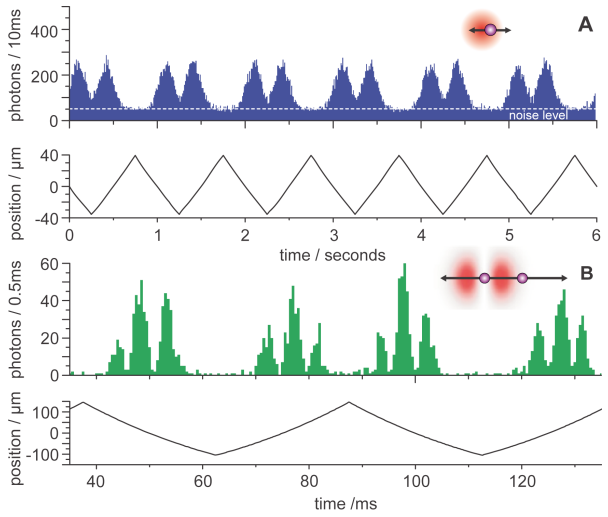

Figure 8: Position control of single atoms in optical cavities using a standing-wave dipole trap as a conveyor belt. (A) shows the Purcell-enhanced emission of a single atom into the cavity while we move it to and fro across the TEM_{00} mode of the cavity. (B) shows a similar situation with two atoms interacting with the TEM_{01} mode. Either atom or both atoms can be coupled to the cavity mode [22].

To subsequently control and adjust the coupling of the trapped atoms to the cavity, we use the standing-wave dipole-force trap as a conveyor belt that is set into motion perpendicular to the cavity axis. This allows us to repetitively move atoms out of and back into the cavity mode. Therefore we are able to either selectively address one atom of a string of atoms by the cavity, or to simultaneously couple two precisely separated atoms to a higher mode of the cavity [22]. This is shown in Fig. 8. The position of the atom(s) relative to the cavity is adjusted by tilting a glass plate in the path of the standing wave. This changes the positions of the antinodes. The atoms follow this motion, which allows a precise tuning of the coupling to the cavity.

Outlook

We have shown that the coherence properties of photons emerging from a coupled atom-cavity system are excellent. This is a key requirement for optical quantum information processing [25], and it is also a sine-quanon for quantum networking between different cavities, where conditional measurements on the photons will be a way to entangle or teleport atomic states [23, 24]. Furthermore, the degree of control we have achieved over the atom-cavity coupling is a large step towards a quantum register consisting of neutral atomic qubits, where each individual atom can be addressed by the cavity, and where pairs of individually addressable atoms can be coupled to one-and-the-same cavity mode, in order to perform cavity-mediated quantum gate operations [29].

1.2.1.4 COLD MOLECULES

The production and investigation of cold and hence slowly moving molecules is a young and fascinating field of research. Due to their slow motion, cold molecules are expected to offer new insights in the course of chemical reactions. Furthermore, cold polar molecules are good candidates for the implementation of quantum-information processing schemes [30]. Up to now, there is no standard recipe to effectively cool freely moving molecules and therefore there is room for unconventional methods. We have developed a novel method which allows filtering of slow polar molecules from a gas in thermal equilibrium by using electric fields [31, 32, 33]. In the filtering process, the interaction of the asymmetric charge distribution of polar molecules with the electric field of a guiding device is exploited, which allows the transport of the slow molecules over large distances. With this technique, molecular fluxes of the order of 10^{10} molecules per second with an average velocity of a few 10 m/s can be achieved for ammonia. We have also demonstrated the filtering and guiding technique for the important class of molecules exhibiting a quadratic Stark effect, as described now.

Cold Water

The electrostatic guide exploits the force that an inhomogeneous electric field exerts on polar molecules. The force is a direct consequence of the energy shift that a molecule experiences in an electric field, in other words, the Stark effect. Initial results were obtained with formaldehyde gas (H_2CO) [31] and ammonia (ND_3) [32], which exhibit a large Stark shift linear in the applied electric field. Other polar molecules are more difficult to guide because their Stark shift is not linear but quadratic in the applied field, and hence, smaller. Some of these molecules are interesting for their own particular reasons. In addition we expect that in general molecules with quadratic Stark shifts will have collision properties that are more favourable for evaporative cooling. Water is an important example of this class of molecules and of great interest for the life sciences and astrophysics.

After improving the apparatus we have been able to guide deuterated water (D_2O) [34]. The guided water has a motional temperature that is of the order of one Kelvin. Interestingly, our analysis shows that due to the filtering the guided water beam is purified and consists of only a handful of rovibrational states.

Continuously Loaded Electrostatic Trap

A basic feature of most methods to produce a trapped sample of cold molecules is their pulsed operation, where the trap is, e.g., switched on after the sample has been produced. From that point onward, the sample decays, e.g., by collisions with background gas, and has to be regenerated. A continuously operated trap would be advantageous not only for high-precision measurements, where long observation times with samples under constant conditions are required, but also for determining cold collision rates of reacting molecular species. Our electrostatic filtering method produces a continuous beam of guided molecules. We have built an electrostatic trap [35] that can be loaded continuously from such a guide, as depicted in Fig. 9.

The trap consists of a series of ring-shaped electrodes of alternating polarity, so that high electric fields near the electrodes confine our (low-field-seeking) molecules at the nearly field-free region in the centre of the trap, as visible in Fig. 10. The geometry allows a leakage-free connection to the guides with quadrupole symmetry to fill the trap or extract molecules from it. Because of the randomization of the motion in the trap, a molecule has in principle an equal chance to reach either one of the holes. Therefore, a dynamic equilibrium is established as soon as the loading rate equals the rate at which the molecules leak out of the trap. With this trap, we have succeeded in storing a molecular gas of approximately 10^8 molecules in a volume of $\sim$0.6 cm^3 at a temperature of 300 mK for about 130 ms.

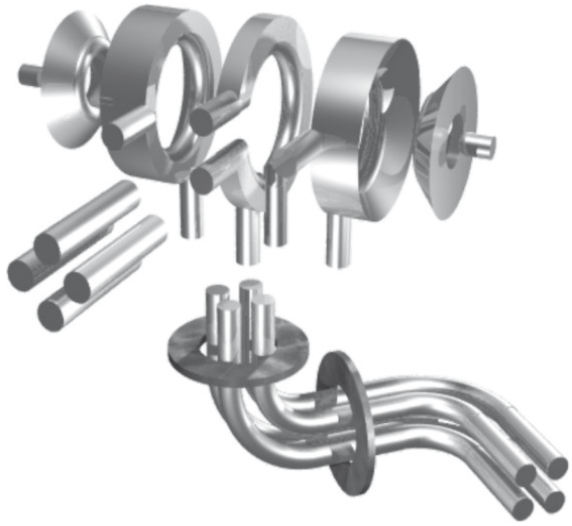

Figure 9: Exploded view of the electric trap. In the lower half the four-electrode guide is seen with its two 90° bends. The guide loads slow molecules into the electric trap, which consists of 7 electrodes with high voltages of alternating polarity. Molecules trapped in the trap randomize their motion because of the irregular shape of the trapping potential. They leave the trap either back through the input or through the output guide where they will be led to a detector.

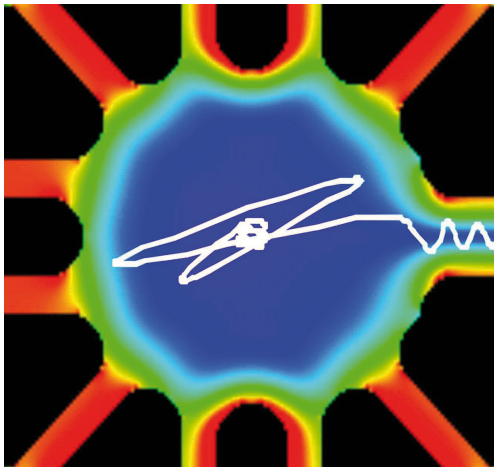

Figure 10: Electric field in a plane through the axis and the entrance of the trap. The colour code from weak to strong electric fields is blue, green, and red, respectively. The electrodes are black. A simulated trajectory of a molecule can be seen in white, entering the trap from the right and leaving the trap via the output perpendicular to the projection plane.

Outlook

We will now start to explore methods to investigate and reduce the internal dynamics of the molecules. One project in this line is the construction of a new, cryogenic, source. This source will combine buffer-gas cooling with electrostatic filtering and guiding. It is expected to produce a dense guided beam of slow state-selected molecules. Simultaneously we are setting up UV optics in order to prepare for in-situ diagnostics of the trapped molecules. This should also give insight into a new and potentially powerful optical cooling method for molecules: cavity cooling. This method has only recently been demonstrated for single atoms [8, 21], and is seen as the only optical method that should be applicable to molecules, as it relies on coherent scattering. For future studies of interactions between ultracold molecules, dissipative methods like the two that were mentioned above will become indispensable.

1.2.1.5 JUNIOR RESEARCH GROUP

Quantum Simulations with Trapped Ions
Leader: Dr. Tobias Schätz

To gain deeper insight into the "macroscopic" quantum behaviour of nature, such as high-temperature superconductivity, one has to understand or simulate large quantum systems. However, the simulation of the dynamics of only some ten of interacting quantum objects is already intractable for the most-powerful classical computers. For instance, the generic state of only 30 electrons (two-level systems or quantum bits) in a magnetic field is defined by 2^{30} numbers. A description of its evolution requires a matrix of $2^{30}\times 2^{30}$. Increasing classical calculation capabilities cannot and will not help to simulate even slightly larger quantum systems: for 300 particles, 2^{300} numbers describe their state, close to the estimated amount of protons in our universe.

Quantum Computer/Simulator

As originally proposed by Feynman [36], a universal quantum computer could efficiently simulate the dynamics of many-body quantum systems, incorporating the quantum behaviour of nature by sharing quantum bits (qubits) instead of classical bits (0 or 1). Following the original proposal by Feynman, we want to choose a system with an evolution that is governed by the same equations as the system to be simulated. This analogue quantum simulator approach was adapted to traps hosting ions as qubits (represented by two electronic levels) by Porras and Cirac in 2004 [37]. Instead of translating quantum dynamics into an algorithm of stroboscopic quantum gate operations running on a universal quantum computer, we will control and manipulate our qubit ions in a continuous way that is equivalent to the way nature evolves the system of our interest.

Experimental Challenge

The systems (Hamiltonians) that can be realized with trapped ions can be quantum spin systems, describing magnetism in many solid-state systems like magnets, high-T_c superconductors, quantum Hall ferromagnets, ferroelectrics, etc. To illustrate the experimental procedure, let us consider the simulation of the quantum Ising model. The interaction of the spins (qubit ions) with the environment (the magnetic field) and between the spins will be simulated via their interaction with laser beams and the repulsion between our qubit ions trapped along a linear chain, as shown in Fig. 11.

While two-photon stimulated-Raman transitions will provide Rabi flopping between our two qubit levels and therefore simulate the rotation of the individual spins in the external magnetic field, a state-dependent (conditional) optical dipole force will realize an effective interaction between (neighbouring) spins. This conditional force, e.g. applied along the axis of the ion string in ferromagnetic order, in which all spins point in the same direction, would simply displace all the qubit ions along this axis and thus not change the Coulomb energy of the system. But for the ions being in any different order, the force would change the distance between neighbouring qubit ions and therefore increase the Coulomb energy. Thus, starting in any ground state of the system and slowly (adiabatically) turning on the laser force would always keep the system in its ground state and evolve it therefore naturally into the ferromagnetic order [37]. The simulation of this evolution would allow one to observe and analyze quantum phase transitions. In contrast to a classical phase transition (driven by thermal fluctuations) these quantum phase transitions (driven by quantum fluctuations) provide nature with superposition states of the two energetically equivalent ferromagnetic states (where all spins point up and down at the same time). This should allow for the investigation of maximally entangled states.

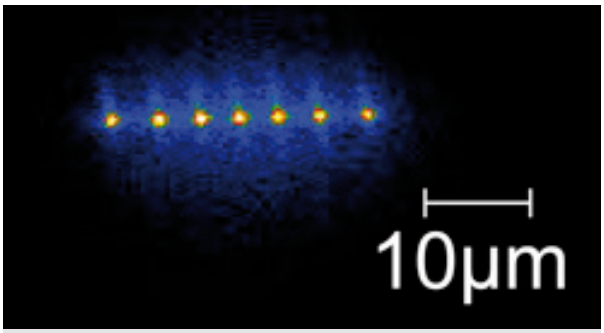

Figure 11: Fluorescence light of a linear chain of seven laser cooled $^{25}Mg^{+}$ ions in the experimental zone of our segmented linear Paul-trap.

The possibility to control all the parameters of the system individually by switching laser beams and/or trap voltages and to address each single spin on each single lattice site turns it into a versatile system offering tools for analysis overcoming by far the access in experiments on solid-state systems. We will start with experiments involving only a few qubits [38]. Scaling the system to 10 qubits might already allow us to outperform classical simulations and could lead to a deeper insight into the dynamics of quantum systems. Implementing individual addressing would allow for an initial state preparation representing a particular spin excitation. We could also analyze non-equilibrium dynamics by switching the interactions fast enough (non-adiabatically) [37]. To allow for simulations of many more than 10 spins we will have to further investigate the scaling possibilities of our trap apparatus.

Technical Progress

The necessity of high laser power, high spectral demands and financial reasons led us to develop an all-solid-state laser system fulfilling our needs. By frequency doubling commercial fibre laser systems twice in external ring resonators [39], we were able to set up three lasers systems in 2005, necessary to realize the quantum simulator proposal. We developed and realized a six-times segmented linear Paul trap providing a loading and an experimental zone of the anticipated tight confinement (up to $2\pi\times8$ MHz radial trapping frequency). We photo-ionized Magnesium at the end of 2005, first trapped, laser cooled and detected it in January 2006 as shown in Fig. 11, calibrated the trapping parameters and successfully transferred the ions between the zones. We achieve life times of the ions in our trap of the order of days. Finishing the setup of our laser beams for coherent two-photon stimulated Raman transitions and the individually developed experimental control, we should be able to run our first simulation experiments in 2006.

Outlook

Our experimental setup for the realisation of basic quantum simulations provides us with the necessary tools to approach a set of additional simulation problems we will try to access, such as strong correlation between Bosons [40], quantum-random walk [41, 42] or particle production in our early universe [43, 44]. In close collaboration with the group of Prof. Rempe, we plan to investigate in a separate experimental setup whether laser-cooled atomic ions and cold neutral molecules can be brought to mutually interact. In collaboration with the Prof. Krausz and co-workers, we are planning to use a similar apparatus for loading, trapping and sympathetic laser cooling of (internally cold) orientated molecular ions to study fast dynamical changes triggered by femtosecond laser pulses via electron/X-ray scattering.

The work described is supported by the Emmy-Noether program of the DFG, by the MPG, by the Theory division of Prof. Cirac and by the division of Prof. Rempe, the latter contributing a part of the required resources.

REFERENCES

[1] S. Dürr et al., Phys. Rev. Lett. **92**, 020406 (2004)
[2] T. Mukaiyama et al., Phys. Rev. Lett. **92**, 180402 (2004)
[3] S. Dürr et al., Phys. Rev. A **70**, 031601(R) (2004)
[4] T. Volz et al., Phys. Rev. A **72**, 010704(R) (2005)
[5] S. Dürr et al., Phys. Rev. A **72**, 052707 (2005)
[6] T. Volz et al., arXiv:cond-mat/0605184
[7] G. Smirne et al., arXiv:cond-mat/0604183
[8] P. Maunz et al., Nature **428**, 50 (2004)
[9] P. Maunz et al., Phys. Rev. Lett. **94**, 033002 (2005)
[10] K. Murr et al., arXiv:quant-ph/0512001
[11] K. Murr, Phys. Rev. Lett. **96**, 253001 (2006)
[12] T. Puppe et al., Physica Scripta **T112**, 7(2004)
[13] M. Hennrich et al., Phys. Rev. Lett. **85**, 4872 (2000)
[14] A. Kuhn et al., in Quantum Information Processing, T. Beth and G. Leuchs (Eds.), 182, Wiley-VCH (Berlin 2003)
[15] A. Kuhn and G. Rempe in Experimental Quantum Computation and Information, M.F. De and C. Monroe (Eds.), Vol. **148**, 37, IOS-Press (Amsterdam 2002)
[16] A. Kuhn et al., Appl. Phys. B **69**, 373 (1999)
[17] A. Kuhn et al., Phys. Rev. Lett. **89**, 067901 (2002)
[18] M. Hennrich et al., Phys. Rev. Lett. **94**, 053604 (2005)
[19] T. Legero et al., Appl. Phys. B **77**, 797 (2003)
[20] T. Legero et al., Phys. Rev. Lett. **93**, 070503 (2004)
[21] S. Nußmann et al., Nat. Phys. **1**, 122 (2005)
[22] S. Nußmann et al., Phys. Rev. Lett. **95**, 173602 (2005)
[23] C. Cabrillo et al., Phys. Rev. A **59**, 1025 (1999)
[24] S. Bose et al., Phys. Rev. Lett. **83**, 5158 (1999)
[25] E. Knill et al., Nature 409, **46** (2001)
[26] D. Fattal et al., Phys. Rev. Lett. **92**, 037903 (2004)
[27] C. Santori et al., Nature **419**, 594 (2002)
[28] K. Murr et al., Phys. Rev. A **73**, 063415 (2006)
[29] T. Pellizzari et al., Phys. Rev. Lett. **75**, 3788 (1995)
[30] D. DeMille, Phys. Rev. Lett. **88**, 067901 (2002); A. Micheli et al., Nat. Phys. **2**, 287 (2006)
[31] S.A. Rangwala et al., Phys. Rev. A **67**, 043406 (2003)
[32] T. Junglen et al., Eur. Phys. J. D **31**, 365 (2004)
[33] T. Junglen et al., Phys. Rev. Lett. **92**, 223001 (2004)
[34] T. Rieger et al., Phys. Rev. A. **73**, 061402(R) (2006)
[35] T. Rieger et al., Phys. Rev. Lett. **95**, 173002 (2005)
[36] R.P. Feynman, Int. J. Theor. Phys., **21** (1982)
[37] D. Porras et al., Phys. Rev. Lett. **92**, 207901 (2004)
[38] T. Schaetz et al., Appl. Phys. B, **79**, 979 (2004)
[39] A. Friedenauer et al., online published in Appl. Phys. B, (2006)
[40] D. Porras and J.I. Cirac, Phys. Rev. Lett. **93**, 263602 (2004)
[41] B.C. Travaglione and G. J. Milburn, Phys. Rev. A **65**, 032310 (2002)
[42] Y. Omar, private communication (2005)
[43] P.M. Alsing et al., Phys. Rev. Lett. **94**, 220401 (2005)
[44] R. Schützhold and T. Schaetz, to be submitted

1.2.2 SURVEY OF THE RESEARCH ACTIVITIES

Bose-Einstein Condensation

Project	Objective	Staff
Dissociation of Feshbach molecules	Determination of the width of Feshbach resonances from measurements of the molecule dissociation. Creation of an outgoing d-wave in the dissociation of molecules and investigation of shape resonances.	S. Dürr N. Syassen T. Volz
Mott state of molecules	Creation of a Mott state of molecules in an optical lattice.	D.M. Bauer S. Dürr E. Hansis N. Syassen T. Volz
Three-body recombination	Characterization of the three-atom system by measurement of three-body recombination.	S. Dürr N. Syassen T. Volz
Inelastic collisions	Study of inelastic atom-molecule and molecule-molecule collisions.	S. Dürr N. Syassen S. Teichmann T. Volz

Cavity Quantum Electrodynamics

Project	Objective	Staff
Light forces in optical cavities	Understanding momentum diffusion in a optical cavity.	P. Maunz K. Murr P.W.H. Pinkse T. Puppe I. Schuster
Laser cooling in optical cavities	Development of a theory of velocity-dependent light forces for arbitrary order in the atom-cavity interaction.	K. Murr
Atom-cavity spectroscopy	Demonstration of viability of quantum-optics experiments with a single atom inside a microscopic high-finesse cavity.	P. Maunz P.W.H. Pinkse T. Puppe I. Schuster
Blue trap	Development of an improved intracavity dipole trap with blue-detuned light fields.	A. Kubanek K. Murr P.W.H. Pinkse T. Puppe I. Schuster
Cavity Mk II	Development of a new cavity with better optical access and special length control.	J. Almer A. Kubanek P.W.H. Pinkse T. Puppe I. Schuster

Quantum Information Processing

Project	Objective	Staff
Atom trapping and cooling	Trapping, cooling and manipulation of single atoms inside high-finesse cavities: theory and experiment.	M. Hijlkema A. Kuhn K. Murr S. Nußmann H. Specht B. Weber S.C. Webster
Atom-photon interfaces	Coupling of atoms and photons in optical cavities and controlled generation of non-classical light.	J. Bochmann M. Hennrich A. Kuhn G. Langfahl T. Legero H. Specht S.C. Webster T. Wilk
Single-photon characterisation	Characterisation of single-photon pulses using many-photon interference phenomena.	A. Kuhn T. Legero S.C. Webster T. Wilk

Cold Molecules

Project	Objective	Staff
Electrostatic trapping	Electrostatic trapping of slow molecules in two and three dimensions.	T. Junglen P.W.H. Pinkse T. Rieger
Cryogenic source	Development of a cryogenic source combining buffer-gas cooling with guided extraction.	L.D. van Buuren P.W.H. Pinkse
Spectroscopy	Spectroscopic study of guided molecules.	M. Motsch M. Zeppenfeld P.W.H. Pinkse
Electrodynamic trapping	Development of new electrodynamic trapping methods for high-field and low-field seeking molecules.	P.W.H. Pinkse T. Rieger P. Windpassinger

JUNIOR RESEARCH GROUP

Quantum Simulations with Trapped Ions

Project	Objective	Staff
Quantum simulations with trapped atomic ions	Demonstration of the feasibility for simulating a "quantum phase transition" in a segmented linear Paul trap using atomic ions as qubits.	A. Friedenauer L. Petersen T. Schätz H. Schmitz
Trapping of neutral molecules and atomic ions	Guiding and trapping of neutral polar molecules and atomic (lasercooled) ions.	S. Kahra G. Leschhorn P.W.H. Pinkse T. Schätz
Single molecule imaging	Loading, trapping and sympathetic laser cooling of (internally cold) orientated molecular ions to study fast dynamical changes triggered by femtosecond laser pulses via electron/X-ray scattering.	S. Kahra G. Leschhorn E. Fill W. Fuß T. Schätz

1.2.3 SELECTED REPRINTS

1) T. Legero, T. Wilk, M. Hennrich, G. Rempe and A. Kuhn:
Quantum beat of two single photons.
Physical Review Letters **93**, *070503 (2004).*
MPQ Progress Report: page 82

2) S. Dürr, T. Volz and G. Rempe:
Dissociation of ultracold molecules with Feshbach resonances.
Physical Review A **70**, *031601(R) (2004).*
MPQ Progress Report: page 86

3) P. Maunz, T. Puppe, I. Schuster, N. Syassen, P.W.H. Pinkse and G. Rempe:
Normal-mode spectroscopy of a single bound atom-cavity system.
Physical Review Letters **94**, *033002 (2005).*
MPQ Progress Report: page 90

4) M. Hennrich, A. Kuhn and G. Rempe:
Transition from antibunching to bunching in cavity QED.
Physical Review Letters **94**, *053604 (2005).*
MPQ Progress Report: page 94

5) T. Volz, S. Dürr, N. Syassen, G. Rempe, E. van Kempen and S. Kokkelmans:
Feshbach spectroscopy of a shape resonance.
Physical Review A **72**, *010704(R) (2005).*
MPQ Progress Report: page 98

6) T. Rieger, T. Junglen, S. Rangwala, P.W.H. Pinkse and G. Rempe:
Continuous loading of an electrostatic trap for polar molecules.
Physical Review Letters **95**, *173002 (2005).*
MPQ Progress Report: page 102

7) S. Nußmann, M. Hijlkema, B. Weber, F. Rohde, G. Rempe and A. Kuhn:
Submicron positioning of single atoms in a microcavity.
Physical Review Letters **95**, *173602 (2005).*
MPQ Progress Report: page 106

8) S. Nußmann, K. Murr, M. Hijlkema, B. Weber, A. Kuhn and G. Rempe:
Vacuum-stimulated cooling of single atoms in three dimensions.
Nature Physics **1**, *122-126 (2005).*
MPQ Progress Report: page 110

9) K. Murr:
Large velocity capture range and low temperatures with cavities.
Physical Review Letters **96**, *253001 (2006).*
MPQ Progress Report: page 115

10) T. Rieger, T. Junglen, S.A. Rangwala, G. Rempe P.W.H. Pinkse and J. Bulthuis:
Water Vapour at a Translational Temperature of 1 K.
Physical Review A, **73**, *061402(R) (2006).*
MPQ Progress Report: page 119

JUNIOR RESEARCH GROUP

1) A. Friedenauer, F. Markert, H. Schmitz, L. Petersen, S. Kahra, M. Herrmann, Th. Udem, T.W. Hänsch and T. Schätz:
High power all solid state laser system near 280 nm.
Appl. Phys. B 84, *371-373 (2006)*
MPQ Progress Report: page 123

2) T. Schaetz, M. D. Barrett, D. Leibfried et al.:
Quantum Dense Coding with Atomic Qubits.
Physical Review Letters **93**, *040505 (2004).*
MPQ Progress Report: page 126

VOLUME 93, NUMBER 7 PHYSICAL REVIEW LETTERS week ending 13 AUGUST 2004

Quantum Beat of Two Single Photons

Thomas Legero, Tatjana Wilk, Markus Hennrich, Gerhard Rempe, and Axel Kuhn
Max-Planck-Institut für Quantenoptik, Hans-Kopfermann-Strasse 1, D-85748 Garching, Germany
(Received 15 March 2004; published 13 August 2004)

The interference of two single photons impinging on a beam splitter is measured in a time-resolved manner. Using long photons of different frequencies emitted from an atom-cavity system, a quantum beat with a visibility close to 100% is observed in the correlation between the photodetections at the output ports of the beam splitter. The time dependence of the beat amplitude reflects the coherence properties of the photons. Most remarkably, simultaneous photodetections are never observed, so that a temporal filter allows one to obtain perfect two-photon coalescence even for nonperfect photons.

DOI: 10.1103/PhysRevLett.93.070503 PACS numbers: 03.67.Hk, 03.67.Mn, 42.50.Dv, 42.65.Dr

The quantum nature of light impressively manifests itself in the fourth-order interference of two identical and mutually coherent single photons that impinge simultaneously on a beam splitter (BS). The photons coalesce and both leave the beam splitter in the same direction. Hong *et al.* first demonstrated this phenomenon with photon pairs from parametric down-conversion [1], and Santori *et al.* used the same effect to show the indistinguishability of independently generated photons that are successively emitted from a quantum dot embedded in a microcavity [2]. In all experiments performed so far, the photons were short compared to the time resolution of the employed detectors, so that interference phenomena were observed only as a function of the spatial delay between the interfering photons [3].

To investigate the temporal dynamics behind this interference phenomenon, we now use an adiabatically driven, strongly coupled atom-cavity system as a single-photon emitter [4–7]. Photons are generated by a unitary process, so that their temporal and spectral properties can be arbitrarily adjusted. In fact, the duration of the photons used in our experiment exceeds the time resolution of the employed single-photon counters by 3 orders of magnitude. This allows for the first time an experimental investigation of fourth-order interference phenomena in a time-resolved manner with photons arriving simultaneously at the beam splitter [8]. We find perfect interference even if the frequency difference between the two photons exceeds their bandwidths. This surprising result is very robust against all kinds of fluctuation and opens up new possibilities in all-optical quantum information processing [9].

The principal scheme of the experiment is sketched in Fig. 1. We consider an initial situation where two single photons in modes A and B impinge simultaneously on a BS. In front of the BS, we distinguish states $|1_{A,B}\rangle$ and $|0_{A,B}\rangle$, where a photon is either present or has been annihilated by transmission through the BS and subsequent detection by detector C or D. Mode A is an extended spatiotemporal photonic field mode, traveling along an optical fiber, which initially carries a photon. The photon in mode B emerges from a strongly coupled atom-cavity system, which is driven in a way that the photon is deterministically generated by a vacuum-stimulated Raman transition between two long-lived atomic states [4,5]. In particular, the photon emitted from B matches the photon from A. The initial state of the total system, A and B, is given by the product state $|\Psi_i\rangle = |1_A 1_B\rangle$. The effect of a first photodetection in the output mode C or D at time t_0 is evaluated by applying the respective photon annihilation operator $\hat{a}_C$ or $\hat{a}_D$ to $|\Psi_i\rangle$. The two operators behind the BS are linked to the two operators before the BS by the unitary relation

$$\hat{a}_{C,D} = (\hat{a}_B \pm \hat{a}_A)/\sqrt{2}, \quad (1)$$

where $\hat{a}_A$ and $\hat{a}_B$ are operators that remove one photon from A and B, respectively. As the detection reveals no which-way information, the system is projected into one of the two superposition states,

$$|\Psi_\pm(t_0)\rangle = \hat{a}_{C,D}|1_A 1_B\rangle = (|1_A, 0_B\rangle \pm |0_A, 1_B\rangle)/\sqrt{2}, \quad (2)$$

depending on which detector clicks.

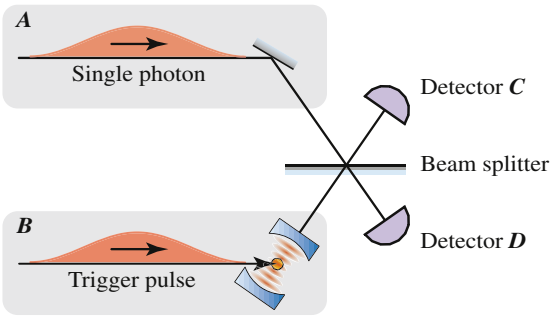

FIG. 1 (color online). Fourth-order interference. Single photons emerge from A and B and impinge simultaneously on a beam splitter. The photons are so long that they give rise to distinct photodetections. The first detection projects the system into a superposition, which then determines the probability of detecting the second photon with either one or the other detector.

VOLUME 93, NUMBER 7 PHYSICAL REVIEW LETTERS week ending 13 AUGUST 2004

The initial purity of the superposition, i.e., the balance between its two parts and their phase coherence, and, hence, also the mutual coherence time of the interfering photons, can now be measured by monitoring the time evolution of $|\Psi_{\pm}\rangle$. Moreover, the superposition can be systematically varied by controlling the relative phase between its two parts. The latter is achieved by introducing a small frequency difference between the photons from A and B. Assume that the photon in the fiber has a frequency difference Δ with respect to the photon from the cavity. In this case, the two components of $|\Psi_{\pm}\rangle$ evolve with different frequencies, so that after a time τ, the two states have acquired a phase difference $\Delta\tau$. The new state then reads

$$|\Psi_{\pm}(t_0+\tau)\rangle = (|1_A, 0_B\rangle \pm e^{i\Delta\tau}|0_A, 1_B\rangle)/\sqrt{2}. \quad (3)$$

This state can be monitored by photodetections. The probability to count a second photon with either detector C or D, as a function of the relative phase $\Delta\tau$, reads

$$\langle\Psi_{\pm}|\hat{a}_C^{\dagger}\hat{a}_C|\Psi_{\pm}\rangle = \tfrac{1}{2}(1 \pm \cos\Delta\tau)$$
$$\text{and} \quad \langle\Psi_{\pm}|\hat{a}_D^{\dagger}\hat{a}_D|\Psi_{\pm}\rangle = \tfrac{1}{2}(1 \mp \cos\Delta\tau). \quad (4)$$

In a photon correlation experiment, a frequency difference between the interfering photons therefore results in a quantum-beat signal in the correlation function that oscillates with frequency Δ. Moreover, Eq. (4) implies that the first and second photon hit the same detector for $\Delta = 0$. This corresponds to the well-known behavior of two indistinguishable photons that impinge simultaneously on a BS [1,2]. However, in the present case, the two photodetections can have a time delay that can be as large as the duration of the interfering photons. Nevertheless, perfect two-photon coalescence is expected. Another remarkable consequence from Eq. (3) is that the initial phase difference between its two parts, induced by the first photodetection, is either 0 or π. Therefore, the beat starts to oscillate at zero with the detection of a first photon, so that the cross-correlation function between the two BS output ports shows fringes with a visibility of 100%. This distinguishes the present situation dramatically from the situation of two interfering coherent fields with frequency difference Δ that are superposed on a BS. In the latter case, the cross-correlation function would oscillate with a fringe visibility not exceeding 50%, since photodetections do not influence the relative phase of the coherent fields. The present scheme is also different from other experiments, where quantum state reduction has been observed in optical cavity QED [10,11]. In these experiments, the detection of a photon changes the state of a single system, whereas in the present case, the relative phase of two distinct modes, A and B, is determined.

We emphasize that the above way of calculating joint photodetection probabilities is strongly simplified. A more detailed analysis that comes to the same conclusions can be found in Ref. [8].

The experimental setup is sketched in Fig. 2(a). ^{85}Rb atoms released from a magneto-optical trap fall with 2 m/s through a cavity of finesse $F = 60,000$ with $(g_{\max}, \kappa, \gamma)/2\pi = (3.1, 1.25, 3.0)$ MHz, where $g_{\max}$ is the optimal atom-cavity coupling constant, and κ and γ are the field decay rates of cavity and atom, respectively. The atoms enter one at a time with a probability that is 66 times higher than the probability of having more atoms. Each atom is prepared in $|e\rangle \equiv |5S_{1/2}, F = 3\rangle$, while the cavity is resonant with the transition between $|g\rangle \equiv |5S_{1/2}, F = 2\rangle$ and $|x\rangle \equiv |5P_{3/2}, F = 3\rangle$. The atom experiences a sequence of laser pulses that alternate between triggering single-photon emissions and repumping the atom to state $|e\rangle$: The 2 μs long trigger pulses are resonant with the $|e\rangle \leftrightarrow |x\rangle$ transition and their Rabi

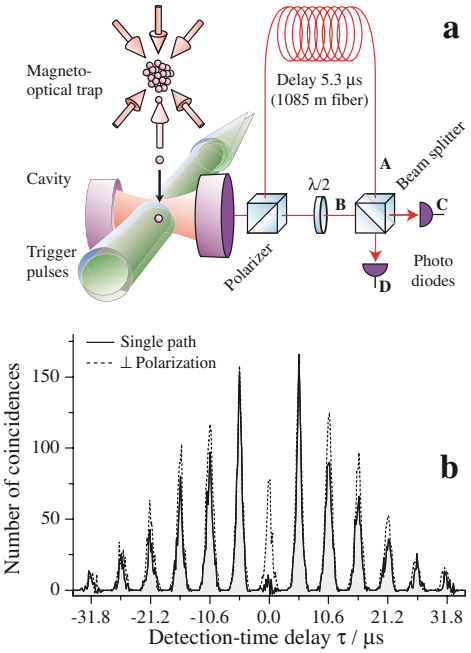

FIG. 2 (color online). Atoms and photons. (a) Triggered by laser pulses, an atom-cavity system emits unpolarized single photons. They are randomly directed by a polarizing beam splitter along two paths towards a nonpolarizing beam splitter (BS). A photon traveling along path A gets delayed so that it impinges on the BS simultaneously with a subsequent photon that travels along path B. (b) Number of coinciding photodetections in the two output ports as a function of the time difference between the detections: If only a single path is open, a Hanbury-Brown–Twiss measurement of the intensity correlation is performed, showing antibunching (solid line). If both paths are open but have perpendicular polarization, no interference takes place and the BS randomly directs the photons to C and D. This leads to coincidences at $\tau \approx 0$ (dashed line). All traces result from a convolution with a 48 ns wide square time-bin function.

VOLUME 93, NUMBER 7 PHYSICAL REVIEW LETTERS week ending 13 AUGUST 2004

frequency increases linearly to $\Omega_{\max}/2\pi = 17.8$ MHz. In connection with the vacuum field of the cavity stimulating the $|x\rangle \leftrightarrow |g\rangle$ transition, these pulses adiabatically drive a stimulated Raman transition to $|g\rangle$. This transition goes hand in hand with a photon emission. Between two emissions, another laser pumps the atom from $|g\rangle$ to $|x\rangle$, from where it decays back to $|e\rangle$. This is complemented by a π-polarized laser driving the transition $|5S_{1/2}, F = 3\rangle \leftrightarrow |5P_{3/2}, F = 2\rangle$ to produce a high degree of spin polarization in $m_F = \pm 3$, with a large coupling to the cavity. To discard the photons emerging during this process, the detectors are electronically gated. This leads to a modulation of the dark-count rate and, hence, to a triangular modulation of the background contribution to all correlation functions measured with detectors C and D, with maxima showing an average number of 3.2 correlations/48 ns. All data shown here have been corrected for this periodic background.

We now consider the case where the atom-cavity system emits two photons, one after the other, with a time separation of 5.3 μs, deliberately introduced by the periodicity of our trigger pulse sequence. We suppose that the first photon travels along an optical fiber (mode A) and hits a 50:50 BS at the fiber output at the same time as the second photon, provided the latter comes directly from the cavity (mode B). To characterize the system, we first close the fiber, so that photons impinge only in mode B. For this situation, Fig. 2(b) shows the intensity correlation function, measured with detectors C and D, as a function of the time difference τ between photodetections as a solid line. The central peak is missing; i.e., the light shows strong antibunching and photons are emitted one by one [4]. Next, both paths to the BS are opened, so that photons can impinge simultaneously on the BS. Interference is suppressed by adjusting the $\lambda/2$ retardation plate at input port B so that the two light fields are polarized perpendicular to each other (dashed line). In this case, each photon is randomly directed onto one of the detectors, C or D. This leads to a nonvanishing correlation signal at $\tau \approx 0$, which is a factor of 2 smaller than the neighboring peaks at $\tau = \pm 5.3$ μs. The central peak has a duration of 640 ns (half width at $1/e$ maximum), which comes from the convolution of two 450 ns long single photons (half width at $1/e$ maximum of the intensity). In the following, the signal obtained for perpendicularly polarized photons is used as a reference, since any interference leads to a significant deviation. Note that all the experimental traces presented here are not sensitive to photon losses, since only measured coincidences contribute. Moreover, they can be compared without normalization, since data was always recorded until 980 coincidences were obtained in the correlation peaks at $\tau = \pm 5.3$ μs. This required loading and releasing atoms from the magneto-optical trap about 10^5 times.

Experimental results obtained for parallel polarization are displayed in Fig. 3(a). The photons interfere and the first photodetection reveals no which-way information. Therefore, the system is projected into the superposition state $|\Psi_{\pm}\rangle$. In contrast to the expectations from the above discussion, the correlation signal does not vanish completely, in particular, for nonzero detection-time delay. Instead, a pronounced minimum is observed around $\tau = 0$. We interpret the depth of this minimum as a measure of the initial purity of the superposition state, and we attribute its limited width to the average mutual dephasing of the interfering photons (see below). Moreover, as shown in Fig. 3(b), we resolve a pronounced oscillation of the correlation function, starting with a minimum at $\tau = 0$, when a frequency difference of $\Delta/2\pi = 3$ MHz is introduced between the interfering photons. The first maxima of the oscillation are found at $|\tau| \approx \pi/\Delta$, where the two parts of $|\Psi_{\pm}\rangle$ have acquired a phase difference of $\pm\pi$. If the photons are detected with this time difference, they are registered by different detectors and give rise to a coincidence count. Therefore, the

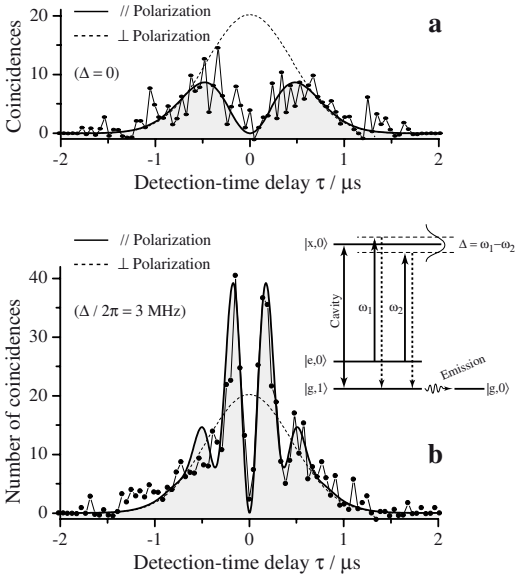

FIG. 3. Quantum beat. Number of coinciding photodetections as a function of the time difference τ between the detections [only the central peak is shown; see Fig. 2(b)]. Both paths are open and have parallel polarization (circles). The solid lines represent a numerical fit to the data [8]. A Gaussian fit to the reference signal (perpendicular polarization, dashed line) is also shown. (a) Photons of identical frequencies lead to a 460 ns wide central minimum. This lack of coincidences is caused by coalescing photons that leave the BS through the same port. Depth and width of the minimum indicate the initial purity of the superposition and the mutual coherence time of the photons, respectively. (b) The atom-cavity system is driven by a sequence of laser pulses with a frequency difference $\Delta = |\omega_1 - \omega_2| = 2\pi \times 3$ MHz between consecutive pulses (see level scheme). This gives rise to a frequency difference between consecutive photon emissions, which leads to a quantum beat in the correlation function starting at $\tau = 0$.

VOLUME 93, NUMBER 7 PHYSICAL REVIEW LETTERS week ending 13 AUGUST 2004

number of coincidences in these maxima exceeds the reference level, measured with perpendicular polarization, by a factor of 2. This underpins the phase coherence of the whole process and shows that it is possible to arbitrarily adjust the relative phase between the two parts of $|\Psi_{\pm}\rangle$. The initial purity of the superposition and the balance between its two parts is characterized by the visibility of the beat signal at $\tau = 0$. This visibility exceeds 90%, indicating that the superposition is nearly perfect.

The mutual coherence time of the interfering photons is obtained from the damping of the quantum beat or, alternatively, from the width of the two-photon interference dip. In both cases, a coherence time of 460 ns (half width at $1/e$ dip depth) is observed, which exceeds the 64 ns decay time of the cavity, as well as the 27 ns lifetime of the atom's excited state. Hence, the intrinsic lifetimes do not limit the coherence. However, for perfectly transform limited photons, one would expect to see no decrease of the quantum-beat visibility for $\Delta \neq 0$, and no correlation at all for $\Delta = 0$. This is obviously not the case—a numerical fit to the measured data based on an analytical model [8] (solid lines in Fig. 3) shows that the observed coherence time can be explained by an inhomogeneous broadening of $\delta\omega/2\pi = 690$ kHz, which exceeds the 350 kHz bandwidth of transform limited photons. No specific broadening mechanism could be identified, and therefore we attribute this to several technical reasons: static and fluctuating magnetic fields affect the energies of the magnetic substates and spread the photon frequencies over a range of 160 kHz, and the trigger laser has a linewidth of 50 kHz, which is mapped to the photons. Moreover, diabatically generated photons lead to an additional broadening.

To summarize, we have observed the fourth-order interference of two individual photons impinging on a beam splitter in a time-resolved manner. With photons of different frequencies, a quantum beat is found in the correlation between the photodetections at the output ports of the beam splitter. This beat oscillates with the frequency difference of the interfering photons. The interference fringes are visible only for photons that are detected within their mutual coherence time. Moreover, our measurements reveal that identical photons coalesce; i.e., they leave the beam splitter as a pair, provided they do not dephase with respect to each other. Any deviation from perfect coalescence, observed for nonzero detection-time delay, can be attributed to a random dephasing due to an inhomogeneous broadening of the photon spectrum. We therefore conclude that a temporal filter, which accepts only time intervals between photodetections shorter than the mutual coherence time, is a way to obtain nearly perfect two-photon interference, even if the coherence properties of the photons are not ideal. This makes linear optical quantum computing [9] much more feasible with today's technology.

Moreover, we point out that the present experiment is formally equivalent to a setup composed of two independent atom-cavity systems, since the photon traveling along the optical fiber could as well be released directly from an independent (second) atom-cavity system. Provided the time the photons need to travel from the cavities to the detectors is much shorter than their mutual coherence time (as is in fact the case for mode B in our experiment), the first photodetection would establish an entanglement between the distant atom-cavity systems [12–15], since the states $|1_{A,B}\rangle$ and $|0_{A,B}\rangle$ refer in this case to these systems. This entanglement would live until it is destructively probed by a second photodetection. Our results therefore pave the way towards distributed quantum computing and teleportation of atomic quantum states [16,17].

This work was supported by the focused research program "Quantum Information Processing" and the SFB 631 of the Deutsche Forschungsgemeinschaft and by the European Union through the IST (QUBITS, QGATES) and IHP (QUEST, CONQUEST) programs.

[1] C. K. Hong, Z. Y. Ou, and L. Mandel, Phys. Rev. Lett. **59**, 2044 (1987).
[2] C. Santori, D. Fattal, J. Vučković, G. S. Solomon, and Y. Yamamoto, Nature (London) **419**, 594 (2002).
[3] Z. Y. Ou and L. Mandel, Phys. Rev. Lett. **61**, 54 (1988).
[4] A. Kuhn, M. Hennrich, and G. Rempe, Phys. Rev. Lett. **89**, 067901 (2002).
[5] M. Hennrich, T. Legero, A. Kuhn, and G. Rempe, Phys. Rev. Lett. **85**, 4872 (2000).
[6] A. Kuhn and G. Rempe, in *Experimental Quantum Computation and Information*, edited by F. D. Martini and C. Monroe (IOS Press, Amsterdam, 2002), Vol. 148, pp. 37–66.
[7] A. Kuhn, M. Hennrich, and G. Rempe, in *Quantum Information Processing*, edited by T. Beth and G. Leuchs (Wiley-VCH, Berlin, 2003), pp. 182–195.
[8] T. Legero, T. Wilk, A. Kuhn, and G. Rempe, Appl. Phys. B **77**, 797 (2003).
[9] E. Knill, R. Laflamme, and G. J. Milburn, Nature (London) **409**, 46 (2001).
[10] G. Rempe, R. J. Thompson, R. J. Brecha, W. D. Lee, and H. J. Kimble, Phys. Rev. Lett. **67**, 1727 (1991).
[11] G. T. Foster, L. A. Orozco, H. M. Castro-Beltran, and H. J. Carmichael, Phys. Rev. Lett. **85**, 3149 (2000).
[12] C. Cabrillo, J. I. Cirac, P. García-Fernández, and P. Zoller, Phys. Rev. A **59**, 1025 (1999).
[13] J. Hong and H.-W. Lee, Phys. Rev. Lett. **89**, 237901 (2002).
[14] X.-L. Feng, Z.-M. Zhang, X.-D. Li, S.-Q. Gong, and Z.-Z. Xu, Phys. Rev. Lett. **90**, 217902 (2003).
[15] D. E. Browne, M. B. Plenio, and S. F. Huelga, Phys. Rev. Lett. **91**, 067901 (2003).
[16] S. Bose, P. L. Knight, M. B. Plenio, and V. Vedral, Phys. Rev. Lett. **83**, 5158 (1999).
[17] S. Lloyd, M. S. Shahriar, J. H. Shapiro, and P. R. Hemmer, Phys. Rev. Lett. **87**, 167903 (2001).

RAPID COMMUNICATIONS

PHYSICAL REVIEW A **70**, 031601(R) (2004)

Dissociation of ultracold molecules with Feshbach resonances

Stephan Dürr, Thomas Volz, and Gerhard Rempe
Max-Planck-Institut für Quantenoptik, Hans-Kopfermann-Straße 1, 85748 Garching, Germany
(Received 26 May 2004; published 8 September 2004)

Ultracold molecules are associated from an atomic Bose-Einstein condensate by ramping a magnetic field across a Feshbach resonance. The reverse ramp dissociates the molecules. The kinetic energy released in the dissociation process is used to measure the widths of four Feshbach resonances in ^{87}Rb. This method to determine the width works remarkably well for narrow resonances even in the presence of significant magnetic-field noise. In addition, a quasimonoenergetic atomic wave is created by jumping the magnetic field across the Feshbach resonance.

DOI: 10.1103/PhysRevA.70.031601 PACS number(s): 03.75.Nt, 34.50.−s

The field of ultracold molecules has seen impressive progress over the course of the last year. A recent landmark achievement was the creation of a Bose-Einstein condensate (BEC) of molecules [1–4]. Presently, several experiments are exploring the crossover regime between BEC and BCS (Bardeen-Cooper-Schrieffer) superfluidity [4–8]. While these experiments associate bosonic dimers from fermionic atoms (see also Ref. [9]), there is also considerable interest in dimers associated from bosonic atoms [10–13]. Ultracold molecules are created by first cooling atoms to ultracold temperatures and then associating them to molecules using either photoassociation or a Feshbach resonance. In the latter case, the molecules are typically created by slowly ramping the magnetic field in the appropriate direction across the Feshbach resonance.

In this paper, we investigate the dissociation of molecules by ramping the magnetic field back through the resonance. The kinetic energy released in the dissociation depends on ramp speed and on the width of the resonance. This was previously used to determine the width of a fairly broad Feshbach resonance in Na [14]. We now used this method to determine the widths of four Feshbach resonances in ^{87}Rb. We discuss why the widths of narrow Feshbach resonances can be determined with this method even in the presence of significant magnetic-field noise. Indeed, three of the resonances investigated here are so narrow that their widths are not accessible otherwise. In addition, an outgoing quasimonoenergetic atomic wave is created by jumping the magnetic field across the resonance instead of ramping linearly in time. In this case, the atoms fly apart on the surface of a hollow sphere.

We start with a brief summary of the theoretical background [14–16]. A Feshbach resonance arises when a closed-channel bound state crosses an open-channel dissociation threshold when varying the magnetic field. Near this crossing, the bare states are coupled to dressed states. The energy ϵ of the bare molecular state with respect to the dissociation threshold depends on a good approximation linearly on the magnetic field B so that $\epsilon=(B-B_{\mathrm{res}})\Delta\mu$, where the slope $\Delta\mu$ is the difference in the magnetic moments between a molecule and a dissociated atom pair, and B_{res} is the position of the Feshbach resonance.

A long-lived molecule can only exist for $\epsilon<0$. Otherwise, the molecule dissociates spontaneously into a pair of unbound atoms due to the resonant coupling to the continuum of atomic pair states above the dissociation threshold. When a molecule at rest with $\epsilon>0$ dissociates, the energy ϵ is released as kinetic energy of the two atoms. Since total momentum is conserved and both atoms have equal mass, the atoms have equal kinetic energy ($E=\epsilon/2$ each) and precisely opposite momentum vectors. The decay rate Γ_{mol} of the molecules can be obtained from Fermi's golden rule, yielding [14]

$$\Gamma_{\mathrm{mol}}(\epsilon)=\frac{2|\Delta B\Delta\mu|}{\hbar}\left(\frac{ma_{\mathrm{bg}}^2}{\hbar^2}\epsilon\right)^{1/2} \tag{1}$$

for $\epsilon>0$, and $\Gamma_{\mathrm{mol}}=0$ otherwise. Here, ΔB is the width of the Feshbach resonance, m is the mass of an atom, and a_{bg} is the background value of the s-wave scattering length. Alternatively, Eq. (1) can be obtained from scattering theory, see, e.g., Eqs. (25) and (42) in Ref. [17] with $\Gamma_m=\hbar\Gamma_{\mathrm{mol}}$.

Consider a magnetic-field ramp that is linear in time with $d\epsilon/dt>0$. In this case, the molecule fraction f decays as [14]

$$f(\epsilon)=\exp\left(-\frac{4|\Delta B|}{3\hbar\left|\frac{dB}{dt}\right|}\sqrt{\frac{ma_{\mathrm{bg}}^2}{\hbar^2}}\epsilon^{3/2}\right) \tag{2}$$

for $\epsilon>0$, and $f=1$ otherwise. The mean kinetic energy of a single atom after the dissociation is then [14,15]

$$\langle E\rangle=\frac{1}{2}\Gamma\left(\frac{5}{3}\right)\left(\frac{3\hbar\left|\frac{dB}{dt}\right|}{4|\Delta B|}\sqrt{\frac{\hbar^2}{ma_{\mathrm{bg}}^2}}\right)^{2/3}, \tag{3}$$

where Γ is the Euler gamma function with $\Gamma\left(\frac{5}{3}\right)\approx 0.903$. This relation makes it possible to determine the width ΔB of a Feshbach resonance from a measurement of $\langle E\rangle$, because a_{bg} is typically known with much better accuracy than ΔB. Unlike previous methods, this method of measuring ΔB does not depend on knowledge of the initial atomic density distribution.

The probability density D for the velocity $\vec{v}$ of the dissociated atoms is easily obtained from Eq. (2), yielding

1050-2947/2004/70(3)/031601(4)/$22.50

$$D(\vec{v})d^3v = \frac{3}{4\pi v_0^3}\exp\left(-\frac{|\vec{v}|^3}{v_0^3}\right)d^3v, \qquad (4)$$

where $\langle E\rangle=(m/2)v_0^2\Gamma(\frac{5}{3})$. Using a time-of-flight method, this velocity distribution is converted into a position distribution, which is measured using absorption imaging.

In the experiment, the velocity distribution of the molecules before dissociation has a finite width. The result is an offset energy E_0 in Eq. (3), but the shape of the velocity distribution Eq. (4) is hardly affected, because E_0 is small.

A fit of Eq. (4) to the absorption images would be cumbersome, because no analytic solution is known for the integral of Eq. (4) along one or two coordinate axes. We therefore fit a two-dimensional Gaussian to the absorption images and extract $\langle E\rangle$ of the Gaussian fit function. In order to analyze the error made by this choice of the fit function, we numerically integrate Eq. (4) along one coordinate axis for a specific value of $\langle E\rangle$ and fit a two-dimensional Gaussian to this. The resulting best-fit value $\langle E\rangle$ of the Gaussian is a factor of $\sim$1.18 larger than the true value $\langle E\rangle$ of Eq. (4). We correct the kinetic energies in our data analysis by this factor.

An experimental cycle begins with the production of a BEC of ^{87}Rb atoms in a magnetic trap. The BEC is then transferred to an optical dipole trap and a magnetic field of up to $\sim$1000 G is applied. The atomic spin is prepared in the absolute ground state $|f,m_f\rangle=|1,1\rangle$. This state has many Feshbach resonances [18].

The dipole trap consists of two beams from a Nd:yttrium aluminum garnet (YAG) laser that cross at right angles. One beam is horizontal, the other subtends an angle of 25° with the horizontal plane. The horizontal beam has a beam waist ($1/e^2$ radius of intensity) of 40 μm and a power of 45 mW, the other beam has 55 μm and 20 mW. Trap frequencies of $2\pi\times(80,110,170)$ Hz were measured with parametric heating.

In our previous experiments [12,19], an undesired reflection of the horizontal beam from an uncoated inside surface of the glass cell housing the BEC caused a weak standing wave. This created a one-dimensional optical lattice with a well depth of $\sim k_B\times 0.6$ μK, which exceeds typical values of k_BT and of the chemical potential. The horizontal beam is now tilted by a few degrees with respect to the glass surface, thus eliminating this standing wave. This improves the trap loading substantially, because atoms from the wings of the trap are now free to move to the central region. Now, a BEC of typically 6×10^5 atoms can be held in the crossed dipole trap, with a small thermal fraction of less than 1×10^5 atoms. The in-trap peak density in the BEC is typically 5×10^{14} cm^{-3}.

Ultracold molecules are created by ramping the magnetic field slowly downward through one of the Feshbach resonances, as described in Ref. [12]. About 2 ms before the molecule creation, the atoms are released from the dipole trap. The fraction of the population that is converted into molecules is $\sim$10% for the broad resonances at 685 and 1007 G, and it is $\sim$3% for the narrower resonances at 632 and 912 G. We could not detect molecules when working at even narrower resonances with a width predicted to be ΔB $\sim$0.2 mG. We speculate that this is because the slow molecule-creation ramp might suffer from magnetic-field noise. After the molecule creation, a Stern-Gerlach field is applied to separate the molecules from the remaining atoms. Next, the magnetic field is ramped upward through the Feshbach resonance to dissociate the molecules. Then the atoms fly freely for up to 11 ms, before an absorption image of the cloud is taken on a video camera. The mean kinetic energy is extracted from the image as described above.

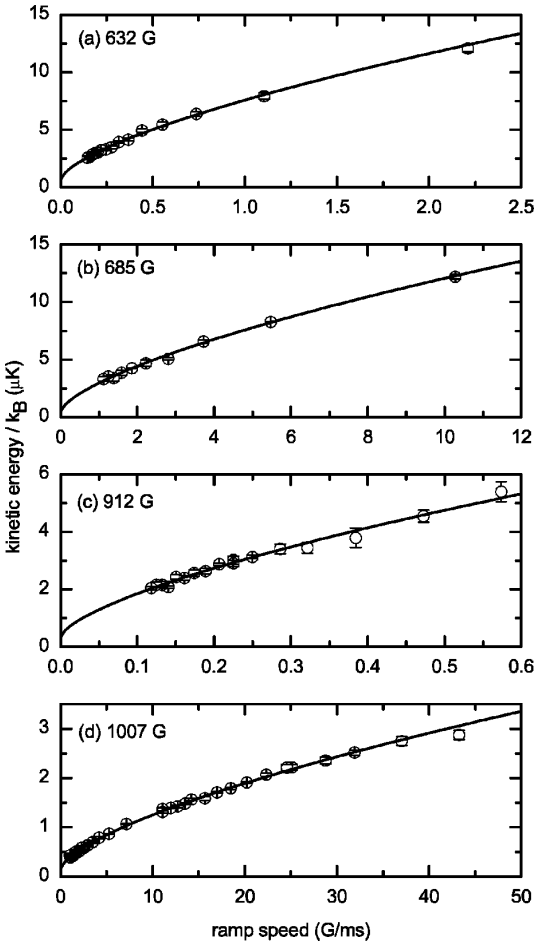

FIG. 1. Mean kinetic energy per atom as a function of the speed of the dissociation ramp. Parts (a), (b), (c), and (d) were measured at Feshbach resonances at 632, 685, 912, and 1007 G, respectively. The solid lines show fits of Eq. (3) to the data. The best-fit values are shown in Table I.

Experimental results as a function of ramp speed are shown in Fig. 1 for the four broadest Feshbach resonances of the state $|1,1\rangle$. Solid lines show fits of Eq. (3) to the data, with the width of the resonance ΔB and the offset energy E_0 as free fit parameters. The best-fit values are shown in Table I, using the theory value $a_{bg}=100.5$ Bohr radii for the state $|1,1\rangle$ from Ref. [19]. For the resonances at 632, 912, and 1007 G, the measured widths agree well with the theoretical predictions and with a previously measured value, both also

TABLE I. Position B_{res} and width ΔB of the Feshbach resonances. ΔB_{fit} is the best-fit value obtained from the measurement in Fig. 1. ΔB_{th} is the theoretical prediction from Ref. [18]. ΔB_{prev} is the result of a previous measurement in Ref. [19].

B_{res} (G)	ΔB_{fit} (mG)	ΔB_{th} (mG)	ΔB_{prev} (mG)
632	1.3(2)	1.5	
685	6.2(6)	17	
912	1.3(2)	1.3	
1007	210(20)	170(30)	200(30)

shown in Table I. The good agreement shows that the dissociation of molecules can be used as a reliable method to determine ΔB. The resonance at 685 G, however, is a factor of $\sim$2.7 narrower than predicted. More recent calculations [20] predict a width of 10 mG for this resonance, which is much closer to the value measured here.

It is surprising that a width as small as $\Delta B = 1.3$ mG can be measured with our setup, because the magnetic-field noise is most likely larger than this value. The observed linewidths of microwave transitions measured with 50 ms long pulses set an experimental upper bound on magnetic-field noise of 4 mG (rms). An attempt to directly measure the magnetic-field dependence of the scattering length $a(B)$ for the 632 or 912 G resonance would therefore most likely suffer strongly from the magnetic-field noise.

There are two reasons why such a small ΔB can be measured with the method presented here nonetheless. First, the dissociation process is pretty fast, e.g., $\Gamma_{mol} \sim 10$ kHz for $\epsilon = k_B \times 5\ \mu$K at the 912 G resonance. Therefore, low-frequency magnetic-field noise merely shifts the exact time of dissociation but has no effect on the actual ramp speed during the rather short decay time. Second, by choosing fast enough ramp speeds, the experiment is operated in a regime where the relevant decay happens at magnetic fields that are pretty far away from B_{res}. A typical decay energy of $\epsilon = k_B \times 5\ \mu$K corresponds to $B - B_{res} \sim 25$ mG for the 912 G resonance. Here, the magnetic-field noise has little effect on the molecule-decay rate.

In addition to the possibility to measure the widths of Feshbach resonances, the dissociation of molecules into atom pairs can also be used to produce a monoenergetic spherical wave of atoms. To this end, the magnetic field is jumped across the resonance as fast as possible and then held at a fixed value B_{final}. If the jump is fast enough, there will be hardly any dissociation during the jump. Therefore all molecules dissociate at B_{final}, thus creating atoms with a fixed amount of kinetic energy. Hence, the atoms fly apart on the surface of a hollow sphere during the subsequent free flight.

The laser beam used in absorption imaging integrates this density distribution along its propagation direction, thus yielding a two-dimensional image that shows a ring, with a nonzero density in the center. Such an image is shown for the 685 G resonance in Fig. 2(a). Due to the initial momentum spread of the molecules the dissociated atoms are not perfectly monoenergetic. This smears the atomic distribution around the ring. The contrast is still good enough to see a clear dip in the center of the line profile in Fig. 2(b). The data

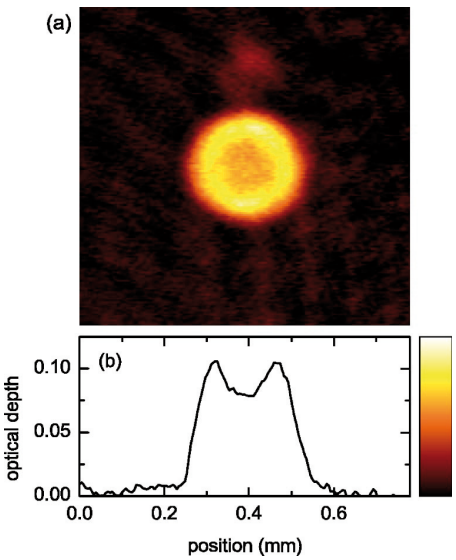

FIG. 2. (Color online) (a) Monoenergetic spherical wave of atoms, created by dissociation of molecules when jumping the magnetic field across the Feshbach resonance. The atoms fly apart on the surface of a hollow sphere. The absorption-imaging beam integrates the three-dimensional density profile along one direction. The observed two-dimensional image therefore shows a ring, with a nonzero density in the center. The image was averaged over $\sim$100 experimental shots. (b) Line profile across the center of the image. The dip in the center is clearly visible.

were taken with 5.5 ms time of flight after the dissociation and with $B_{final} - B_{res} \sim 40$ mG corresponding to $\Gamma_{mol} \sim 20$ kHz.

Technically, the creation of a sharp corner between the magnetic-field jump and the plateau at B_{final} is difficult. The experimental requirements concerning the sharpness of this corner are more stringent with broader resonances because of the faster molecule-decay rates. We believe that this is why we were unable to observe a dip as in Fig. 2(b) at the 1007 G resonance with the given bandwidth of the servo that controls our magnetic field.

The scheme with the jump in the magnetic field can be easily generalized by using an arbitrary shape of the dissociation ramp, which makes it possible to tailor the time and energy dependence of the outgoing atomic wave function.

As mentioned earlier, one expects that after the dissociation of molecules the created atom pairs should have precisely opposite momentum vectors, given that the molecules had a negligible momentum spread initially. A detection of this pair correlation might be an interesting subject of future investigations.

In conclusion, the dissociation of molecules with a linear magnetic-field ramp is a simple and reliable technique to determine the widths of Feshbach resonances, even in the presence of magnetic-field noise. We measured the widths of four Feshbach resonances in ^{87}Rb, thereby covering more than two orders of magnitude in ΔB. We also showed that dissociation of molecules can be used to create a quasimonoenergetic atomic wave.

We thank Cheng Chin for pointing out the possibility of creating monoenergetic atoms by jumping the magnetic field across the resonance. We also acknowledge fruitful discussions with Thorsten Köhler and Paul Julienne. This work was supported by the European-Union Network "Cold Quantum Gases."

[1] M. Greiner, C. A. Regal, and D. S. Jin, Nature (London) **426**, 537 (2003).
[2] S. Jochim, M. Bartenstein, A. Altmeyer, G. Hendl, S. Riedl, C. Chin, J. Hecker-Denschlag, and R. Grimm, Science **302**, 2101 (2003).
[3] M. W. Zwierlein, C. A. Stan, C. H. Schunck, S. M. Raupach, S. Gupta, Z. Hadzibabic, and W. Ketterle, Phys. Rev. Lett. **91**, 250401 (2003).
[4] T. Bourdel, L. Khaykovich, J. Cubizolles, J. Zhang, F. Chevy, M. Teichmann, L. Tarruell, S. J. Kokkelmans, and C. Salomon, e-print cond-mat/0403091.
[5] C. A. Regal, M. Greiner, and D. S. Jin, Phys. Rev. Lett. **92**, 040403 (2004).
[6] M. Bartenstein, A. Altmeyer, S. Riedl, S. Jochim, C. Chin, J. Hecker-Denschlag, and R. Grimm, Phys. Rev. Lett. **92**, 120401 (2004).
[7] M. W. Zwierlein, C. A. Stan, C. H. Schunck, S. M. Raupach, A. J. Kerman, and W. Ketterle, Phys. Rev. Lett. **92**, 120403 (2004).
[8] J. Kinast, S. L. Hemmer, M. E. Gehm, A. Turlapov, and J. E. Thomas, Phys. Rev. Lett. **92**, 150402 (2004).
[9] K. E. Strecker, G. B. Partridge, and R. G. Hulet, Phys. Rev. Lett. **91**, 080406 (2003).
[10] E. A. Donley, N. R. Claussen, S. T. Thomson, and C. E. Wieman, Nature (London) **417**, 529 (2002).
[11] J. Herbig, T. Kraemer, M. Mark, T. Weber, C. Chin, H.-C. Nägerl, and R. Grimm, Science **301**, 1510 (2003).
[12] S. Dürr, T. Volz, A. Marte, and G. Rempe, Phys. Rev. Lett. **92**, 020406 (2004).
[13] K. Xu, T. Mukaiyama, J. R. Abo-Shaeer, J. K. Chin, D. E. Miller, and W. Ketterle, Phys. Rev. Lett. **91**, 210402 (2003).
[14] T. Mukaiyama, J. R. Abo-Shaeer, K. Xu, J. K. Chin, and W. Ketterle, Phys. Rev. Lett. **92**, 180402 (2004).
[15] K. Goral, T. Köhler, S. A. Gardiner, E. Tiesinga, and P. Julienne, e-print cond-mat/0312178.
[16] V. A. Yurovsky and A. Ben-Reuven, e-print cond-mat/0402334.
[17] E. Timmermans, P. Tommasini, M. Hussein, and A. Kerman, Phys. Rep. **315**, 199 (1999).
[18] A. Marte, T. Volz, J. Schuster, S. Dürr, G. Rempe, E. G. van Kempen, and B. J. Verhaar, Phys. Rev. Lett. **89**, 283202 (2002).
[19] T. Volz, S. Dürr, S. Ernst, A. Marte, and G. Rempe, Phys. Rev. A **68**, 010702(R) (2003).
[20] Eric van Kempen and Boudewijn Verhaar (personal communication).

PRL 94, 033002 (2005) PHYSICAL REVIEW LETTERS week ending 28 JANUARY 2005

Normal-Mode Spectroscopy of a Single-Bound-Atom–Cavity System

P. Maunz, T. Puppe, I. Schuster, N. Syassen, P. W. H. Pinkse, and G. Rempe
Max-Planck-Institut für Quantenoptik, Hans-Kopfermann-Strasse 1, D-85748 Garching, Germany
(Received 18 June 2004; published 27 January 2005)

The energy-level structure of a single atom strongly coupled to the mode of a high-finesse optical cavity is investigated. The atom is stored in an intracavity dipole trap and cavity cooling is used to compensate for inevitable heating. Two well-resolved normal modes are observed both in the cavity transmission and the trap lifetime. The experiment is in good agreement with a Monte Carlo simulation, demonstrating our ability to localize the atom to within $\lambda/10$ at a cavity antinode.

DOI: 10.1103/PhysRevLett.94.033002 PACS numbers: 32.80.Pj, 42.50.–p

Experimental research in quantum information science with atoms and ions [1] is based on the ability to control individual particles in a truly deterministic manner. While spectacular advances have recently been achieved with trapped ions interacting via phonons [2,3], the precise control of the motion of atoms exchanging photons inside an optical cavity [4] or emitting single photons on demand [5,6] is still a challenge. Although very successful, experiments in cavity quantum electrodynamics with single laser-cooled atoms [7–9] are complicated by the motion of the atom in the standing-wave mode of the optical cavity [10,11]. The lack of control over the atomic motion is mainly due to the heating effects of the various laser fields employed to trap and excite the atom inside the cavity in combination with the limited ability to cool the atom between two highly reflecting mirrors facing each other at a microscopic distance [12,13]. Only recently, good localization of the atom at an antinode of the cavity mode has been achieved by applying optical molasses [14] or a novel cavity cooling force [15] to a trapped atom.

In this Letter, we go one step further and employ cavity cooling to probe the energy spectrum of a single trapped atom strongly coupled to a high-finesse resonator [16,17]. In previous experiments using thermal beams, the spectrum was explored only for many atoms [18,19], one atom on average [20,21], or single cold atoms transiting the cavity [22]. Our experiment is the first in which the normal-mode (or vacuum-Rabi) splitting of a single atom trapped inside a cavity is observed. Both the cavity transmission and the trapping time are investigated. The results agree with a Monte Carlo simulation and demonstrate that remarkably good control can be obtained over this fundamental quantum system.

The cavity used in the experiment (Fig. 1) has a finesse $\mathcal{F} = 4.4 \times 10^5$, a mode waist $w_0 = 29\ \mu$m, and a length $l = 122\ \mu$m [15]. A single TEM_{00} mode of the cavity is near resonant with the $5\,^2S_{1/2}F = 3, m_F = 3 \leftrightarrow 5\,^2P_{3/2}F = 4, m_F = 4$ transition of ^{85}Rb at $\lambda = 780.2$ nm. The atom-cavity coupling at an antinode of the standing wave, $g/2\pi = 16$ MHz, is large compared to the amplitude decay rates of the atomic excitation, $\gamma/2\pi = 3$ MHz, and the cavity field, $\kappa/2\pi = 1.4$ MHz. Strong coupling is reached, resulting in critical photon and atom numbers $n_0 = \gamma^2/2g^2 \approx 1/60$ and $N_0 = 2\gamma\kappa/g^2 \approx 1/30$, respectively. This strongly coupled atom-cavity system is probed by a weak near-resonant beam impinging on the cavity. The probe beam is also used to cool the axial motion of the atom. A second TEM_{00} mode supported by the cavity, two free spectral ranges red detuned with respect to the near-resonant mode, is used to trap the atom in the cavity. This mode is resonantly excited by a trap laser at 785.3 nm. The far-detuned light is generated by a grating- and current-stabilized laser diode and has a linewidth of about 20 kHz rms. The cavity length is continuously stabilized to this trap laser. The two light fields transmitted through the cavity are separated by a holographic grating. The trap light is directed to a photomultiplier, whereas the probe light is further filtered by a narrow-band interference filter and then detected by two single-photon counting modules. The setup achieves a quantum efficiency of 32% for the probe light transmitted through the cavity and a suppression of the trap light on the photon counting modules of more than 70 dB.

Laser-cooled ^{85}Rb atoms are injected from below by means of an atomic fountain [8]. The parameters of the fountain are chosen to get well-separated signals of single atoms which have a velocity below 10 cm/s. The atoms are guided into the antinodes of the far-detuned field by a weak dipole potential with a trap depth of 400 μK. The near-resonant light used to detect the atom is blue detuned with

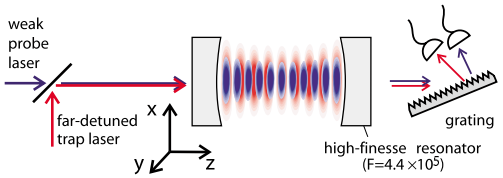

FIG. 1 (color online). Experimental setup: The high-finesse cavity is excited by a weak near-resonant probe field and a strong far-red-detuned trap field. ^{85}Rb atoms are injected from below. Behind the cavity, the two light fields are separated by a grating and measured with independent photodetectors.

0031-9007/05/94(3)/033002(4)$23.00

PRL 94, 033002 (2005) PHYSICAL REVIEW LETTERS week ending 28 JANUARY 2005

respect to the atomic resonance, $\Delta_a = \omega_p - \omega_a = 2\pi \times 35$ MHz, and resonant with the cavity, $\Delta_c = \omega_p - \omega_c = 0$. The presence of the atom inside the cavity tunes the atom-cavity system out of resonance with the probe laser. The resulting dramatic drop of the transmission allows the detection of an atom with a high signal-to-noise ratio and a high bandwidth. Since the atoms are guided into the antinodes of the far-detuned field, only atoms which enter near the cavity center, where the antinodes of the two light fields coincide, are strongly coupled to the probe beam and cause a deep drop of the transmission. Upon detection of a strongly coupled atom in the cavity, the trap depth of the conservative dipole potential is increased to values between 1.3 and 1.9 mK. This compensates for the kinetic energy of the atom and leads to trapping. It is noteworthy that all atoms which activated the trigger are captured in the trap. We estimate the probability to trap more than one atom at a time to be below 0.4%.

The storage time of a single atom in the far-detuned dipole trap without any near-resonant light is about 30 ms as described in Ref. [15]. The storage time is limited by axial parametric heating due to intensity fluctuations of the intracavity dipole trap. The dipole force of the probe light, which caused a shift and a distortion of the measured spectra in earlier experiments [4,22], can be neglected because it is much weaker than the dipole force of the far-detuned light. However, depending on the relative frequencies of the atomic transition, cavity resonance, and probe laser, nonconservative forces can heat or cool the atom [23–25] mainly along the cavity axis. In order to measure the atom-cavity spectrum, it is necessary to probe the system at detunings for which these forces lead to strong heating. This quickly reduces the atomic localization, and severely limits the available probe time by boiling the atom out of the trap. To compensate the disastrous effect of heating, cooling intervals are applied to reestablish strong coupling of the atom to the cavity. This can be achieved by switching the probe laser to parameters for which the velocity-dependent forces lead to efficient cooling [15]. Of course, in the radial direction, the atom is heated by scattering photons of the near-resonant probe light. Since there is no radial cooling mechanism, this heating mechanism contributes to the experimentally observed loss rate of atoms from the trap.

These considerations lead to the following protocol to perform the atom-cavity spectroscopy: After capturing the atom in the trap, a 500 μs long cooling interval is used to improve the localization of the atom and to determine its coupling strength by monitoring the cavity transmission with a resonant probe laser ($\Delta_c = 0$). This is followed by a 100 μs long probe interval, where the frequency of the probe laser is changed to an adjustable but fixed value Δ_c. This sequence of cooling and probing intervals is then repeated. As long as the atom is stored in the trap, the transmission during the cooling intervals is low, while it is high if the atom has left. The end of the last cooling interval during which the transmission is below 80% of the empty-cavity transmission determines the exit time of the atom. Within this sequence, each probe interval is enclosed by two cooling intervals in which the coupling strength before and after the probe interval can be determined independently of the probing. This allows the exclusion of probe intervals during which the atom is only weakly coupled to the cavity mode. We find that in about 25% of the probe intervals in which an atom resides in the trap, both cooling intervals have a transmission below 2% of that of the empty cavity. These probe intervals are defined as ''strongly coupled'' and are used for further analysis. The whole protocol is repeated for different atoms and different values of Δ_c.

Figure 2 shows the average cavity transmission during the strongly coupled probe intervals as a function of the probe detuning. The four spectra are obtained for different atom-cavity detunings and all show two well-resolved normal modes. Together, they display the avoided crossing between the atomic and the cavity resonances [26]. The atom-cavity detuning is adjusted by tuning the atomic

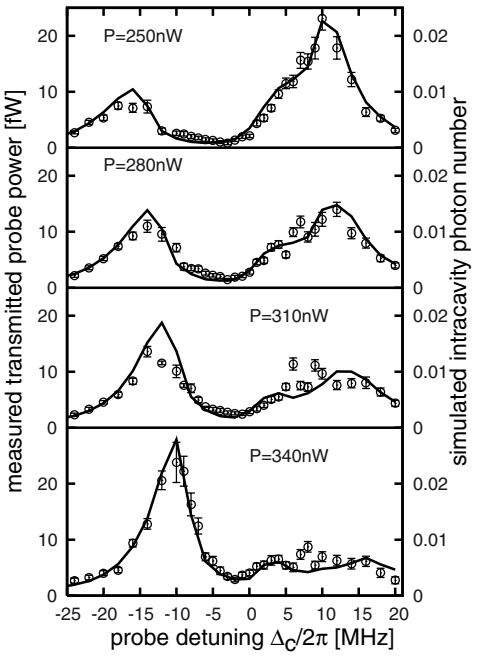

FIG. 2. Transmission of the cavity containing a single trapped and strongly coupled atom (circles). The detuning between the cavity and the atom is adjusted by tuning the Stark shift of the atom via the trapping-field power expressed in terms of the transmitted power, P. The average transmission during probe intervals for which the atom is found to be strongly coupled by independent qualification (see text) shows well-resolved normal-mode peaks. On average each point includes the data from about 350 probe intervals collected from between 35 and 1000 atoms. A Monte Carlo simulation (solid lines) describes the data well.

PRL 94, 033002 (2005) PHYSICAL REVIEW LETTERS week ending 28 JANUARY 2005

resonance via the dynamic Stark effect induced by the far-detuned trap light. The induced (position-dependent) shift, Δ_S, of the atomic resonance frequency is proportional to the trap depth. For a transmitted power of the trap light of about 280 nW the dynamic Stark shift compensates the initial atom-cavity detuning of $2\pi \times 35$ MHz. The eigenstates of the atom-cavity system (dressed states) are superpositions of the atomic ground state together with a cavity photon and the atomic excited state without a cavity photon. Since the probe laser excites only the cavity mode, the excitation of a dressed state is proportional to the contribution of the cavity state to the dressed state. This contribution depends on the atom-cavity detuning and explains the observation that the height of the left normal-mode peak increases with increasing Stark shift, while that of the right peak decreases. For zero detuning between atom and cavity (about $P = 280$ nW), the contributions from the atomic and the cavity states are equal so that the normal modes have the same height and reach a minimum splitting of $2g$. Here, the observed splitting of about $2 \times 2\pi \times 12$ MHz is only slightly smaller than the maximal possible splitting of $2 \times 2\pi \times 16$ MHz expected for a pointlike atom at rest at an antinode. This proves that the atom is localized in the regime of strong coupling with $g \gg (\gamma, \kappa)$.

For a stationary atom, the widths of the two normal modes are given by a weighted mean of the atomic and cavity linewidths. However, since the atom is not fixed at an antinode of the probe field, but oscillates in the trap, the atom-cavity coupling is time dependent. This leads to fluctuating frequencies of the normal modes, and therefore the measured spectra are broadened.

The different widths of the normal modes of the spectra in Fig. 2 can be explained by taking into account the position-dependent Stark shift for a moving atom: An atom close to an antinode of the trapping field experiences a larger Stark shift, which shifts both normal modes to larger probe detunings. Near the center of the cavity, where the antinodes of both light fields overlap, this atom is also close to an antinode of the probe field. Therefore its coupling to the cavity is also larger. This increases the splitting of the normal modes. Consequently, the frequency of the left normal mode is only weakly dependent on the atomic position while the two effects add up for the right normal mode. This broadens the right peak to a greater extent than the left.

The exact width and line shape of the measured normal modes are influenced by the details of the atomic motion in the trap. Cavity heating and cooling strongly depend on the atomic position and the frequency of the probe laser. These forces determine the atomic motion in a complex way. In order to obtain more information on the atomic motion we compare the measured spectra with the results of a Monte Carlo simulation. Here a pointlike atom is propagated in space according to a stochastic differential equation for the atomic position and momentum. The forces and momentum diffusion are given by analytic equations for the combined atom-cavity-trap system. Parametric heating by the dipole trap is implemented by a randomly changing potential depth. To model the experiment in detail, single atoms are injected at random positions into the mode. Upon activating the trigger, the trap depth of the trapping field is increased, and the atom is exposed to the alternating cooling and probing scheme. The atomic trajectory is recorded until the atom leaves the cavity. The simulated transmission is evaluated in the same way as the experimental data.

Results are also shown in Fig. 2 and agree well with the experimental data if the power of the trapping field is reduced by 30% with respect to the intracavity power determined from the measured cavity transmission. This discrepancy could be explained by different transmissions of the two cavity mirrors. For consistency, the probe light power in the simulation is reduced by the same amount. The simulation also allows one to calculate the spatial probability distribution of the atom in the trap. The axial distribution has a width (FWHM) of $\lambda/7$ if all probe intervals are included. If only strongly coupled probe intervals (as defined above) are considered, the atom is axially confined to a width of $\lambda/10$ around the antinodes of the dipole trap. The probability distribution of the simulated atom-cavity coupling (in three dimensions) is shown in Fig. 3. It shows that our selection scheme eliminates the occurrence of probe intervals with weak atom-cavity coupling and an average coupling of about $2\pi \times 13$ MHz is reached. This agrees well with the experimentally achieved coupling of $2\pi \times 12$ MHz.

Further characterization of the normal modes can be obtained by investigating the average storage time of the atom in the trap as a function of the detuning during the probe intervals. While the atom is probed, additional heating can lead to a loss of the atom from the trap. The probe-induced loss rate is shown in Fig. 4. These spectra also

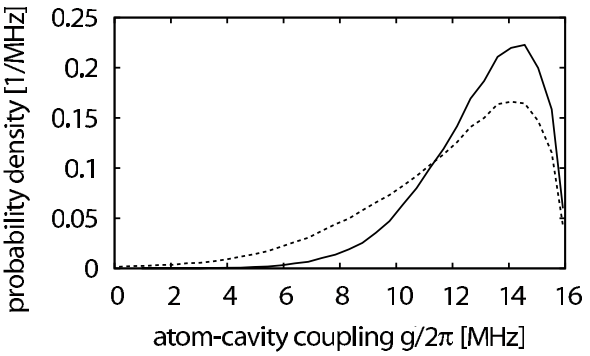

FIG. 3. Simulated probability distribution of the atom-cavity coupling for all probe intervals (dotted line) and for the strongly coupled intervals (solid line). Qualification completely eliminates the occurrence of probe intervals with weak coupling, $g \lesssim (\gamma, \kappa)$.

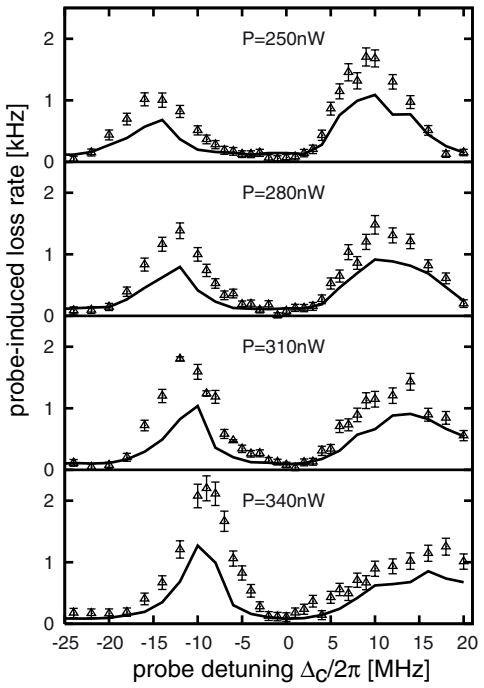

FIG. 4. Probe-induced loss rate of atoms from the trap (triangles) for different detunings between cavity and atom, adjusted by varying the trapping-field power. No qualification is employed. The experiment is in qualitative agreement with a Monte Carlo simulation (solid lines): the observed frequencies, widths, and relative heights of the normal-mode peaks are well described by the simulation. Only the absolute value of the measured rate exceeds that of the simulation. This could be explained by fluctuations of experimental parameters not taken into account in the simulation, e.g., the lack of shot noise in the modeling of atom capture. For all probe detunings the simulated atomic excitation is below 1.4%.

show two well-resolved peaks at detunings for which the excitation of the system is high. The measurements are in qualitative agreement with our Monte Carlo simulation. The simulation shows that for zero and large probe detunings, spontaneous emission accounts for about 75% of the probe-induced loss rate. On the normal-mode resonances, momentum diffusion caused by dipole-force fluctuations of the probe light generates additional heating, which causes more than 80% of the probe-induced loss rate. This makes the normal modes clearly visible in the probe-induced loss rate.

In conclusion, cavity cooling has been applied to reliably localize a single trapped atom in the strong-coupling region of a high-finesse cavity. Two well-resolved normal modes are observed both in cavity transmission and the atomic loss rate from the trap. The ability to individually excite the normal modes of a bound atom-cavity system opens up a wealth of new possibilities including the realization of a quantum-logic gate [27] or the control of the propagation of a light pulse [28] with exactly one atom.

[1] C. Monroe, Nature (London) **416**, 238 (2002).
[2] M. Riebe *et al.*, Nature (London) **429**, 734 (2004).
[3] M. D. Barrett *et al.*, Nature (London) **429**, 737 (2004).
[4] P. Münstermann, T. Fischer, P. Maunz, P. W. H. Pinkse, and G. Rempe, Phys. Rev. Lett. **84**, 4068 (2000).
[5] A. Kuhn, M. Hennrich, and G. Rempe, Phys. Rev. Lett. **89**, 067901 (2002).
[6] J. McKeever *et al.*, Science **303**, 1992 (2004).
[7] H. Mabuchi, Q. A. Turchette, M. S. Chapman, and H. J. Kimble, Opt. Lett. **21**, 1393 (1996).
[8] P. Münstermann, T. Fischer, P. W. H. Pinkse, and G. Rempe, Opt. Commun. **159**, 63 (1999).
[9] J. A. Sauer, K. M. Fortier, M. S. Chang, C. D. Hamley, and M. S. Chapman, Phys. Rev. A **69**, 051804(R) (2004).
[10] P. W. H. Pinkse, T. Fischer, P. Maunz, and G. Rempe, Nature (London) **404**, 365 (2000).
[11] C. J. Hood, T. W. Lynn, A. C. Doherty, A. S. Parkins, and H. J. Kimble, Science **287**, 1447 (2000).
[12] J. Ye, D. W. Vernooy, and H. J. Kimble, Phys. Rev. Lett. **83**, 4987 (1999).
[13] T. Fischer, P. Maunz, P. W. H. Pinkse, T. Puppe, and G. Rempe, Phys. Rev. Lett. **88**, 163002 (2002).
[14] J. McKeever *et al.*, Phys. Rev. Lett. **90**, 133602 (2003).
[15] P. Maunz *et al.*, Nature (London) **428**, 50 (2004).
[16] J. J. Sanchez-Mondragon, N. B. Narozhny, and J. H. Eberly, Phys. Rev. Lett. **51**, 550 (1983); **51**, 1925(E) (1983).
[17] G. S. Agarwal, Phys. Rev. Lett. **53**, 1732 (1984).
[18] Y. Zhu *et al.*, Phys. Rev. Lett. **64**, 2499 (1990).
[19] J. Gripp, S. L. Mielke, and L. A. Orozco, Phys. Rev. A **56**, 3262 (1997).
[20] R. J. Thompson, G. Rempe, and H. J. Kimble, Phys. Rev. Lett. **68**, 1132 (1992).
[21] J. J. Childs, K. An, M. S. Otteson, R. R. Dasari, and M. S. Feld, Phys. Rev. Lett. **77**, 2901 (1996).
[22] C. J. Hood, M. S. Chapman, T. W. Lynn, and H. J. Kimble, Phys. Rev. Lett. **80**, 4157 (1998).
[23] G. Hechenblaikner, M. Gangl, P. Horak, and H. Ritsch, Phys. Rev. A **58**, 3030 (1998).
[24] P. Münstermann, T. Fischer, P. Maunz, P. W. H. Pinkse, and G. Rempe, Phys. Rev. Lett. **82**, 3791 (1999).
[25] K. Murr, J. Phys. B **36**, 2515 (2003).
[26] P. Meystre and M. Sargent III, *Elements of Quantum Optics* (Springer-Verlag, Berlin, 1999), 3rd ed.
[27] Q. A. Turchette, C. J. Hood, W. Lange, H. Mabuchi, and H. J. Kimble, Phys. Rev. Lett. **75**, 4710 (1995).
[28] Y. Shimizu *et al.*, Phys. Rev. Lett. **89**, 233001 (2002).

PRL **94,** 053604 (2005) PHYSICAL REVIEW LETTERS week ending 11 FEBRUARY 2005

Transition from Antibunching to Bunching in Cavity QED

Markus Hennrich,* Axel Kuhn, and Gerhard Rempe

Max-Planck-Institut für Quantenoptik, Hans-Kopfermann-Strasse 1, D-85748 Garching, Germany

(Received 4 June 2004; published 10 February 2005)

The photon statistics of the light emitted from an atomic ensemble into a single field mode of an optical cavity is investigated as a function of the number of atoms. The light is produced in a Raman transition driven by a pump laser and the cavity vacuum, and a recycling laser is employed to repeat this process continuously. For weak driving, a smooth transition from antibunching to bunching is found for about one intracavity atom. Remarkably, the bunching peak develops within the antibunching dip. The observed behavior is well explained by a model describing an ensemble of independent emitters.

DOI: 10.1103/PhysRevLett.94.053604 PACS numbers: 42.50.Dv, 42.50.Fx, 42.55.Ye, 42.65.Dr

The photon statistics of light reveals whether it originates from a classical or a quantum source like a single atom. These sources can be distinguished by their intensity correlation function, $g^{(2)}(\tau)$ [1]. Classical light fulfills the Cauchy-Schwarz inequality, $g^{(2)}(0) \geq g^{(2)}(\tau)$, whereas light that violates this inequality must be described by the laws of quantum physics. In this case, a local minimum at $\tau = 0$ is found, i.e. $g^{(2)}(0) < g^{(2)}(\tau)$, which is defined as antibunching [2]. First experiments demonstrating antibunching were performed with a weak beam of atoms [3]. Limitations imposed by number fluctuations [4] were later eliminated by using a single emitter [5–11]. The deterministic control of the nonclassical light radiated by a single emitter [12–18] has interesting applications, e.g., in quantum information processing. Classical bunching, $g^{(2)}(0) > g^{(2)}(\tau)$, has been observed in the fluorescence of a large number of independently radiating atoms as early as 1956 [19], and has regained new interest in the context of cold-atom physics [20,21].

A smooth transition between antibunching and bunching is expected if the number of atoms gradually increases. Such a transition has not been observed so far, since a good photon-collection efficiency, and thus a large solid angle, is essential to obtain a photon count rate large enough to discriminate the antibunching signal from background noise, while spatial coherence of the detected light is required to observe bunching. For a distributed ensemble of atoms, this calls for a small solid angle. Obviously, these two requirements contradict each other, making the experiment difficult in the interesting regime of just a few radiating particles.

In the work presented here, all emitters are coupled to a single mode in a high-finesse optical cavity. Only the light in this mode is investigated, so that spatial coherence is granted. At the same time, the enhanced spontaneous emission into the cavity mode gives a good photon-collection efficiency. The experiment is performed in a regime where an emitted photon leaves the cavity before being reabsorbed and before affecting other atoms. Vacuum-Rabi oscillations and collective effects are therefore largely suppressed. Moreover, the laser beams exciting the atoms are running perpendicular to the cavity axis, so that the photon statistics of the light emitted from the cavity is not the result of a driving field interfering with the atomic emission, as for an axially excited cavity [22–24]. It follows that all requirements to observe the transition between antibunching and bunching for independently fluorescing atoms with one-and-the-same experimental setup are fulfilled. In fact, we find that, with an increasing number of atoms, a strong bunching peak (demonstrating the wave character of the light) develops inside the antibunching minimum at $\tau = 0$ (characterizing the particle nature of the light).

Figure 1 illustrates the setup. A cloud of ^{85}Rb atoms released from a magneto-optical trap (MOT) falls through a 1 mm long optical cavity of finesse $F = 60\,000$. The average number of atoms simultaneously interacting with the cavity, $\bar{N}$, is freely adjustable by the loading time of the trap between $\bar{N} = 0$ and $\bar{N} \approx 140$. In the cavity, the atoms are exposed to two laser beams. The pump laser continu-

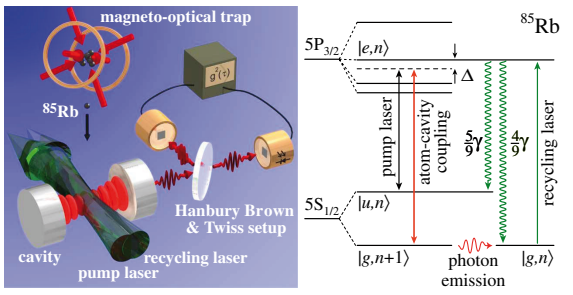

FIG. 1 (color online). Scheme of the experiment. Left: The setup shows that atoms are released from a magneto-optical trap and fall through a cavity 20 cm below with a velocity of 2 m/s. Each atom interacts with the TEM_{00} mode of the cavity for about 20 μs and is exposed to pump and recycling laser beams. The light emitted from the cavity is registered by a pair of photodiodes. Right: Relevant levels and transitions in ^{85}Rb. The atomic states $|u\rangle$, $|e\rangle$, and $|g\rangle$ are involved in the Raman process, and the states $|n\rangle$ and $|n+1\rangle$ denote the cavity's photon number.

PRL **94,** 053604 (2005) PHYSICAL REVIEW LETTERS week ending 11 FEBRUARY 2005

ously drives the transition between the state $|u\rangle \equiv |5S_{1/2}(F=3)\rangle$ and the excited state $|e\rangle \equiv |5P_{3/2}(F=3)\rangle$ with Rabi frequency Ω_P, while the cavity couples $|e\rangle$ to the other hyperfine ground state, $|g\rangle \equiv |5S_{1/2}(F=2)\rangle$. Both fields are detuned by an amount Δ from the respective atomic transition so that they resonantly drive a Raman transition between $|u\rangle$ and $|g\rangle$ which also changes the intracavity photon number by one. At the same time, a recycling laser of Rabi frequency Ω_R resonantly drives the transition from $|g\rangle$ to $|e\rangle$, from where the atoms decay back to state $|u\rangle$. This closes the excitation loop and enables each atom to emit several photons on its way through the cavity. Because of the continuous driving, the Raman transitions are stochastic in contrast to the adiabatically driven Raman transition process reported in [15,25–27]. The dynamics of the system is determined by $(g_{\max}, \kappa, \gamma, \Omega_P, \Omega_R, \Delta) = 2\pi \times (2.5, 1.25, 3.0, 7.6, 3.3, -20)$ MHz, where $g_{\max}$ is the cavity-induced coupling between states $|e,0\rangle$ and $|g,1\rangle$ for an atom optimally coupled to the cavity, and κ and γ are the field and polarization decay rates of the cavity and the atom, respectively. The maximum recycling rate is achieved when the transition between $|g\rangle$ and $|e\rangle$ is strongly saturated. In this case, both levels are equally populated leading to a recycling rate of $R_{\max} = \frac{5}{9}\gamma = 2\pi \times 1.7$ MHz, where $\frac{5}{9}$ is the average branching ratio for a decay from $|e\rangle$ to $|u\rangle$. Therefore the recycling is always slower than the decay of the cavity excitation, 2κ. For the above value of Ω_R, the recycling is about 4 times slower than the cavity decay, so that the cavity returns to the vacuum state before the next photon is placed into its mode from the same atom. Therefore nonclassical antibunching can be observed. The maximum effective Rabi frequency of the Raman process, $\Omega_{\text{eff}} = g_{\max}\Omega_P/\Delta = 2\pi \times 0.95$ MHz, is also smaller than the cavity decay rate. Therefore the system is overdamped and shows no Rabi oscillations; i.e., both the reabsorption of emitted photons and the cavity-mediated interaction between different atoms are negligible. The cavity decay is mainly caused by the 100 ppm transmittance of one of the mirrors. Photons leave the cavity through this output coupler with a probability of 90%, and are detected by two photodiodes with 50% quantum efficiency that are placed at the output ports of a beam splitter. They form a Hanbury Brown and Twiss setup to measure the $g^{(2)}(\tau)$ intensity correlation function of the light. To avoid a limitation to a waiting-time distribution between successive photons, all photodetection times are registered and taken into account in the evaluation.

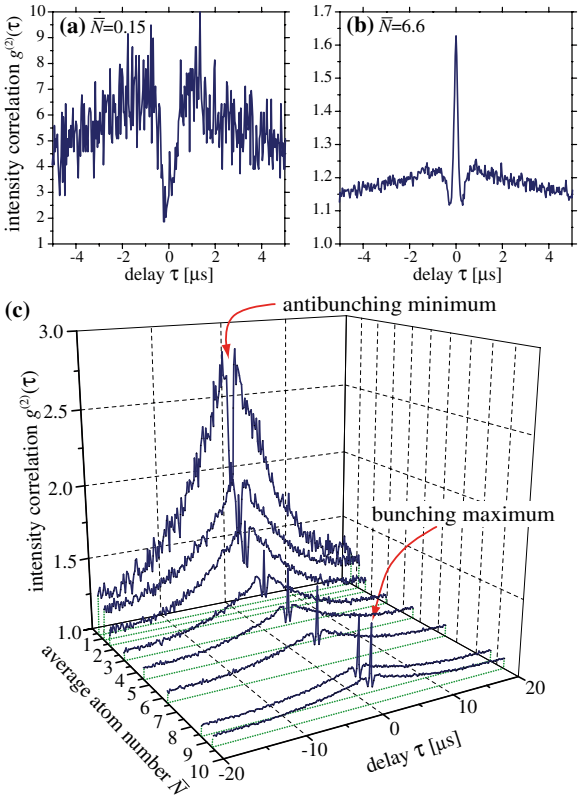

FIG. 2 (color online). Intensity correlation, $g^{(2)}(\tau)$, as a function of the detection time delay, τ, for different values of the average atom number, $\bar{N}$. A transition from antibunching to bunching is observed for $\bar{N} \approx 1$. To adjust $\bar{N}$, we load the trap between 20 ms and 2.5 s. For each trace, we load and release atoms from the MOT 500 times and register photons during $\delta t =$ 8 ms while the atom cloud traverses the cavity.

Figure 2 shows $g^{(2)}(\tau)$ for different settings of the atom flux. For an average atom number below one, $\bar{N} = 0.15$, it shows nonclassical antibunching, i.e., a local minimum at $\tau = 0$ in Fig. 2(a). Note that sub-Poissonian light with $g^{(2)}(0) < 1$ is not observed because the Poissonian statistics of the atomic cloud is mapped to the photon statistics. When the atom flux is increased to $\bar{N} > 1$, a transition to bunching, i.e., a local maximum at $\tau = 0$, is observed; see Figs. 2(b) and 2(c).

This transition from nonclassical light for $\bar{N} < 1$ to classical light for $\bar{N} > 1$ can be explained with a model [4] that describes an ensemble of independent emitters where the electric field of all atoms,

$$E(t) = \sum_{i=1}^{N(t)} E_i(t), \tag{1}$$

is the sum of the fields radiated by the individual atoms, $E_i(t)$. Obviously, the individual fields interfere with the fields radiated by the other atoms. For independent emitters, correlations between the fields of different atoms can be neglected. Following [4] and provided the atom distribution is Poissonian with an average atom number $\bar{N}$ [28], the intensity correlation function reads

$$g^{(2)}(\tau) = 1 + |f(\tau)g_A^{(1)}(\tau)|^2 + f(\tau)g_A^{(2)}(\tau)/\bar{N}. \tag{2}$$

PRL **94,** 053604 (2005) PHYSICAL REVIEW LETTERS week ending 11 FEBRUARY 2005

It consists of three different contributions: (i) The constant term 1 stems from photons that are independently emitted by different atoms, i.e., it reflects the atom statistics which is directly mapped to the light. (ii) The bunching term, $|f(\tau)g_A^{(1)}(\tau)|^2$, with $g_A^{(1)}(\tau)$ the autocorrelation function of the electric field emitted by one atom and $f(\tau)$ given below [29], results from the beating of the light emitted by different atoms. Constructive or destructive interference leads to a fluctuating intensity [1]. If a photon is detected, constructive interference is likely and the probability for a second photodetection is increased. The opposite holds for destructive interference. The interference and the correlated behavior vanish if the two photodetections are separated by more than the coherence time. Therefore the bunching contribution decreases with the square of $g_A^{(1)}(\tau)$, whose $\frac{1}{e}$ decay defines the coherence time, τ_c. Note that this contribution does not depend on the number of atoms and therefore persists for very high atom flux. (iii) The antibunching term, $f(\tau)g_A^{(2)}(\tau)/\bar{N}$, with $g_A^{(2)}(\tau)$ the single-atom intensity correlation function, is attributed to the photons emitted from an individual atom. After a photon emission, the atom must be recycled to state $|u\rangle$ before it can emit another photon. This leads to antibunching. Because of the statistical nature of the recycling, photons are uncorrelated for large $|\tau|$, and $g_A^{(2)}(\tau \to \pm\infty)$ reaches 1. However, only photons emitted from one-and-the-same atom during its limited interaction time with the cavity contribute. The envelope function, $f(\tau)$, with $f(\tau \to \pm\infty) = 0$, takes this into account. Note that the antibunching term scales with the inverse average atom number, $1/\bar{N}$, and therefore vanishes for large $\bar{N}$.

The three contributions explain the observed transition from antibunching to bunching shown in Fig. 2(c): the antibunching contribution for $\bar{N} < 1$ vanishes with increasing atom number while the bunching contribution does not change. For a detailed comparison of this model with the experiment, we write the correlation function as $g^{(2)}(\tau, 1/\bar{N}) = A(\tau) + B(\tau)/\bar{N}$, with

$$|g_A^{(1)}(\tau)|^2 = \frac{A(\tau) - 1}{f^2(\tau)}, \qquad g_A^{(2)}(\tau) = \frac{B(\tau)}{f(\tau)}. \tag{3}$$

For every value of τ, we can now obtain $A(\tau)$ and $B(\tau)$ from a linear fit to the experimentally observed $g^{(2)}(\tau, 1/\bar{N})$ as a function of $1/\bar{N}$ [30]. For the two examples $\tau = 0$ and $\tau = 1\ \mu$s, Fig. 3(a) shows that this procedure is indeed justified, as the experimental data show a linear dependence on $1/\bar{N}$. The same result holds for other values of τ. The offset $A(\tau) = \lim_{\bar{N}\to\infty} g^{(2)}(\tau, 1/\bar{N})$ represents the two $\bar{N}$-independent contributions, (i) and (ii), from above, whereas the slope $B(\tau) = d(g^{(2)}(\tau, 1/\bar{N}))/d(1/\bar{N})$ determines the size of the antibunching contribution. A decomposition of $g^{(2)}(\tau, 1/\bar{N})$ into these contributions is shown in Fig. 3(b). $A(\tau)$ consists of the constant term 1 plus the bunching peak, whereas $B(\tau)$ shows an antibunching dip and decays with an envelope function $f(\tau)$ that is imposed by the atom transit.

Figure 4 shows the single-atom correlation functions deduced from $A(\tau)$ and $B(\tau)$ using the relations (3). These functions reveal the relevant experimental time scales. The minimum delay between two successive photons from one-and-the-same atom corresponds to the $1/e$ half width of the antibunching dip, $\tau_A = 430 \pm 10$ ns. This is much larger than the photon lifetime in the cavity, $\kappa^{-1}/2 = 64$ ns, so that successive photons from a single atom hardly overlap. From the decay of the field correlation function, $|g_A^{(1)}(\tau)|^2$, we calculate a coherence time of the emitted light of $\tau_c = 170 \pm 2$ ns (half $1/e^2$ width), larger than the decay time of the cavity field, $\kappa^{-1} = 128$ ns. This seemingly unexpected result is not surprising as the coherence properties are controlled by the photon-

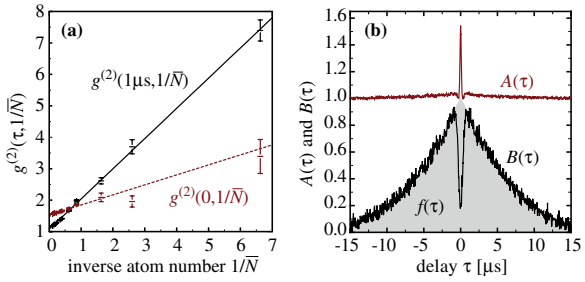

FIG. 3 (color online). (a) Decomposition of $g^{(2)}(\tau, 1/\bar{N})$: Linear-regression fit as a function of $1/\bar{N}$ for $\tau = 0$ and $\tau = 1\ \mu$s. For each τ, the offset $A(\tau)$ and the slope $B(\tau)$ are obtained from such fits. (b) Bunching and antibunching contributions, $A(\tau)$ and $B(\tau)$, respectively. Modeling $B(\tau)$ for $|\tau| > 1.0\ \mu$s yields the empirical envelope, $f(\tau) = \exp(-|\tau/6.5\ \mu\text{s}|^{1.22})$ (shaded).

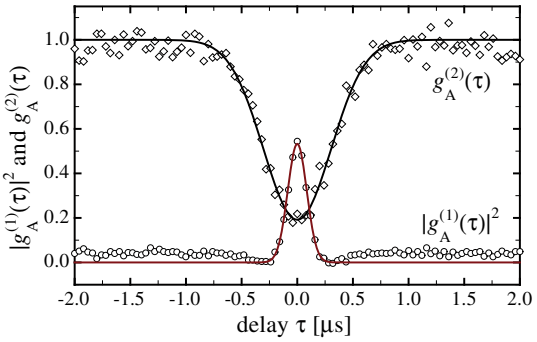

FIG. 4 (color online). Single-atom correlations, $|g_A^{(1)}(\tau)|^2$ and $g_A^{(2)}(\tau)$, deduced from $A(\tau)$, $B(\tau)$, and $f(\tau)$ using Eq. (3). The two contributions weighted according to Eq. (2) determine the observed photon statistics, $g^{(2)}(\tau)$, as shown in Fig. 2. Because of a small cross talk between $g_A^{(2)}(\tau)$ and $|g_A^{(1)}(\tau)|^2$, the latter stays larger than zero for values of τ smaller than the atom-cavity interaction time.

generating Raman process, which takes longer than the cavity decay time [31]. We also note that the peak amplitude of the field correlation function, $|g_A^{(1)}(0)|^2 = 0.53 \pm 0.01$, is very close to the expectation value for independently emitting atoms, which is $|g_A^{(1)}(0)|^2 = 0.5$ for unpolarized light [32].

The only small discrepancy from our expectations is that $g_A^{(2)}(\tau = 0)$ does not vanish completely as one would expect for the resonance fluorescence of single atoms [33]. Instead, we obtain $g_A^{(2)}(0) = 0.19 \pm 0.02$. This slight departure from perfect antibunching indicates that some atoms emit a second photon before the first photon has left the cavity. To assure that such collective effects do not dominate, we have verified that the photon number increases linearly with the average atom number in our parameter regime. Only with at least 100 atoms and drive Rabi frequencies raised by a factor of 3, does the average photon number show a slightly nonlinear increase with $\bar{N}$; i.e., a moderate amplification is found. However, no kink in the photon number is observed that would signal a lasing threshold. In fact, laser operation relies on a recycling rate much larger than the cavity decay rate, so that the photons remain long enough in the cavity to stimulate further emissions.

In conclusion, we have observed the transition from antibunching to bunching in the fluorescence light emitted from a high-finesse cavity with an increasing average number of atoms in the cavity. The cavity decay determines the fastest time scale, so that the atoms act as independent emitters. The agreement of our data with the predicted scaling behavior of the photon statistics is excellent, so that the single-atom correlation functions for antibunching and bunching, $g_A^{(2)}(\tau)$ and $g_A^{(1)}(\tau)$, respectively, can be extracted. It would be interesting to apply a similar analysis to a lasing atom-cavity system [7], where cooperative effects are expected to dominate the photon statistics.

We thank B. W. Shore for stimulating discussions. This work was supported by the Deutsche Forschungsgemeinschaft (SPP 1078 and SFB 631) and the European Union [IST (QGATES) and IHP (CONQUEST) programs].

*Present address: ICFO–Institut de Ciències Fotòniques, Jordi Girona 29, Nexus II, 08034 Barcelona, Spain.

[1] M. O. Scully and M. Zubairy, *Quantum Optics* (Cambridge University Press, Cambridge, U.K., 1997).
[2] L. Mandel and E. Wolf, *Optical Coherence and Quantum Optics* (Cambridge University Press, Cambridge, U.K., 1995), Chap. 14.7.3.
[3] H. J. Kimble, M. Dagenais, and L. Mandel, Phys. Rev. Lett. **39**, 691 (1977).
[4] H. J. Carmichael, P. Drummond, P. Meystre, and D. F. Walls, J. Phys. A **11**, L121 (1978).
[5] F. Diedrich and H. Walther, Phys. Rev. Lett. **58**, 203 (1987).
[6] V. Gomer, F. Strauch, B. Ueberholz, S. Knappe, and D. Meschede, Phys. Rev. A **58**, R1657 (1998).
[7] J. McKeever, A. Boca, A. D. Boozer, J. R. Buck, and H. J. Kimble, Nature (London) **425**, 268 (2003).
[8] F. De Martini, G. Di Giuseppe, and M. Marrocco, Phys. Rev. Lett. **76**, 900 (1996).
[9] P. Michler *et al.*, Nature (London) **406**, 968 (2000).
[10] C. Kurtsiefer, S. Mayer, P. Zarda, and H. Weinfurter, Phys. Rev. Lett. **85**, 290 (2000).
[11] A. Beveratos, R. Brouri, T. Gacoin, J.-P. Poizat, and P. Grangier, Phys. Rev. A **64**, 061802 (2001).
[12] B. Lounis and W. E. Moerner, Nature (London) **407**, 491 (2000).
[13] P. Michler *et al.*, Science **290**, 2282 (2000).
[14] C. Santori, D. Fattal, J. Vučković, G. S. Solomon, and Y. Yamamoto, Nature (London) **419**, 594 (2002).
[15] A. Kuhn, M. Hennrich, and G. Rempe, Phys. Rev. Lett. **89**, 067901 (2002).
[16] A. Beveratos *et al.*, Phys. Rev. Lett. **89**, 187901 (2002).
[17] J. McKeever *et al.*, Science **303**, 1992 (2004).
[18] M. Keller, B. Lange, K. Hayasaka, W. Lange, and H. Walther, Nature (London) **431**, 1075 (2004).
[19] R. Hanbury Brown and R. Q. Twiss, Nature (London) **178**, 1046 (1956).
[20] C. Jurczak *et al.*, Phys. Rev. Lett. **77**, 1727 (1996).
[21] S. Bali, D. Hoffmann, J. Simán, and T. Walker, Phys. Rev. A **53**, 3469 (1996).
[22] J. Carmichael, R. J. Brecha, and P. R. Rice, Opt. Commun. **82**, 73 (1991).
[23] G. Rempe, R. J. Thompson, R. J. Brecha, W. D. Lee, and H. J. Kimble, Phys. Rev. Lett. **67**, 1727 (1991).
[24] S. L. Mielke, G. T. Foster, and L. A. Orozco, Phys. Rev. Lett. **80**, 3948 (1998).
[25] M. Hennrich, T. Legero, A. Kuhn, and G. Rempe, Phys. Rev. Lett. **85**, 4872 (2000).
[26] A. Kuhn and G. Rempe, in *Experimental Quantum Computation and Information*, edited by F. De Martini and C. Monroe (IOS Press, Amsterdam, 2002), Vol. 148, pp. 37–66.
[27] M. Hennrich, A. Kuhn, and G. Rempe, J. Mod. Opt. **50**, 935 (2003).
[28] For $\tau \geq 1\ \mu$s, we assume that $g_A^{(2)} = 1$ and $g_A^{(1)} \approx 0$. With $f(1\ \mu\text{s}) \approx 1$, this leads to $g^{(2)}(1\ \mu\text{s}, \bar{N} = 1) \approx 2$. This value is used to calibrate the atom flux leading to $\bar{N} = 1$. Relative to this calibration, $\bar{N}$ is then adjusted by laser-induced fluorescence.
[29] H. J. Kimble, M. Dagenais, and L. Mandel, Phys. Rev. A **18**, 201 (1978).
[30] Variations of the atom density lead to a small modulation of $g^{(2)}(\tau)$ in the millisecond regime. This contribution was subtracted to prevent a falsification of the fit.
[31] T. Legero, T. Wilk, M. Hennrich, G. Rempe, and A. Kuhn, Phys. Rev. Lett. **93**, 070503 (2004).
[32] With $|g_A^{(1)}(0)|^2 = 1$ for each polarization mode, and uncorrelated orthogonal modes (in both ways), the average of these four contributions leads to $|g_A^{(1)}(0)|^2 = 0.5$.
[33] H. J. Carmichael and D. F. Walls, J. Phys. B **9**, 1199 (1976).

RAPID COMMUNICATIONS

PHYSICAL REVIEW A **72**, 010704(R) (2005)

Feshbach spectroscopy of a shape resonance

Thomas Volz,[1] Stephan Dürr,[1] Niels Syassen,[1] Gerhard Rempe,[1] Eric van Kempen,[2] and Servaas Kokkelmans[2]
[1]*Max-Planck-Institut für Quantenoptik, Hans-Kopfermann-Straße 1, 85748 Garching, Germany*
[2]*Eindhoven University of Technology, P.O. Box 513, 5600MB Eindhoven, The Netherlands*
(Received 4 October 2004; published 29 July 2005)

We present a spectroscopy technique for studying cold-collision properties. The technique is based on the association and dissociation of ultracold molecules using a magnetically tunable Feshbach resonance. The energy and lifetime of a shape resonance are determined from a measurement of the dissociation rate. Additional spectroscopic information is obtained from the observation of a spatial interference pattern between an outgoing *s* wave and *d* wave. The experimental data agree well with the results from a model, in which the dissociation process is connected to a scattering gedanken experiment, which is analyzed using a coupled-channel calculation.

DOI: 10.1103/PhysRevA.72.010704 PACS number(s): 34.50.Gb, 03.75.Nt

The field of ultracold molecules has seen tremendous progress in the past two years. The key technique that triggered this development is the association of ultracold molecules from ultracold atoms using a Feshbach resonance [1–9]. A Feshbach resonance is caused by the resonant coupling of a colliding atom pair to a molecular bound state. The system can be tuned into resonance by applying a magnetic field. To produce stable molecules, the magnetic field is slowly ramped across the Feshbach resonance to lower fields. For detection, the molecules are dissociated by ramping the magnetic field back to higher values above the Feshbach resonance. In this field range, the energy of the molecular state lies in the continuum of unbound atom-pair states. The coupling between the discrete molecular state and the continuum of atomic states leads to an exponential decay of the molecules into unbound atom pairs. These atoms are then imaged with standard techniques. Beyond this molecule detection scheme, the dissociation has other interesting applications: For example, the width of the Feshbach resonance can be extracted from the energy released in the dissociation process [7,10].

In this Communication, we use the dissociation process as a spectroscopic tool for studying cold-collision properties. Specifically, we investigate a *d*-wave shape resonance in ^{87}Rb. The shape-resonance state is a quasibound state which is localized behind the centrifugal barrier. The energy of this state lies in the continuum of unbound atom-pair states. In our experiment, the shape resonance is probed by tuning the energy of the Feshbach molecules with the magnetic field. If the energy of the molecules matches the energy of the shape resonance, then population is transferred from the molecular state to the shape-resonance state. From there, the population decays rapidly into unbound atom pairs by tunneling through the centrifugal barrier. The molecules can therefore dissociate in two ways, either directly into the continuum or indirectly by passing through the shape-resonance state. The indirect processes turn out to be much faster than the direct ones, so that the molecule dissociation rate is drastically enhanced. However, if the energies of the molecules and the shape resonance do not match, then indirect processes will be suppressed. The magnetic-field dependence of the dissociation rate thus reveals the energy and lifetime of the shape resonance. This information can be used as spectroscopic input to constrain theoretical models for the cold-collision properties. Little is gained in the case of ^{87}Rb, where the collisional properties are rather well known, and where the shape resonance has been observed in previous experiments [11–13]. However, our method is interesting for systems, where the collisional properties are unknown, such as heteronuclear mixtures or nonalkali species. Here, theoretical models starting from *ab initio* calculations presently do not have enough experimental input to obtain realistic predictions for the cold-collision properties.

The experimental setup was described in detail elsewhere [3,10,14]. In brief, a Bose-Einstein condensate (BEC) of ^{87}Rb atoms in the hyperfine state $|f,m_f\rangle=|1,1\rangle$ is prepared in an optical dipole trap. The magnetic field is held slightly above the Feshbach resonance, which is located at $B_{res}\sim 632$ G [14]. It is caused by a *d*-wave molecular state and has a width of 1.3 mG [10]. The BEC is released from the trap and 1 ms later molecules are created by slowly ramping the magnetic field downward across the Feshbach resonance. Remaining atoms are spatially separated from the molecules using a Stern-Gerlach field. Next, the molecules are dissociated back into unbound atom pairs by jumping the magnetic field to a value $B>B_{res}$ and holding it there for a variable time t_{hold} [15]. During t_{hold}, population in the molecular state decays exponentially with a rate $\Gamma(B)$, which depends on the value of B during t_{hold}. After t_{hold}, the magnetic field is switched off rapidly, which stops the dissociation process. After 0.85 ms time of flight (counting from the dissociation), an absorption image is taken. Molecules that did not decay during t_{hold} are invisible in the image, because only unbound atoms resonantly absorb light from the detection laser beam.

The dissociation rate $\Gamma(B)$ is extracted from a series of images for fixed B and variable t_{hold}. The number of dissociated atoms is determined from each image and then fit to an exponential as a function of t_{hold}. This yields the dissociation rate shown in Fig. 1. The enhanced dissociation rate near 1.3 G due to the shape resonance is clearly visible.

In a simple analytic model, the dissociation can be described as a two-step process. In the first step, the interaction

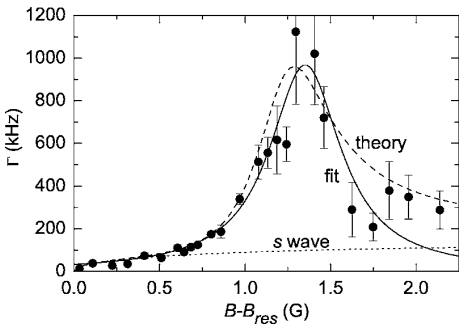

FIG. 1. Molecule dissociation rate Γ as a function of magnetic field B with respect to the position of the Feshbach resonance B_{res}. The experimental data for the total rate (circles) clearly show the effect of the shape resonance near 1.3 G. The solid line is a Lorentzian fit to the data. The dashed (dotted) line shows the prediction for the total (s-wave) dissociation rate from a coupled-channel calculation. The s-wave dissociation is not affected by the shape resonance.

Hamiltonian H transfers population from the molecular state $|\psi_{mol}\rangle$ to the shape-resonance state $|\psi_{shape}\rangle$. This is described by a generalized Rabi frequency $\Omega=(2/\hbar)|\langle\psi_{shape}|H|\psi_{mol}\rangle|$. In the second step, the population tunnels with a rate Γ_{shape} from $|\psi_{shape}\rangle$ into the continuum of unbound atom-pair states. One can show that for $\Omega \ll \Gamma_{shape}$ the molecular state decays exponentially with a rate [16]

$$\Gamma(B) = \frac{\Omega^2}{\Gamma_{shape}}\left[1+\left(2\frac{E_{shape}-E_{mol}(B)}{\hbar\Gamma_{shape}}\right)^2\right]^{-1}, \qquad (1)$$

where E_{shape} and E_{mol} are the energies of the shape-resonance state and the molecular state, respectively. E_{mol} depends on B, while Γ_{shape}, E_{shape}, and Ω in this simple model do not. For the small magnetic-field range considered here, a linear approximation holds

$$E_{mol}(B) = (B - B_{res})\Delta\mu, \qquad (2)$$

where B_{res} is the position of the Feshbach resonance and $\Delta\mu$ is the difference in the magnetic moments between a molecule and an unbound atom pair. $\Delta\mu$ is determined experimentally from the time-of-flight images shown in Fig. 2. The radial cloud size in the images yields the kinetic energy E in the relative motion of the dissociated atom pairs. Due to energy conservation in the dissociation process, $E=E_{mol}(B)$. We thus obtain $\Delta\mu=k_B\times 230(18)$ μK/G. Alternatively, $\Delta\mu$ can be determined with a Stern-Gerlach method [3].

$\Gamma(B)$ in Eq. (1) is a Lorentzian, which is fit to the data as shown in Fig. 1. Using the above value for $\Delta\mu$, the best-fit parameters are $E_{shape}=k_B\times 312(25)$ μK, $\Gamma_{shape}=15(3)$ MHz, and $\Omega=2\pi\times 0.61(7)$ MHz. We thus extract the energy and lifetime of the shape resonance as well as the Rabi frequency without making any reference to the coupled-channel calculation further below.

Figure 2 shows time-of-flight images of the atoms after dissociation. They exhibit spatial interference patterns created by different outgoing partial waves. Only two partial waves contribute to these interference patterns, namely those

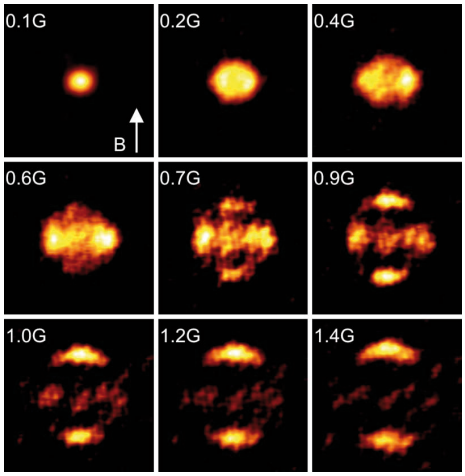

FIG. 2. (Color online) Time-of-flight images of unbound atoms obtained in the molecule dissociation. The images were taken at different values of $B-B_{res}$. The magnetic field is vertical in the images. The interference between the s and d partial waves undergoes a change in relative phase and amplitude. At 0.1 G, the dissociation is mostly s wave, producing a circle. For higher magnetic fields, both partial waves are populated. From 0.2 to 0.6 G, the interference suppresses atom emission *along* B, whereas the opposite relative phase in the interference between 1.0 and 1.4 G suppresses emission *perpendicular* to B. At 0.7 and 0.9 G, the relative phase is such that neither component is strongly suppressed. The typical radius reached by the atoms during the constant time of flight increases for increasing B, thus indicating an increase of the kinetic energy released in the dissociation.

with quantum numbers $(l,m_l)=(0,0)$ and (2, 0) for the rotation of the atoms around each other [17]. The indirect dissociation processes (where population passes through the shape-resonance state) create outgoing d waves, because the shape-resonance state is a d-wave state and the tunneling out of this state does not affect the angular momentum. In contrast, the direct dissociation processes are independent of the shape resonance and preferentially populate the s-wave state, because all other partial waves are suppressed for low energy by the centrifugal barrier. Note that interference between different partial waves of cold atoms has previously been observed in *scattering* experiments [12,13,18]. Previous molecule *dissociation* experiments, however, observed only outgoing s waves.

The interference pattern is described by the following wave function:

$$\psi_{decay}(\vec{r}) = g(r,t)[\sqrt{\beta_0}Y_{00} - e^{i\delta_{rel}}\sqrt{\beta_2}Y_{20}(\vartheta)], \qquad (3)$$

where $Y_{lm}(\vartheta,\varphi)$ is a spherical harmonic, the real numbers β_l and δ_{rel} characterize the amplitudes of the partial waves and their relative phase, and $g(r,t)$ is a radial wave function. $g(r,t)$ is normalized such that $\beta_0+\beta_2=1$, which implies that β_l is the branching ratio for decay into the lth partial wave.

The branching ratio β_2 and the relative phase δ_{rel} are extracted from the images with the same method as used in Ref. [13]. In brief, computed tomography is used to recon-

struct the three-dimensional (3D) density distribution from the two-dimensional (2D) images. The 3D density is sorted into 20 bins to obtain the probability $W(\vartheta)$ for finding an atom at angle ϑ. A fit of the angular part of the modulus squared of Eq. (3) to $W(\vartheta)$ yields the fit parameters β_2 and δ_{rel}. These parameters are shown in Fig. 3. The branching ratio clearly shows the enhanced decay into the d wave due to the shape resonance. For β_2 close to 0 or 1, the fit cannot reliably determine the relative phase.

In order to analyze the dissociation more rigorously, we performed a coupled-channel calculation for a scattering gedanken experiment that is closely related to our dissociation experiment. We briefly summarize the theory here. For more details, see Ref. [19]. In the gedanken experiment, we consider a colliding atom pair with kinetic energy E in the relative motion in the presence of a magnetic field B near the 632-G Feshbach resonance. S-matrix elements $S_{ll'}$ are calculated in the E-B-plane for l and l' equal to 0 or 2 (both with $m_l=0$). According to the theory of multichannel scattering resonances, these S-matrix elements are expected to follow an analytic expression of the form [20,21]

$$S_{ll'}(E,B) = \left(\delta_{ll'} - \frac{i\hbar\Gamma_{ll'}(E)}{E - E_{mol}(B) + \frac{i}{2}\hbar\Gamma(E)} \right) e^{i[\delta_l^{bg}(E)+\delta_{l'}^{bg}(E)]}. \tag{4}$$

Here, $\delta_{ll'}$ is the Kronecker symbol, $\Gamma(E)$ is the total decay rate of the molecular state, $E_{mol}(B)$ is given by Eq. (2), and the significance of the partial-decay-rate parameters $\Gamma_{ll'}(E)$ will be discussed below. Finally, $\delta_l^{bg}(E)$ is the background scattering phase for the lth partial wave, where background means for magnetic fields far away from the Feshbach resonance [22].

For any given E, we fit Eq. (4) for variable B to the S-matrix elements obtained from our coupled-channel calculation. The fits match the S matrix extremely well. The open-channel physics, including the shape resonance, is independent of B and is therefore included in the energy-dependent fit parameters $\delta_l^{bg}(E)$ and $\Gamma_{ll'}(E)$. Furthermore, the combination of the fits yields $\Delta\mu = k_B \times 224\ \mu\mathrm{K/G}$.

We will now discuss the connection between our dissociation experiment and the fit parameters $\delta_l^{bg}(E)$ and $\Gamma_{ll'}(E)$. As mentioned earlier, the kinetic energy E of the atom pairs after dissociation is $E=E_{mol}(B)$. Therefore the energy-dependent fit parameters for the gedanken experiment become magnetic-field-dependent parameters in the dissociation experiment $\delta_l^{bg}(B)$ and $\Gamma_{ll'}(B)$.

The link between the scattering gedanken experiment and the dissociation experiment can be established from evaluating the different terms in the asymptotic form of the regular scattering wave function

$$\psi^{(+)}(\vec{r}) \overset{r\to\infty}{\sim} (-1)^{l'} \frac{e^{-ikr}}{r} Y_{l'0}(\vartheta) - \frac{e^{ikr}}{r} \sum_l (S_{ll'}^{bg} + S_{ll'}^{res}) Y_{l0}(\vartheta), \tag{5}$$

where we assume in the gedanken experiment that only one partial wave l' is initially populated. Here, k is related to the energy by $E=\hbar^2k^2/(2m_{red})$ with the reduced mass m_{red}, and we split the S matrix into a background part and a resonant part $S_{ll'}=S_{ll'}^{bg}+S_{ll'}^{res}$ with $S_{ll'}^{bg}=e^{2i\delta_l^{bg}(E)}\delta_{ll'}$.

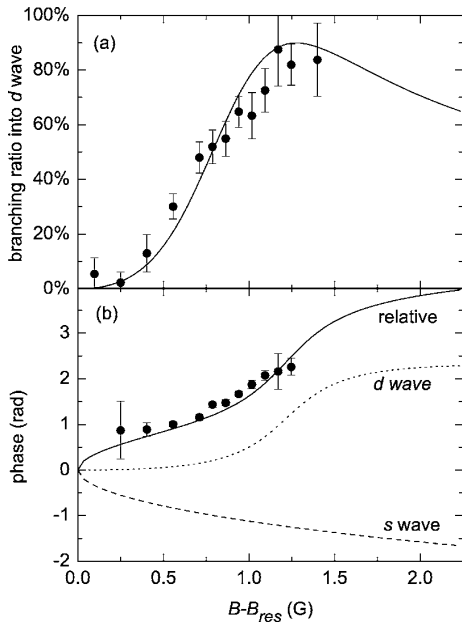

FIG. 3. Parameters extracted from the spatial interference patterns. (a) Branching ratio for decay into the d wave. Again, the d-wave shape resonance is clearly visible. (b) Partial-wave phases and relative phase. The solid, dashed, and dotted lines show the theoretical prediction for the relative phase $\delta_{rel}=\delta_2^{bg}-\delta_0^{bg}$, the s-wave phase δ_0^{bg}, and the d-wave phase δ_2^{bg}, respectively. Experimental data (circles) agree well with the theory (solid line) in (a) and (b).

The scattering wave function consists of three parts: an incoming wave, an outgoing background wave, and an outgoing resonant wave. The resonant part is due to particles that make the transition to the molecular state and subsequently decay back into the open channel. The Stern-Gerlach separation removes all incoming flux and along with it the background scattered wave. Hence, these two terms need to be removed from the scattering state in order to describe the decay wave function

$$\psi_{decay}(\vec{r}) \overset{r\to\infty}{\sim} -\frac{e^{ikr}}{r} \sum_l S_{ll'}^{res} Y_{l0}(\vartheta). \tag{6}$$

Using the above equations, this can be rewritten to yield Eq. (3), where the relative phase of the decaying partial waves is $\delta_{rel}=\delta_2^{bg}-\delta_0^{bg}$ and the branching ratio for decay into the lth partial wave is given by $\beta_l(B)=\Gamma_{ll}(B)/\Gamma(B)$. This means that $\Gamma_{ll}(B)$ represents the partial decay rate into the lth partial wave. The theory for the decay rate, branching ratio, and the phases is shown as lines in Figs. 1 and 3. The good agreement between theory and experiment without any free fit parameters supports the theory developed here.

Finally, we extract the parameters of the simple model from the full theory. The d-wave decay rate $\Gamma_{22}=\Gamma-\Gamma_{00}$ is the difference between the total and the s-wave decay rate, both shown in Fig. 1. The maximum of Γ_{22} is located at 1.28 G corresponding to $E_{shape}=k_B\times 287\ \mu$K. The value and the curvature of $\Gamma_{22}(B)$ at the maximum correspond to $\Gamma_{shape}=17$ MHz and $\Omega=2\pi\times 0.61$ MHz. These numbers agree well with the values obtained by fitting the simple model Eq. (1) to the experimental data.

In conclusion, we showed that dissociation of ultracold molecules can be used to measure the energy and lifetime of a shape resonance. Additional information was obtained from the analysis of the spatial interference patterns. This is enough information to constrain theoretical models so much that the basic scattering properties of the system can be determined. We developed a model for the dissociation, which agrees well with the experimental results.

We acknowledge fruitful discussions with Harald Friedrich and Boudewijn Verhaar. This work was supported by the European-Union Network "Cold Quantum Gases." S.K. acknowledges support from the Netherlands Organization for Scientific Research (NWO). E.K. acknowledges support from the Stichting FOM, financially supported by NWO.

[1] C. A. Regal, C. Ticknor, J. L. Bohn, and D. S. Jin, Nature (London) **424**, 47 (2003).
[2] J. Herbig, T. Kraemer, M. Mark, T. Weber, C. Chin, H.-C. Nägerl, and R. Grimm, Science **301**, 1510 (2003).
[3] S. Dürr, T. Volz, A. Marte, and G. Rempe, Phys. Rev. Lett. **92**, 020406 (2004).
[4] K. E. Strecker, G. B. Partridge, and R. G. Hulet, Phys. Rev. Lett. **91**, 080406 (2003).
[5] J. Cubizolles, T. Bourdel, S. J. J. M. F. Kokkelmans, G. V. Shlyapnikov, and C. Salomon, Phys. Rev. Lett. **91**, 240401 (2003).
[6] S. Jochim, M. Bartenstein, A. Altmeyer, G. Hendl, C. Chin, J. Hecker Denschlag, and R. Grimm, Phys. Rev. Lett. **91**, 240402 (2003).
[7] T. Mukaiyama, J. R. Abo-Shaeer, K. Xu, J. K. Chin, and W. Ketterle, Phys. Rev. Lett. **92**, 180402 (2004).
[8] M. W. Zwierlein, C. A. Stan, C. H. Schunck, S. M. F. Raupach, A. J. Kerman, and W. Ketterle, Phys. Rev. Lett. **92**, 120403 (2004).
[9] S. T. Thompson, E. Hodby, and C. E. Wieman, Phys. Rev. Lett. **94**, 020401 (2005).
[10] S. Dürr, T. Volz, and G. Rempe, Phys. Rev. A **70**, 031601(R) (2004).
[11] H. M. J. M. Boesten, C. C. Tsai, J. R. Gardner, D. J. Heinzen, and B. J. Verhaar, Phys. Rev. A **55**, 636 (1997).
[12] N. R. Thomas, N. Kjærgaard, P. S. Julienne, and A. C. Wilson, Phys. Rev. Lett. **93**, 173201 (2004).
[13] Ch. Buggle, J. Léonard, W. von Klitzing, and J. T. M. Walraven, Phys. Rev. Lett. **93**, 173202 (2004).
[14] A. Marte, T. Volz, J. Schuster, S. Dürr, G. Rempe, E. G. M. van Kempen, and B. J. Verhaar, Phys. Rev. Lett. **89**, 283202 (2002).
[15] The jump in the magnetic field is in fact a fast magnetic-field ramp ($dB/dt\approx 1$ G/μs), during which hardly any dissociation occurs. At the end of the ramp, the magnetic field settles in at about 1 μs.
[16] C. Cohen-Tannoudji, J. Dupont-Roc, and G. Grynberg, *Atom-Photon Interactions* (Wiley, New York, 1992), pp. 49–59.
[17] The interaction Hamiltonian conserves parity so that Δl is even. Moreover, due to rotational symmetry around the z axis (along B), $m_l+m_{f1}+m_{f2}$ is conserved, where the magnetic quantum numbers of the atoms are m_{f1},m_{f2}. These are +1 each, before and after the interaction. Hence m_l is identical before and after the interaction. Since the incoming wave in the association is an s wave, all outgoing partial waves must have $m_l=0$ and even l. Finally, partial waves with $l>2$ are negligible in the low-energy range considered here.
[18] R. Legere and K. Gibble, Phys. Rev. Lett. **81**, 5780 (1998).
[19] S. Dürr *et al.*, e-print cond-mat/0507580.
[20] J. R. Taylor, *Scattering Theory* (Wiley, New York, 1972).
[21] H. Feshbach, *Theoretical Nuclear Physics* (Wiley, New York, 1992).
[22] For the S matrix to be unitary and symmetric, the parameters $\Gamma_{ll'}(E)$ must all be real and fulfill $\Gamma_{00}+\Gamma_{22}=\Gamma$ and $\Gamma_{20}=\Gamma_{02}=\pm\sqrt{\Gamma_{00}\Gamma_{22}}$. From the coupled-channel calculation we find that in our case $\Gamma_{02}=-\sqrt{\Gamma_{00}\Gamma_{22}}$.

PRL 95, 173002 (2005) PHYSICAL REVIEW LETTERS week ending 21 OCTOBER 2005

Continuous Loading of an Electrostatic Trap for Polar Molecules

T. Rieger, T. Junglen, S. A. Rangwala,* P. W. H. Pinkse, and G. Rempe

Max-Planck-Institut für Quantenoptik, Hans-Kopfermann-Strasse 1, D-85748 Garching, Germany

(Received 5 May 2005; published 18 October 2005)

A continuously operated electrostatic trap for polar molecules is demonstrated. The trap has a volume of ≈ 0.6 cm^3 and holds molecules with a positive Stark shift. With deuterated ammonia from a quadrupole velocity filter, a trap density of $\approx 10^8$ cm^{-3} is achieved with an average lifetime of 130 ms and a motional temperature of ≈ 300 mK. The trap offers good starting conditions for high-precision measurements, and can be used as a first stage in cooling schemes for molecules and as a ''reaction vessel'' in cold chemistry.

DOI: 10.1103/PhysRevLett.95.173002 PACS numbers: 33.80.Ps, 33.55.Be, 39.10.+j

The production and storage of cold polar molecules is of considerable interest to physicists and chemists. Once sufficiently cold and dense samples are available, the anisotropic and long-range dipole-dipole interaction can lead to new phases of matter [1–3]. The interaction can even be tuned by external fields allowing one to link polar molecules [4]. Other applications include the study of ultracold chemical reactions [5]. Different methods have been developed to produce and trap cold polar molecules [6]. Here, trapping is defined as the ability to store the particles much longer than the time it would take them to leave the trap volume in the absence of the trapping potential. So far, magnetic trapping was demonstrated for molecules cooled by a buffer gas [7] or synthesized from alkali atoms by photoassociation [8]. In other experiments decelerated samples of cold molecules were trapped in static [9,10] or oscillating [11] electric fields. A basic feature of all these methods is their pulsed operation, where the trap is switched on after the sample has been produced, or the sample is produced in the trap center. From that point onward, the sample decays, e.g., by collisions with background gas, and has to be regenerated. Accumulative methods have been proposed, but remain challenging [12]. Such continuously operated traps would be advantageous not only for high-precision measurements where long observation times with samples under constant conditions are required, but also for determining cold collision rates of reacting molecular species.

In this Letter we report on a novel electrostatic trap for polar molecules, which is continuously loaded from an electrostatic quadrupole guide [13]. Equilibration of the filling and loss rates results in a steady state population of trapped molecules. The trap works along electrostatic principles already proposed some time ago [14]. It confines low-field-seeking molecules in a region with low electric field strength, surrounded by a region with a high electric field. The trap is experimentally demonstrated with deuterated ammonia (ND_3), but can be used for all molecules exhibiting significant Stark effect. As shown in Fig. 1(a), the trap consists of five ring-shaped electrodes and two spherical electrodes at both ends. Neighboring electrodes carry high voltages of different polarity giving rise to an inhomogeneous electric field, illustrated in Fig. 1(b), which is large near the electrodes and small in the center of the trap. The central ring electrode is intersected 2 times and local thickening of the neighboring electrodes towards the gaps makes it possible to adapt two quadrupole segments, one for filling and one for extraction of the trapped gas. The inner radii of the five ring electrodes are 2.0, 4.3, 4.8, 4.3, and 2.0 mm and the two end electrodes have a diameter of 2 mm. The electrodes are separated by a 1 mm gap and the enclosed volume amounts to ≈ 0.6 cm^3. With the present setup, a voltage difference of 10 kV between neighboring trap electrodes can be reached. This results in

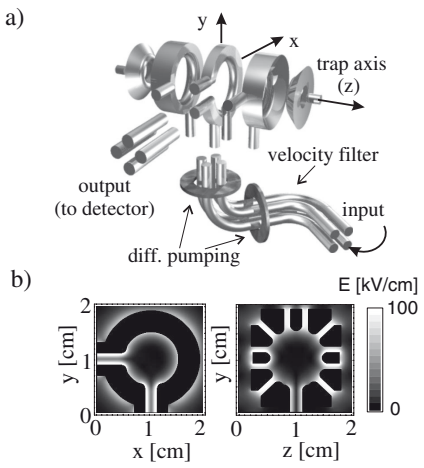

FIG. 1. (a) Exploded view of the trap with input and output quadrupoles. The quadrupole guide filters slow molecules from the cooled effusive source and guides them into the trap. Here the slowest molecules reside till they find their way out through one of the two quadrupole guides. The trapped gas is analyzed with a mass spectrometer positioned behind the output quadrupole. (b) Electric field distribution in the xy plane for electrode voltages of ± 5 kV (left) together with the field distribution in the yz plane containing the input quadrupolar guide (right).

PRL 95, 173002 (2005) PHYSICAL REVIEW LETTERS week ending 21 OCTOBER 2005

a minimum electric field of ≈40 kV/cm which the molecules need to overcome in order to escape the trap in regions away from the small entrance and exit holes. At these electric fields, only guided molecules with velocities below ≈30 m/s can be kept within the trap where the maximum capture velocity depends on the Stark shift of the individual molecule.

Once inside the trap, those molecules which overcome the Stark potential barrier of the trap are either lost by hitting the electrodes or they escape the trap and are pumped away. The remaining molecules undergo multiple reflections off the trap potential, randomizing their motion, and escape via the entrance or exit hole. As the trap surface is large compared to the exit channel area given by the two quadrupolar openings, the probability of finding these holes is small and can even be made arbitrarily small by making the trap volume and/or the electric field larger. Even though the trap allows continuous filling, continuous accumulation is not possible in this conservative potential and the trap density equilibrates when the filling rate equals the leakout rate.

In our experiment, the trap is filled with ND_3 from a quadrupole velocity filter as detailed in Ref. [15]. In brief, molecules from a thermal reservoir are loaded into a quadrupolar electric field guide via an appropriate nozzle assembly. The quadrupole potential provides filtering of the slowest molecules in the transverse direction whereas the longitudinal filtering is achieved by the centripetal action in a bent part of the guide between the nozzle and the trap. With this technique, a continuously guided flux of the order of 10^{10} s^{-1} can be achieved for quadrupole voltages of ±5 kV, which results in a maximum electric field of ≈90 kV/cm. The guided flux consists of a mixture of states with different Stark shifts with the larger Stark shifted states preferentially guided. The longitudinal velocity distribution can be described by a one-dimensional thermal distribution with a most probable velocity of ≈40 m/s. Because of the two-dimensional confinement at finite field strengths, the transversal velocity distribution is expected to be much narrower. In passing we note that the Stark state distribution in the guide and the trap is the same despite additional filtering in the trap as discussed above.

As the average electric field inside the quadrupole is higher than inside the trap, the molecules are accelerated when entering the trap. It follows that the lowest-velocity molecules are absent in the trap. The properties of the trapped sample are revealed by the molecules which leave the trap through the 17 cm long output quadrupole. Here, the molecules are guided through a differential pumping aperture into a separate vacuum chamber where they are detected by a mass spectrometer (MS). Both the input and output quadrupole guides are separated by a 0.5 mm gap from a short piece of a quadrupole guide formed from the trap electrodes. This separation allows independent switching of the quadrupole segments and the trap. The background pressure in the trap chamber is of the order of 10^{-10} mbar and even lower in the detection chamber.

In a first trapping experiment, voltages of ±4.5 kV were applied to the trap and the output electrodes while the input quadrupole was switched from 0 kV to ±4.5 kV and back every 2 s. The effusive source temperature was set to a constant value of 160 K. Figure 2(a) shows a raw trapping signal obtained after averaging over 4000 cycles. When the input quadrupole is switched on at $t = 0$, slow molecules are guided and the trap is filled resulting in an increasing signal at the output quadrupole guide. After the input quadrupole is switched off at $t = 1$ s, a signal decay is observed which allows us to estimate the lifetime of the molecules in the trap. However, we found that the rising and the falling slopes show significant rates of change in signal even 500 ms after switching on or off the input quadrupole. After 500 ms of filling or emptying of the trap, steady state conditions are expected to prevail. Hence, a change of the output flux cannot be caused by the molecules of interest. On the rising slope, the excess signal is likely to be caused by a local pressure increase near the detector after switching on the guiding process. These molecules must be pumped away after switching off

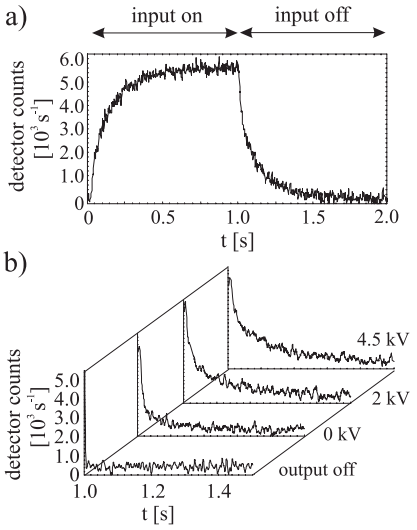

FIG. 2. (a) The raw detector signal at the output quadrupole as a function of time when the voltage at the input quadrupole is switched. The electrodes carry voltages of ±4.5 kV. (b) Deconvoluted detector signals as a function of time for different trapping-field configurations. A rapid decay is observed when the output is switched off at $t = 1$ s. The trap dynamics is revealed by rapidly switching the voltage on one small ring electrode from 4.5 kV to 0, 2, and 4.5 kV after finishing the filling process in order to create an artificial hole in the trap. When the particular electrode is set to 0 kV a clear signal loss can be observed, whereas the slow decay caused by trapped molecules becomes dominant for higher voltages when the trap hole is closed. The signal trace obtained with output off serves as a reference.

PRL 95, 173002 (2005) PHYSICAL REVIEW LETTERS week ending 21 OCTOBER 2005

the input guide, an effect which leads to a time-dependent signal at the falling slope. These spurious signals can be measured by switching on and off the output quadrupole while the trap is continuously filled: As soon as the output guide is switched off, a rapid decay of the MS signal to the background level is expected, only limited by the time the molecules that already left the guide need to fly to the detector, typically less than 1.0 ms. Indeed, a fast decay can be observed but it is accompanied by a slow decay with a $1/e$ time of $\approx$150 ms. Assuming that the guided flux into the detector is a sharp step function $\Theta(t)$, the measured signal $S_\Theta(t)$ is used to determine the deconvolution kernel, $F(K) = F(S_\Theta(t))/F(\Theta(t))$, where F denotes the Fourier transform. For determining the lifetime of the molecules in the trap, the measured decay signal, $S_D(t)$, is deconvoluted by the transformation $S(t) = F^{-1}[F(S_D(t))/F(K)]$, where F^{-1} denotes the inverse Fourier transform. After deconvolution the slow rise and fall of the signal 500 ms after switching on and off the input guide vanishes.

Having described the deconvolution process, we now discuss the trap measurements in which the input quadrupole is periodically switched. In order to demonstrate that the decay rate originates from the trap dynamics, an artificial hole was created in the trap by rapidly lowering the voltage on one small ring electrode to a constant value when the input quadrupole, and accordingly the filling process, is switched off. Figure 2(b) shows the decay signals after deconvolution for reduced voltages on the particular ring electrodse of 0, 2, and 4.5 kV. In the decay measurement where the voltage has been switched to 0 kV, a fast decay can be observed followed by a small and slow decay contribution. The fast decay is caused by the losses due to the weaker field near the particular ring electrode. The molecules causing the slow decay are either too slow to overcome even the weak field potential barrier or they do not encounter the weak field on their way inside the trap. Note that the start of the decay is delayed by the time the molecules need to pass through the output quadrupole. When the voltage on the ring electrode is raised to 2.0 kV, the loss rate decreases leading to a reduction of the fast decay contribution, whereas the slow decay caused by molecules which are trapped longer is more pronounced. For the remaining curve the voltage on the electrode is set to 4.5 kV and here the slow decay is dominant.

Note that the initial fast decay can always be observed. Simulations show that this decay is caused by a class of molecular trajectories which approximately are confined in the plane defined by the middle ring electrode. As both exit channels lie in this plane a fast escape is very probable. For those molecules whose trajectories fill the whole trap volume the escape probability is reduced leading to a longer trapping time. As the lifetime of the molecules in the trap depends on how fast they find an exit, the lifetime is velocity dependent. Therefore, the decay cannot be described by an exponential function and, hence, not by a $(1/e)$ lifetime. An alternative measure for the trap lifetime is the time after which half the molecules have left the trap. From the data for $\pm$4.5 kV a lifetime of 130 $\pm$ 10 ms can be derived.

The lifetime is mainly limited by the exit channels, whereas collisions with the background gas do not contribute significantly. As the field vanishes only at some regions in the center of the trap, Majorana transitions to nontrapping Stark levels are not very likely. With the angle distribution of the guided molecules behind the output quadrupole and the sensitivity of the MS the total flux emerging from the trap can be determined. From the measured angle distribution it has been determined that only 15% of the guided flux reaches the detector. As the detector sensitivity is of the order of 10^{-4} counts/molecule the guided flux from the trap with all electrodes set to $\pm$4.5 kV amounts to 3×10^8 s^{-1}. Similar trapping results were obtained with formaldehyde (CH_2O) and methylchloride (CH_3Cl) which also show a linear Stark effect.

In the following the temperature of the trapped ND_3 sample is determined by a measurement of the molecules' velocity distribution. Therefore, a time-of-flight measurement is performed where the trap is continuously filled and only the output quadrupole is switched on and off at rate 1 Hz. All electrodes were set to voltages of $\pm$4.5 kV. As soon as the output quadrupole is switched on, molecules from the trap are guided to the detector where their arrival time is recorded. After more than 50 000 cycles a clear time-of-flight signal has developed. From the delay and the rising slope the longitudinal velocity distribution can be derived by differentiation. For a single molecular state, the velocity distribution should show a relatively sharp velocity cutoff because the guide and the trap filter on kinetic energy. But given a mixture of states with different Stark shifts, the cutoff is smeared out so that the velocity distribution can be described by a one-dimensional thermal distribution. As the time-of-flight signal is affected by the above-mentioned spurious signal, the measured signal was deconvoluted according to the method described above. Figure 3 shows the velocity distribution obtained from the deconvoluted data. It can be described by a characteristic velocity $\alpha = 16 \pm 1$ m/s with $\alpha = \sqrt{2k_BT/m}$, where k_B is the Boltzmann constant, T the temperature, and m the molecular mass. The characteristic velocity α is equivalent to the most probable speed of a thermal gas in a three-dimensional volume element. This velocity corresponds to a motional temperature of 300 mK. Note that the lowest-velocity molecules may be partially depleted by collisions in the nozzle where the densities are relatively high. Note also that the molecular velocities in the output quadrupole are slightly smaller than inside the trap because the molecules are decelerated when entering the higher quadrupole field. However, as there are only conservative potentials involved, the temperature of the sample does not change. The experimental data are in good agreement with the simulation. As expected, the temperature of 300 mK is smaller than the trap depth of 800 mK derived from the average Stark potential.

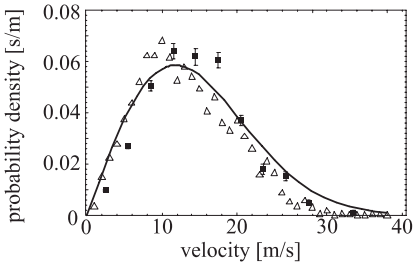

FIG. 3. Velocity distribution of trapped ND_3 molecules derived from data obtained with electrode voltages of ± 4.5 kV (squares). The line is a fit to the measured data of the functional form $(2v/\alpha^2)\exp[-v^2/\alpha^2]$, with the characteristic longitudinal velocity $\alpha = 16.6 \pm 1$ m/s. The triangles denote simulation results.

The transverse velocity distribution of the trapped molecules can be estimated by recording the decrease of the flux of guided molecules in the output quadrupole when the electric field in the latter is reduced. During the measurements, the voltages on the input quadrupole and the trap were set to ± 4.5 kV and the input was modulated. In each measurement the electric field in the output quadrupole was set to a different but constant value. It was observed that more than 90% of the flux from the trap can be guided even if the output quadrupole voltage is reduced down to ± 750 V so that most of the molecules can be two-dimensionally trapped in an electric field of only 15 kV/cm. Below this voltage, the guided flux decreases and at voltages of ± 160 V (≈ 3 kV/cm), for example, the initial flux has reduced by a factor of 2. The measured decrease of the signal amplitude as a function of the output quadrupole voltage is in good agreement with the simulation of the experiment. This justifies the assumption that the simulated transverse velocity distribution with its characteristic velocity of $\alpha_{\mathrm{sim}} = 14$ m/s describes the experiment well. It follows that the characteristic velocity α of the longitudinal distribution is roughly equal to the characteristic velocity α_{sim} determined for the transversal velocity distribution, which is in contrast to the situation in the input quadrupole guide. There, the longitudinal velocities can be much higher as longitudinal filtering is less restrictive than transverse filtering. The trap randomizes the input velocity which leads to an equilibration of the transverse and longitudinal velocity distributions, as is also obtained in the simulation. With the knowledge of the average speed $\bar{v} = 2\alpha/\sqrt{\pi}$ and the total molecular flux Φ out of the trap, one can estimate the number density n in the trap by $\Phi = \frac{1}{4} n \bar{v} A$ where A is the effective area of each of the two exit channels. From simulations we know that the molecular density distribution inside the guide with voltages of ± 4.5 kV has a half-width of ≈ 400 μm. Taking this as the radius of a circular area A and assuming an average velocity $\bar{v}$ of 18 m/s, the number density inside the trap is of the order of 10^8 cm^{-3}.

To summarize, a continuously loaded, large-volume electrostatic trap for polar molecules has been demonstrated experimentally. Our results show that a sample of ND_3 molecules at a density of 10^8 cm^{-3} can be trapped with a lifetime of 130 ± 10 ms. The trap is filled from a quadrupole guide, but it is also conceivable to produce molecules inside the trap, for example, by reactive collisions [16] or crossed molecular beams [17]. These molecules could be cooled by a buffer gas [7] or light scattering [18]. A simple modification of the present trap with three guides coupled to it could lead to the intriguing possibility of an electrostatic "reaction vessel." Two of the guides could be used to load different species of molecules into the trap and the third guide could be used to extract and detect the reaction products. If the trap volume is large, the lifetime and the number of molecules is expected to increase so that reactions inside the trap become possible even at the present densities. Provided electrostatic or mechanical valves can be developed, one can even envision a small cold chemical factory made out of a network of interconnected reaction vessels with new possibilities in controlling chemical reactions.

*Present address: Raman Research Institute, C. V. Raman Avenue, Sadashivanagar, Bangalore 560080, India.

[1] L. Santos *et al.*, Phys. Rev. Lett. **85**, 1791 (2000).
[2] M. A. Baranov *et al.*, Phys. Rev. A **66**, 013606 (2002).
[3] K. Góral, L. Santos, and M. Lewenstein, Phys. Rev. Lett. **88**, 170406 (2002).
[4] A. V. Avdeenkov and J. L. Bohn, Phys. Rev. Lett. **90**, 043006 (2003).
[5] N. Balakrishnan and A. Dalgarno, Chem. Phys. Lett. **341**, 652 (2001).
[6] See, e.g., the Special issue on Ultracold Polar Molecules, edited by J. Doyle, B. Friedrich, R. V. Krems, and F. Masnou-Seeuws [Eur. Phys. J. D **31**, 149 (2004)].
[7] J. D. Weinstein *et al.*, Nature (London) **395**, 148 (1998).
[8] D. Wang *et al.*, Phys. Rev. Lett. **93**, 243005 (2004).
[9] H. L. Bethlem *et al.*, Nature (London) **406**, 491 (2000).
[10] H. L. Bethlem *et al.*, Phys. Rev. A **65**, 053416 (2002).
[11] J. van Veldhoven, H. L. Bethlem, and G. Meijer, Phys. Rev. Lett. **94**, 083001 (2005).
[12] S. Y. T. van de Meerakker *et al.*, Phys. Rev. A **64**, 041401 (2001).
[13] S. A. Rangwala *et al.*, Phys. Rev. A **67**, 043406 (2003).
[14] W. H. Wing, Phys. Rev. Lett. **45**, 631 (1980).
[15] T. Junglen *et al.*, Eur. Phys. J. D **31**, 365 (2004).
[16] H.-J. Loesch (private communication).
[17] M. S. Elioff, J. J. Valentini, and D. W. Chandler, Science **302**, 1940 (2003).
[18] V. Vuletić and S. Chu, Phys. Rev. Lett. **84**, 3787 (2000).

PRL 95, 173602 (2005) PHYSICAL REVIEW LETTERS week ending 21 OCTOBER 2005

Submicron Positioning of Single Atoms in a Microcavity

Stefan Nußmann, Markus Hijlkema, Bernhard Weber, Felix Rohde,* Gerhard Rempe, and Axel Kuhn

Max-Planck-Institut für Quantenoptik, Hans-Kopfermann-Str. 1, D-85748 Garching, Germany

(Received 10 June 2005; published 19 October 2005)

The coupling of individual atoms to a high-finesse optical cavity is precisely controlled and adjusted using a standing-wave dipole-force trap, a challenge for strong atom-cavity coupling. Ultracold Rubidium atoms are first loaded into potential minima of the dipole trap in the center of the cavity. Then we use the trap as a conveyor belt that we set into motion perpendicular to the cavity axis. This allows us to repetitively move atoms out of and back into the cavity mode with a repositioning precision of 135 nm. This makes it possible to either selectively address one atom of a string of atoms by the cavity, or to simultaneously couple two precisely separated atoms to a higher mode of the cavity.

DOI: 10.1103/PhysRevLett.95.173602 PACS numbers: 42.50.Pq, 32.80.Pj, 32.80.Qk, 42.50.Vk

Worldwide, intense research is being devoted to control the position of an array of single atoms. To meet this objective, several techniques are currently being explored with optical [1–5], magnetic [6–8], or electric [9–11] fields. However, none of the experiments performed so far has achieved positioning in combination with strong coupling to a high-finesse optical cavity. Either the atom could not be stopped inside the cavity, or strong coupling was not achieved, or trapping of a discrete number of atoms was probabilistic and cavity addressing was not possible [12–15]. The problems encountered when combining single-atom control with strong coupling are twofold: On the one hand, the small optical cavity required to achieve strong coupling adds a significant complexity, making the experiment challenging. On the other hand, atomic motion in the regime of strong coupling is dramatically different from free-space motion [13,16]. We now report on an experiment where the novel phenomena that a strongly coupled atom experiences inside a cavity are exploited to achieve the above-mentioned objective. Our experiment is the first in which a distinct number of atoms is repeatedly transported in and out of and brought to a halt inside an environment where atoms and cavity can no longer be considered separate entities by virtue of their strong coupling.

The apparatus and the atom transport into the cavity are illustrated in Fig. 1. A cold cloud of ^{85}Rb atoms is prepared in a magneto-optical trap (MOT). From there, these atoms are transferred over a distance of 14 mm into a cavity by means of a horizontally running-wave dipole-force trap, which is formed by a single beam of an Yb:YAG laser (5 W, 1030 nm). This beam is red detuned from the relevant transitions and therefore attracts the atoms towards regions of highest intensity, i.e., towards its focus, which is located between the MOT and the cavity. The atoms oscillate with a period of 200 ms in this trap (waist 40 μm, Rayleigh length 4.8 mm, depth 240 μK), with one turning point at the position of the MOT, and the other in the cavity. This oscillation is stopped as soon as the atoms arrive in the cavity, by switching from the guiding dipole trap to a standing-wave dipole trap (2 W each direction, waist 16 μm in the center of the cavity). The atoms are trapped in the antinodes of the standing wave that act as potential wells of 2.5 mK depth, with a well-to-well distance of 515 nm. Nanopositioning of the atoms relative to the cavity mode is accomplished by tilting a glass plate in the path of the retro-reflected beam. This changes the optical path length and therefore also the position of the antinodes. The glass plate is mounted on a galvo scanner that provides a measured repeatability of the interference pattern of ± 15 nm. This setup has been calibrated interferometrically. Since the trapped atoms follow this motion, they can be shifted to any position along the axis of the dipole-trap beams, as if they were sitting on a conveyor belt [1]. The positioning range is ± 250 μm, limited by the

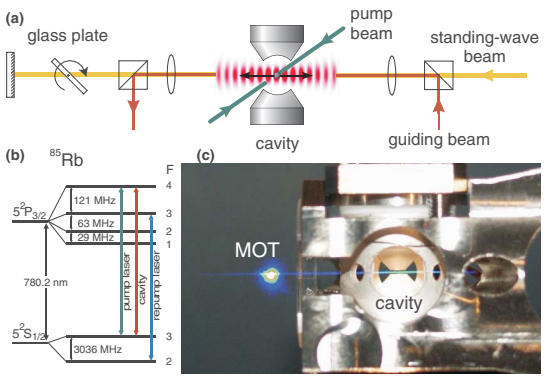

FIG. 1 (color online). Experimental setup: (a) Sketch of the dipole-trap arrangement that is used to guide atoms into the cavity. A standing-wave dipole-force trap allows us to freely adjust the position of an atom within the cavity mode by tilting a thick glass plate in front of the retro-reflecting mirror. Atoms that are trapped in the antinodes are displaced accordingly. (b) Level-scheme of ^{85}Rb including the relevant transitions. (c) Side view of the cavity (cone-shaped mirrors), superimposed with absorption images of an atom cloud in the MOT and in the transport trap illustrating the path of the atoms.

PRL 95, 173602 (2005) PHYSICAL REVIEW LETTERS week ending 21 OCTOBER 2005

present thickness of the glass plate (3 mm). This allows a precise tuning of the coupling to the cavity.

The cavity is 490 μm long so that transverse optical access is granted, and the mirror reflectivity is unbalanced, so that photons generated inside are emitted mainly through one of its mirrors. With the two mirrors (of 5 cm radius of curvature) having transmission coefficients of $T_0 = 2$ ppm and $T_1 = 95$ ppm, strong coupling to the TEM_{00}-mode is reached with $(g_0, \kappa, \gamma) = 2\pi \times (5, 5, 3)$ MHz, and to the TEM_{01}-mode with $(g_0, \kappa, \gamma) = 2\pi \times (4.3, 2.5, 3)$ MHz. Here, g_0 is the atom-cavity coupling constant in a cavity antinode averaged over all the relevant atomic transitions, κ the cavity-field decay rate, and γ the polarization decay rate of the atom. Note that we have deliberately chosen a regime (with $g_0 \simeq \kappa$) where the photons are emitted from the cavity before they are reabsorbed due to vacuum-Rabi oscillations. Moreover, the cavity length (and therefore its mode volume) was chosen to be large enough to accommodate transverse pumping and trapping beams, resulting in $g_0 \simeq \gamma$. We emphasize that single-photon generation schemes, like those demonstrated in Munich [17,18], work very well in such cavities. Moreover, single atoms inside the cavity lead to a $\sim$10-fold reduction of the intensity of a resonant light beam transmitted through the cavity, demonstrating strong coupling for the known γ and κ.

To continuously monitor the atom-cavity coupling, we tune the cavity resonance close to the $5^2S_{1/2}(F = 3)$ to $5^2P_{3/2}(F' = 4)$ transition and continuously excite the atom with a pair of counter-propagating lin $\perp$ lin polarized laser beams. These pump-laser beams run perpendicular to the cavity axis and have the same frequency as the cavity, so that resonant Raman scattering of photons into the cavity mode takes place, although the atoms are Stark-shifted out of resonance by the dipole trap. In particular, the transition

$$|F = 3, n = 0\rangle \overset{\text{laser}}{\rightarrow} |F = 4, n = 0\rangle \overset{\text{cavity}}{\rightarrow} |F = 3, n = 1\rangle$$

keeps the atomic state unchanged, but changes the intracavity photon number n by one, so that the initial and final states differ, which is characteristic for Raman transitions. With the TEM_{00} mode of the cavity driving one branch of this transition, the photon-scattering rate from the atom-cavity system is in first approximation given by the enhanced spontaneous emission rate, $T_1(c/(2L))(g_{\mathrm{eff}}/\kappa)^2 = 640\ \mathrm{ms}^{-1}$, with $g_{\mathrm{eff}} = \Omega_l g_0/2\Delta_{ls}$ the effective atom-cavity coupling strength, where $\Omega_l = 2\pi \times 30$ MHz is the Rabi frequency of the driving laser and $\Delta_{ls} = 2\pi \times 100$ MHz is the dynamic Stark shift from the trapping laser. We estimated that in our experiment about 20 photons/ms are actually detected (due to detector efficiency, transmission loss, etc.).

As we show elsewhere [19], this cavity and pump beam configuration provides efficient cooling of the atoms in the center of the cavity mode. Here, this is used to efficiently load atoms into the cavity. When the dilute cloud of atoms guided from the MOT arrives inside the cavity, the standing-wave potential is turned on. This gives rise to a random distribution of atoms among various potential wells in the vicinity of the cavity mode. Some atoms are hot enough to ripple along the dipole-trap axis like a marble across a washboard, in a random walk. As soon as such an atom enters the cavity mode, it scatters photons into the cavity and is subject to light forces which cool the atom into a potential well. The atom then remains trapped inside the cavity, where it continues to scatter photons. One after another, atoms are loaded into (or lost from) the cavity. This manifests itself in a stepwise increase (or decrease) of the photon-scattering rate into the cavity, which is therefore an unambiguous measure for the number of trapped atoms.

To avoid a fluctuating atom number, we apply a filtering procedure. Some 10 ms after the atoms have been loaded into the standing-wave trap, and when on average one atom has been caught, we interrupt the trap for 10 ms and turn it back on adiabatically. During this interruption, only very cold and well-localized atoms remain captured in the weak dipole trap formed by the red-detuned light field that is used to stabilize the cavity length, while all other atoms are lost. The light of this additional trap is detuned from the Rubidium resonance by eight free spectral ranges of the cavity, i.e., by 5 nm. Moreover, its 44 μK-deep potential wells show a good overlap with the resonant cavity mode in the center of the cavity. This helps to localize cold atoms in the antinodes of the cavity mode. Our preparation sequence usually results in 0, 1, or 2 atoms coupled to the cavity. From the photon-scattering rate, we can determine the exact atom number within a few milliseconds. Note that the weak intracavity trap together with the standing-wave trap forms a 2D optical lattice. The atoms finally trapped therein have a lifetime of 3 s (without the pump laser) and of more than 15 s if continuously excited by the pump laser.

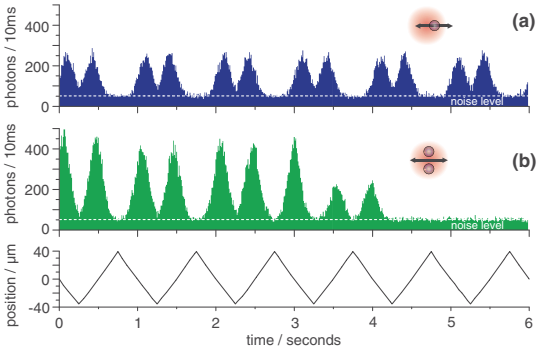

FIG. 2 (color online). Controlled coupling of individual atoms to the cavity: Count rate of the photons emerging from the TEM_{00}-mode of the cavity while (a) a single atom is swept to and fro once a second over a distance of 75 μm. (b) Same situation but starting with two atoms that are lost one after the other.

PRL 95, 173602 (2005) PHYSICAL REVIEW LETTERS week ending 21 OCTOBER 2005

This is an unprecedented trapping time for a neutral atom under permanent observation inside a cavity.

As we load a well-known number of atoms into the cavity, we can also adjust the atom-cavity coupling to any value by tilting the glass plate. This is demonstrated in Fig. 2(a), where a single atom is swept to and fro once a second over a distance of 75 μm through the cavity mode. Figure 2(b) shows the same situation, but starting with two atoms (twice the peak-count rate) that are lost one after another. This shows that we are able to manipulate a single atom for many seconds.

To demonstrate and analyze the repositioning capabilities of our setup, we have performed a series of experiments where we modulate the atomic position with several frequencies and amplitudes, and finally bring the atom back to its initial position. Figure 3(a) depicts the situation where the atom is initially sitting on the cavity axis. We sinusoidally sweep the atom to and fro for a period of 0.5 s with a sweep amplitude of 25 μm. We stop this modulation at the initial position, and, as expected, the final photon-count rate equals the initial count rate, i.e., the atom has been brought back to its starting point. We have now measured such traces for 71 individual atoms, and we swept each atom 19 times through the cavity. For each atom transit, we have determined the standing-wave position that leads to the optimum photon-count rate. Figure 3(b) shows the mean deviation (root-mean-square or RMS value) of these positions relative to the position found in the first or second transit (for both sweep directions separately). Because of the noise of our measurement technique, the positions initially scatter over a range of ± 2 μm (in the third and fourth transit). However, the more important feature is the gradual increase of the mean deviation from transit to transit by an amount of 135 nm. This slow increase is a measure of how well we can reproduce the atomic position. We therefore conclude that the atom is brought back to its starting point within ± 135 nm from one transit to the next. A possible reason for this uncertainty is the small but nonvanishing probability for the atom to hop to another potential well in the outer turning points.

A similar method was applied to study the initial spatial distribution of the atoms, i.e., their average coupling to the cavity after the filter phase. A statistical investigation of 68 traces yields a width of the lateral distribution of ± 7.7 μm along the axis of the dipole trap. This is small compared to the cavity waist, $w_0 = 29.5$ μm. We therefore conclude that the average atom-cavity coupling is reduced by at most 7% due to an initial lateral displacement. This indicates that during the filter phase the atoms had a temperature of only 5 μK in the 44 μK-deep cavity trap.

Finally, we have investigated the effect of the atom transport on the lifetime with and without pump light. Figure 4 shows the probability for an atom to survive 0.5 s of sweeping its position to and fro as a function of the sweep frequency for different sweep amplitudes. Without pump light, the survival probability is high for slow sweeps. However, a fast loss of atoms occurs as soon as the product of sweep frequency and amplitude exceeds 500 μm Hz. With the sweep being sinusoidal, this indicates strong losses if the maximum sweep velocity of the trap exceeds $2\pi \times 500$ μm $/(\lambda_{YAG}/2) = 6100$ potential wells per second. We know that residual back reflections of the laser cause an intensity modulation at the same frequency. Therefore we attribute the sharp onset of losses to parametric heating, which is affecting the atom once the lowest trap frequency is met.

If we carry out the same experiment with pump light, we see two effects: First, the survival probability is very high

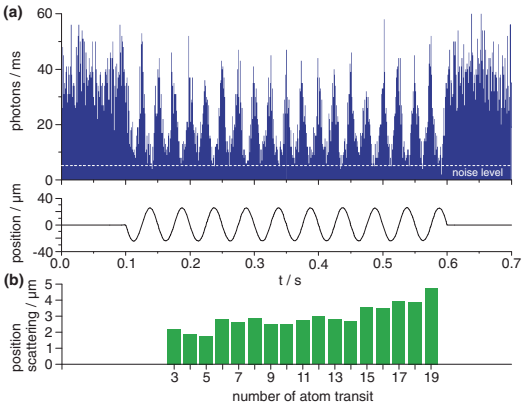

FIG. 3 (color online). Repeatability of atomic positions: Count rate of photons emerging from the cavity while the atomic position is modulated with 20 Hz over a distance of ± 25 μm, and finally brought back to its initial value (a). The 5 kHz noise level is due to photons of the cavity dipole trap at 785 nm still passing the 780 nm filters used for shielding the photon counters. (b) RMS deviation from the initial atomic position, averaged over 71 single-atom traces. The ± 2 μm initial spread stems from noise, but the gradual 135 nm increase from transit to transit reflects the repeatability of the positioning scheme.

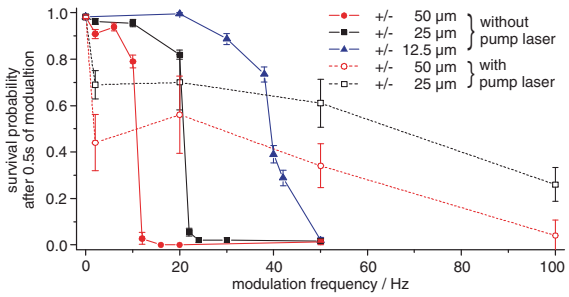

FIG. 4 (color online). Survival probability for moving atoms after 0.5 s of sweeping to and fro, plotted as a function of the sweep frequency for three different sweep amplitudes. Measurements were performed with (open symbols) and without (closed symbols) pump laser. The different behavior reflects the influence of the pump laser on the dynamics of the atom.

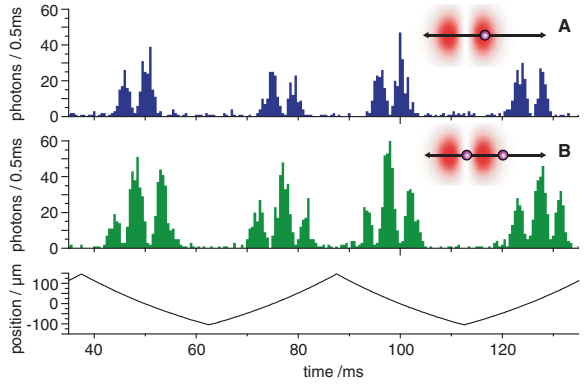

FIG. 5 (color online). Controlled coupling to the TEM_{01}-mode. (a) Photon-count rate from the TEM_{01}-mode while a single atom is swept to and fro with a frequency of 20 Hz over a distance of 250 μm. (b) Same situation, but starting with two atoms whose distance corresponds exactly to the distance between the two maxima of the TEM_{01}-mode. The probability for this arrangement is strongly enhanced due to our loading scheme.

without modulation (0 Hz), but it is reduced significantly even for low sweep frequencies, i.e., atoms are heated and can get lost once they leave the center of the mode. Second, for high sweep frequencies, the strong cooling force in the center of the cavity efficiently compensates for the parametric heating, as the atoms now have a significant chance to survive even for sweep frequencies around 100 Hz. However, the data show that a lossless controlled transport works best without pump light and with moderate velocity.

For the coupling of two (or more) atoms, it is advantageous to use higher transverse modes of the cavity. Figure 5(a) shows the trace of a single atom that is repetitively swept across the TEM_{01} mode of the cavity over a distance of 250 μm, at a sweep frequency of 20 Hz. The cavity mode shows two transverse intensity maxima, and we can clearly distinguish the coupling of the atom to these two maxima on its way through the cavity. The most pronounced feature, however, is the vanishingly small photon-count rate when the atom is between these two maxima. This illustrates that we can control the position of an atom so precisely that it decouples from the cavity once we move it between two maxima of a higher-order mode.

Most promising is the extension of this scheme to two atoms coupled to the same cavity mode, which is shown in Fig. 5(b). If two atoms are initially captured, our loading scheme ensures a probability of 50% to have them in different maxima of the TEM_{01}-mode profile. It is now sufficient to sweep them to and fro along the dipole-trap axis to couple either each atom individually or both simultaneously to the cavity mode. The atoms can therefore be addressed individually via the cavity or, as the distance between the mode maxima of 42 μm can be easily resolved with optical microscopes, one can address them individually from the side using independent laser pulses.

The degree of control achieved over the atom-cavity coupling is a large step towards quantum information processing with a quantum register consisting of neutral atomic qubits, where each individual atom can be addressed by and strongly coupled to a cavity [17,18,20–22]. In particular, a cavity like ours (with unbalanced mirror reflectivity and an adjustable number of atoms in it) is ideally suited to generate single photons from one atom [17,18,21] or two photons from two atoms, etc., with long coherence time [22]. Moreover, the unitarity of the employed photon generation scheme is a way to deterministically entangle an atom and a photon, so that long-distance entanglement and teleportation between selected pairs of atoms in separate cavities are now possible in principle [23–25]. We are confident that our positioning scheme also works in a cavity with much smaller losses. Here, the deterministically controlled coupling of two atoms to the same mode (as demonstrated above) is a sine qua non for cavity-mediated quantum-gate operations [20,26].

This work was supported by the Deutsche Forschungsgemeinschaft (SPP 1078 and SFB 631) and the European Union [IST (QGATES) and IHP (CONQUEST) programs].

*Current address: ICFO Institut de Ciènces Fotòniques, Mediterranean Technology Park, 08860 Castelldefels (Barcelona), Spain.

[1] S. Kuhr *et al.*, Science **293**, 278 (2001).
[2] R. Dumke *et al.*, Phys. Rev. Lett. **89**, 097903 (2002).
[3] O. Mandel *et al.*, Nature (London) **425**, 937 (2003).
[4] S. Bergamini *et al.*, J. Opt. Soc. Am. B **21**, 1889 (2004).
[5] J. A. Sauer *et al.*, Phys. Rev. A **69**, 051804(R) (2004).
[6] W. Hänsel *et al.*, Phys. Rev. Lett. **86**, 608 (2001).
[7] R. Folman *et al.*, Adv. At. Mol. Opt. Phys. **48**, 263 (2002).
[8] P. Horak *et al.*, Phys. Rev. A **67**, 043806 (2003).
[9] G. R. Guthörlein *et al.*, Nature (London) **414**, 49 (2001).
[10] A. B. Mundt *et al.*, Phys. Rev. Lett. **89**, 103001 (2002).
[11] D. Kielpinski, C. Monroe, and D. Wineland, Nature (London) **417**, 709 (2002).
[12] J. McKeever *et al.*, Phys. Rev. Lett. **90**, 133602 (2003).
[13] P. Maunz *et al.*, Nature (London) **428**, 50 (2004).
[14] A. Boca *et al.*, Phys. Rev. Lett. **93**, 233603 (2004).
[15] P. Maunz *et al.*, Phys. Rev. Lett. **94**, 033002 (2005).
[16] P. Münstermann *et al.*, Phys. Rev. Lett. **82**, 3791 (1999).
[17] A. Kuhn, M. Hennrich, and G. Rempe, Phys. Rev. Lett. **89**, 067901 (2002).
[18] M. Keller *et al.*, Nature (London) **431**, 1075 (2004).
[19] S. Nußmann *et al.*, quant-ph/0506067 [Nature Physics (to be published)].
[20] T. Pellizzari *et al.*, Phys. Rev. Lett. **75**, 3788 (1995).
[21] J. McKeever *et al.*, Science **303**, 1992 (2004).
[22] T. Legero *et al.*, Phys. Rev. Lett. **93**, 070503 (2004).
[23] C. Cabrillo *et al.*, Phys. Rev. A **59**, 1025 (1999).
[24] S. Bose *et al.*, Phys. Rev. Lett. **83**, 5158 (1999).
[25] D. E. Browne, M. B. Plenio, and S. F. Huelga, Phys. Rev. Lett. **91**, 067901 (2003).
[26] A. Rauschenbeutel *et al.*, Phys. Rev. Lett. **83**, 5166 (1999).

ARTICLES

Vacuum-stimulated cooling of single atoms in three dimensions

STEFAN NUßMANN, KARIM MURR, MARKUS HIJLKEMA, BERNHARD WEBER, AXEL KUHN AND GERHARD REMPE*

Max-Planck-Institut für Quantenoptik, Hans-Kopfermann-Str. 1, D-85748 Garching, Germany

*e-mail: gerhard.rempe@mpq.mpg.de

Published online: 9 October 2005; doi:10.1038/nphys120

Controlling quantum dynamical processes is the key to practical applications of quantum physics, for example in quantum information science. The manipulation of light–matter interactions at the single-atom and single-photon level can be achieved in cavity quantum electrodynamics, in particular in the regime of strong coupling in which atom and cavity form a single entity. In the optical domain, this requires a single atom at rest inside a microcavity. Here we show that an orthogonal arrangement of a cooling laser, trapping laser and cavity vacuum gives rise to a unique combination of friction forces that act along all three directions. This combination of cooling forces is applied to catch and cool a single atom in a high-finesse cavity. The high cooling efficiency leads to a low temperature and an average single-atom trapping time of 17 s, during which the strongly coupled atom can be observed continuously.

The cooling and trapping of single atoms in a microcavity[1–13] is difficult, mainly because of the limited access and the complexity of the setup. Long trapping times have been achieved for ions, but not in the small cavities required for strong coupling[14,15]. Neutral atoms, in contrast, have been stored in the potential wells of a standing-wave dipole laser resonant with the microcavity[1–6]. In these experiments, the surprisingly short trapping times originated mainly from the axial geometry of the laser–cavity system. We have now changed this geometry and use a standing-wave dipole laser oriented perpendicular to the cavity axis. Moreover, an extra pump laser induces rapid three-dimensional cooling, an effect not anticipated for a deep dipole trap. Our findings result in a deterministic strategy for assembling a permanently bound and strongly coupled atom–cavity system.

As sketched in Fig. 1, our technique uses a standing-wave dipole-force trap and a pump beam that cross in the centre of a high-finesse optical cavity and run perpendicular to the cavity axis. The pump beam is near-resonant with the cavity, so that an atom in the crossing point scatters pump light into the cavity. The momentum kicks the atom experiences when scattering these photons lead to cooling of the atomic motion along the pump and cavity directions. This process is strongly enhanced by the Purcell effect[16] and has the unique advantage that cooling is effective over a large range of atomic-transition frequencies. It therefore allows one to catch a free atom on its flight through the cavity and to cool it down to the bottom of a deep potential well of the dipole trap, even though the average trap-induced a.c.-Stark shift of the atom increases as the localization improves. Strong cooling forces also act along the standing-wave axis and are caused by the delayed response of the atomic excitation and the intra-cavity field to a change in the atomic position. In our experiment, such a cold atom is well localized at an antinode of the standing-wave trap.

COOLING FORCES

The origin of the cooling forces can be understood from a simple model based on a two-level atom. Starting from a master equation that describes the coupling of the atom to the cavity mode, the pump and the dipole trap, one obtains four velocity-dependent forces, which we will discuss in more detail elsewhere. The first

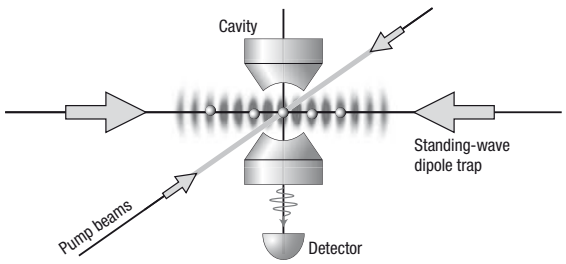

Figure 1 Schematic setup. An atom excited by counter-propagating pump beams scatters photons into a surrounding high-finesse cavity. This goes hand-in-hand with light-induced forces that trap and cool the atom into a single potential well of a deep standing-wave dipole trap.

two cooling forces below have been theoretically predicted[10–12]. A new cooling force along a further third direction arises from the presence of the dipole trap, which also provides a confining potential to localize the atom. Consider an atom that is exposed to a retro-reflected pump beam of photon momenta $\pm\hbar\mathbf{k}_P$ (where $\hbar$ is the reduced Planck's constant and $\mathbf{k}_P$ the photon wavevector), with a frequency ω_P close to the resonance ω_C of a surrounding cavity. The cavity provides a means for removing kinetic energy from the atom if the cavity resonance Δ_C is blue-detuned with respect to the pump ($\Delta_C = \omega_C - \omega_P > 0$). In this case, friction along the pump beams is caused by preferential absorption of photons travelling in the opposite direction to the atom. The Doppler effect shifts these photons towards the blue by $|\mathbf{k}_P \cdot \mathbf{v}|$ (where $\mathbf{v}$ is the atom's velocity), such that the coupled atom–cavity system becomes resonant with counter-propagating pump photons as soon as $\Delta_C + \mathbf{k}_P \cdot \mathbf{v} \approx 0$. This gives rise to a friction force,

$$\mathbf{F}_P = -4\hbar\mathbf{k}_P(\mathbf{k}_P \cdot \mathbf{v})\frac{\kappa\Delta_C}{(\Delta_C^2+\kappa^2)^2}g^2 P_E, \qquad (1a)$$

along each pump beam. For a fixed low-occupation probability of the atom's excited state, $P_E \simeq \Omega^2/(\Delta_A^2+\gamma^2)$ (valid for low saturation, where 2Ω is the Rabi frequency of the pump, γ is the polarization decay rate of the atom and $\Delta_A = \omega_A - \omega_P + \Delta_S$ is the effective pump detuning from the atomic resonance, ω_A, with Δ_S being the dipole-trap induced a.c.-Stark shift), the friction is only determined by the cavity parameters (g the atom–cavity coupling constant, κ the field-decay rate of the cavity). Momentum kicks from photon emissions into the resonator lead to a similar force that acts along the cavity axis,

$$\mathbf{F}_C = -4\hbar\nabla g(\nabla g \cdot \mathbf{v})\frac{\kappa\Delta_C}{(\Delta_C^2+\kappa^2)^2}P_E. \qquad (1b)$$

Photons emitted into the direction of motion are blue-detuned owing to the Doppler shift. These forward emissions also cool the atomic motion by recoil. If now the cavity is blue-detuned, the emissions in the direction of motion are favoured and hence the atom is cooled along the cavity axis. This simple picture does not consider interference effects leading to a spatial modulation of the cavity field, but it holds true if the force in equation (1b) is averaged over a spatial period.

The two forces above are seen as being due to distinct Doppler effects. However, they have a common origin, namely the dependency of the cavity field on the position of the atom. When the atom moves, the field takes a certain time ($\simeq\kappa^{-1}$) to adjust to a new steady-state. This time lag also gives rise to a third force along the standing wave axis,

$$\mathbf{F}_S^{Cav} = -4\hbar\nabla\Delta_S(\nabla\Delta_S \cdot \mathbf{v})\frac{\kappa\Delta_C}{(\Delta_C^2+\kappa^2)^2}\frac{g^2 P_E}{\Delta_A^2+\gamma^2}. \qquad (1c)$$

It acts along the direction of the standing wave and depends in the same way on Δ_C as the other two friction forces. It follows that the cavity, in combination with the pump and the trap, leads to cooling in three dimensions, with forces that all have the same order of magnitude.

Our scheme also profits from an unusual cooling force that is directed along the dipole trap. It can be explained by noting that an atom close to a node of the standing wave is not subject to an a.c.-Stark shift. For a pump frequency resonant to the atomic-transition frequency ω_A, the atom is resonantly pumped to the excited state. The atom now gains potential energy when moving in the standing wave, which is then lost by spontaneous emission (at a rate of 2γ) to the ground state. This is a Sisyphus-like cooling mechanism[17,18] that uses two different fields for trapping and cooling. The resulting force,

$$\mathbf{F}_S^{Sis} = -4\hbar\nabla\Delta_S(\nabla\Delta_S \cdot \mathbf{v})\frac{\Delta_A}{2\gamma(\Delta_A^2+\gamma^2)}P_E^2, \qquad (1d)$$

is cavity-independent and also provides cooling if $\Delta_C < 0$. As shown below, this force alone is sufficient to increase the trapping time. However, for $\Delta_C > 0$, cavity forces dominate and permanent photon scattering into the cavity takes place. Apart from cooling, all forces fluctuate and lead to heating of the atomic motion. The heating rate follows the lorentzian-shaped cavity resonance (apart from equation (1d)). In analogy to free-space laser cooling[19], a cavity-Doppler limited temperature around $k_B T \simeq \hbar\kappa$ (where k_B is the Boltzmann constant and T is temperature) is expected for $\Delta_C \simeq \kappa$. This unique combination of friction forces is unprecedented and it enables cooling of single dipole-trapped atoms in a cavity along all three directions. Here we apply this unusual combination of cooling forces to catch and cool a single atom in a high-finesse cavity, as discussed in the following.

CATCHING AND COOLING A SINGLE ATOM

In the experiment, we use a dipole-force trap to guide ^{85}Rb-atoms over a distance of 14 mm from a magneto-optical trap into the cavity. This trap is formed by a single horizontally running beam of an Yb:YAG laser, with focus between the magneto-optical trap and cavity. Once the atoms reach the cavity, we switch to a standing-wave dipole trap, formed by a pair of counter-propagating Yb:YAG laser beams (2 W; 1,030 nm, waist $w_0 = 16$ μm), tightly focused in the centre of the cavity. The antinodes of the standing wave represent 2.5 mK deep potential wells, that is, an a.c.-Stark shift of the atomic transition frequency in the centre of the wells of $\Delta_S = 2\pi \times 100$ MHz.

The 0.5 mm long cavity is formed by two mirrors of 5 cm radius of curvature that have different transmission coefficients (2 and 95 p.p.m.). The relevant atom–cavity parameters are $(g_0, \kappa, \gamma) = 2\pi \times (5, 5, 3)$ MHz, where g_0 is the atom–cavity coupling constant in an antinode, averaged over all magnetic sublevels of the $5\,^2S_{1/2}(F=3)$ to $5\,^2P_{3/2}(F'=4)$ transition. A Pound–Drever–Hall technique is used to lock the frequency of the TEM_{00} mode to the atomic-transition frequency. For this purpose, we use a reference laser that is red-detuned by eight free-spectral ranges (5 nm) from the atomic resonance. This laser acts as an extra standing-wave dipole trap along the cavity axis. Its potential wells are about 30 μK deep and show a good overlap with the resonant mode in the centre of the cavity. Together with the Yb:YAG standing-wave trap, it forms a two-dimensional optical lattice (calculated trap frequencies are

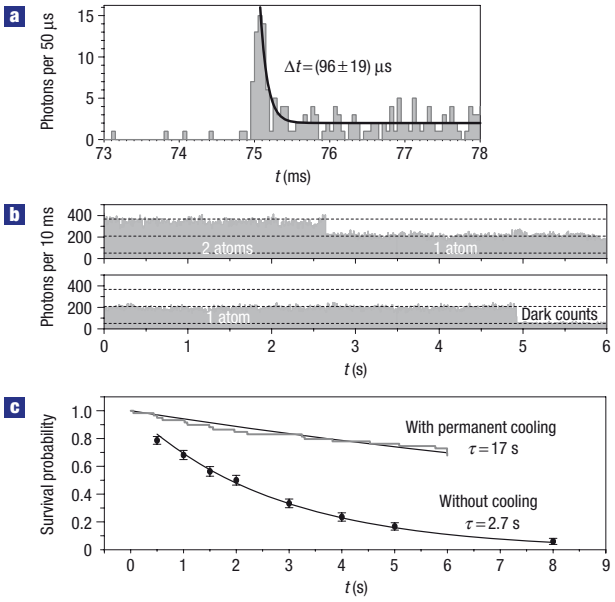

Figure 2 Single-atom traces and storage time. a, Atom capture. Photon-count rate for a pump Rabi-frequency $2\Omega = 2\pi \times 50$ MHz recorded as a function of time from the moment the standing wave is switched on. The trace shows an atom that is captured after 75 ms. Within 100 µs, the scattering rate reaches a steady-state value. **b**, Atom storage. Traces showing the photon-count rate after filtering (see the text). The signal allows us to determine the atom number and the trapping time. **c**, Lifetime. The analysis of 50 traces, each 6 s duration, starting with one atom yields an average lifetime τ of 17 s (upper trace), whereas single atoms that are not exposed to the pump laser only live for 2.7 s (• with errorbars indicating the standard error of the mean). The solid lines are an exponential fit.

$\nu_{sw} \simeq 670$ kHz in direction of the standing-wave trap, $\nu_{Cav} \simeq 100$ kHz along the cavity axis and $\nu_{\perp} \simeq 10$ kHz orthogonal to the cavity and the trapping laser).

In addition to these two conservative dipole traps, we continuously drive the $F = 3$ to $F' = 4$ transition with a pump laser that runs orthogonal to the cavity axis, at an angle of 45° to the standing-wave trap (Fig. 1). Together with a repump laser ($F = 2 \rightarrow F' = 3$), the beam has a focus ($w_0 = 35$ µm) at the intersection of cavity mode and dipole trap, and is retroreflected to balance its radiation pressure. To avoid an intensity modulation of the pump, the two counter-propagating beams have orthogonal polarization. Averaged over all magnetic sub-levels, it drives the atoms with a Rabi frequency $2\Omega = 2\pi \times 30$ MHz (all data, except Fig. 2a). Under these circumstances, the Purcell effect gives rise to photon scattering into the cavity at a rate

$$R_{scat} \simeq 2\kappa \cdot \frac{g^2}{\Delta_C^2 + \kappa^2} \cdot \frac{\Omega^2}{\Delta_A^2 + \gamma^2} \qquad (2)$$

for a single atom. For $\Delta_C = 0$, this gives a scattering rate of $R_{scat} \simeq 1{,}400$ ms^{-1}. In the experiment, we must take into account that the atom stops fluorescing whenever it falls into the dark state $5\,^2S_{1/2}(F = 2)$ and that repumping to $F = 3$ takes some time owing to the large a.c.-Stark shift. This leads to blinking and, from the measured count rate, we estimate that photons are scattered at the above rate only 1/5 of the time. Furthermore, owing to losses in the imaging system and the limited quantum efficiency of the detector, only 5% of the photons that are scattered into the cavity mode are finally detected behind the cavity mirror of higher transmission.

Once the atoms have been brought into the vicinity of the cavity, they are randomly distributed over the potential wells of the standing wave, with a small probability that an atom actually sits in the cavity. Some atoms have enough kinetic energy to move from well to well and as soon as such an atom enters the intersection of cavity mode and pump laser ($\Delta_C/2\pi = +2$ MHz and $\omega_P = \omega_A$ for capturing), it scatters photons into the cavity and is therefore cooled. In Fig. 2a, an experimental trace is shown where a single atom suddenly appears in the cavity. First the photon scattering rate is high, as the initially hot atom is poorly localized in the trap and the average experienced Stark shift Δ_S is small. This changes as the atom gets colder and therefore is better localized in the potential well. After a time $\Delta t \simeq 100$ µs, the atom reaches its final temperature and scatters at a much lower (but constant) rate, as it now experiences a much higher Δ_S close to the bottom of the potential. Starting from the simple estimation that the total kinetic energy, E, is lost during Δt with $\dot{E} \simeq E/\Delta t$, one calculates a mean friction coefficient, $\beta_{exp} = \dot{E}/2E \simeq 1/2\Delta t$, between 5 ms^{-1} (raw data) and 25 ms^{-1} (assuming blinking as discussed above). This is reasonably close to the expected value along the trap direction, $\beta_S = \beta_S^{Cav} + \beta_S^{Sis} = 14$ ms^{-1}, that one obtains from equations (1c) and (1d) with $\mathbf{F} = -\beta m\mathbf{v}$ (where m is the atomic mass and $\mathbf{F}$ denotes in general the forces defined in equations (1a)–(1d), with β denoting the respective friction coefficients, $\beta_P, \beta_C, \beta_S^{Cav}$ and β_S^{Sis}).

To prevent further atoms from penetrating into the cavity mode, we apply a filtering procedure. This is accomplished by a 10-ms-long interruption of the standing-wave trap. During this time, atoms inside the cavity stay trapped in the shallow intra-cavity dipole trap, but the other atoms are lost. If we turn the trap off and back on adiabatically, the probability for a caught atom to survive this procedure is higher than 50%. As shown in Fig. 2b, we then measure the photon rate to determine the exact number of atoms in the cavity[3]. The signal shows only small variations, which indicate a nearly constant atom–cavity coupling, and pronounced individual steps that occur whenever an atom is lost.

SINGLE-ATOM TRAPPING TIME

As shown in Fig. 2c, dipole-trapped atoms show an average lifetime τ of 2.7 s if we switch off the pump laser. However, if an atom is continuously illuminated and coupled to the cavity with $\Delta_C \geq 0$, the lifetime increases, reaching values exceeding 20 s. This impressively demonstrates that a strong cooling mechanism is active. For $\Delta_C = 0$, in particular, a lifetime of about 17 s is measured. In this case, no cavity cooling is expected and in our model the long lifetime comes solely from the Sisyphus-like mechanism, equation (1d). Cavity cooling, equations (1a)–(1c), is expected to give much longer trapping times for $\Delta_C \approx +\kappa$. For technical reasons, however, longer trapping times could not be registered in our experiment. We have therefore deliberately modulated the depth of the trapping potential (that is, the intensity of the Yb:YAG trapping laser) by 30% at a frequency of 7 kHz. This leads to parametric heating and shortens the trapping time, so that systematic lifetime measurements can be made within a reasonable time. Without cooling, the modulation reduces the trapping time to (22 ± 5) ms. We now have performed measurements such as those in Fig. 2c for several different cavity detunings. The single-atom lifetime as a function of Δ_C is plotted in Fig. 3. Obviously, the lifetime increases to about 100 ms as soon as the pump laser is present, even if Δ_C is so large ($2\pi \times 50$ MHz) that the cavity has no effect. Moreover, a cavity close to resonance significantly extends the lifetime. For a blue-detuned cavity, with $\Delta_C \simeq +\kappa$, a 20-fold increase of the lifetime to a maximum of ≃400 ms is obtained, whereas a red-detuned cavity, with $\Delta_C \simeq -\kappa$, leads to a minimum lifetime. To compare these results

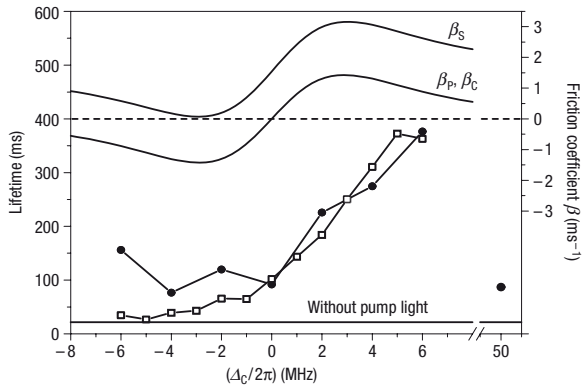

Figure 3 Trapping time and friction forces as a function of the cavity detuning, Δ_C. The data points show the lifetime of atoms that are subject to strong parametric heating, with either $\omega_P = \omega_A$ (●) or $\omega_C = \omega_A$ (□). An extended trapping time is found for almost all detunings if pump light is present. A maximum is reached when the cavity is slightly blue detuned with respect to the laser. This is also expected from the friction coefficients β_P, β_C and β_S. Although the forces along pump and cavity axis change sign, the total friction along the standing-wave dipole trap, $\beta_S = \beta_S^{Cav} + \beta_S^{Sis}$, is always positive owing to the Sisyphus effect.

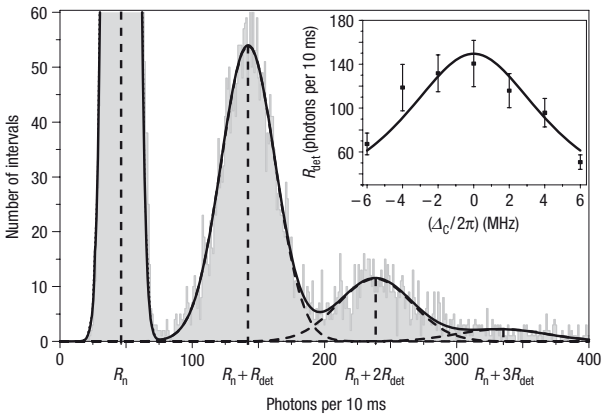

Figure 4 Photon-count histogram measured for $\Delta_C/2\pi = +4$ MHz using 10 ms count intervals. The maxima (left to right) stem from background noise (rate R_n) and from one, two or more atoms. The solid line is a fit of four gaussians to the data. They are centred at $R_n + n \cdot R_{det}$, and are $\left(R_n + n \cdot R_{det} + n \cdot \sigma^2_{R_{det}}\right)^{1/2}$ wide ($n = 0, 1, 2, 3$). R_{det} is the detected photon-count rate per atom, which is also shown in the inset as a function of Δ_C (■ with errorbars indicating $\sigma(R_{det})$), together with the expectation from equation (2) as a solid line, with adapted overall amplitude.

with the theoretical model, the expected friction coefficients are also shown in Fig. 3. Although these values cannot be directly compared with the lifetime, qualitative conclusions can be drawn. First, the cavity-independent Sisyphus cooling, predicted only along the standing-wave axis, accounts for the cavity-independent increase of the lifetime with respect to atoms left in the dark. The variation of the lifetime with Δ_C finds its correspondence in the predicted course of the friction coefficients due to the cavity cooling for all three dimensions. Obviously, cavity cooling increases the trapping time by a factor of four if compared with Sisyphus cooling alone. Without further limitations, such as background gas collisions, we can therefore expect the 17 s lifetime observed without the trap modulation at $\Delta_C = 0$ to increase to about one minute in the presence of the cavity cooling at $\Delta_C \approx +\kappa$.

ATOMS BY THE NUMBER

For the same data, we have also analysed the average count rate per atom using 10 ms time bins. Figure 4 depicts the photon-count histogram. The well-distinct peaks stem from dark counts and traces with one, two or more trapped atoms. From a fit to these data, we can derive the average count rate per atom, R_{det}, and its statistical spread, $\sigma(R_{det})$, that is corrected for shot noise. The results are plotted in the inset of Fig. 4 as a function of Δ_C. If we assume that all variations of R_{det} are caused by variations in the atom–cavity coupling, then from equation (2) we obtain $\Delta g/g = \sigma(R_{det})/2R_{det} = \pm 8.6\%$ (for $\Delta_C/2\pi = +4$ MHz). This can only be explained with an atom distribution among the different wells of the standing wave that is less than ± 9 μm wide. Under the assumption that the distribution in the filter phase is mapped to the standing-wave trap during the adiabatic transfer, this indicates a temperature below 6 μK during filtering.

GROUND-STATE COOLING

To obtain an estimate of the temperature in the deep two-dimensional-lattice, we analysed the auto-correlation function of the emitted photon stream. In this signal, a periodic modulation at $2 \times \nu_{Cav}$ (the trap frequency along the cavity axis) is found, with a visibility of about 5%. This is indeed expected for an atom that oscillates in the weak intra-cavity dipole trap, without ever reaching the nodes of the cavity mode. The $k_B \times 30$ μK depth of the intra-cavity trap can therefore be seen as an upper limit of the atomic energy. The mean kinetic energy cannot surpass 50% of this value, which corresponds to a temperature of 15 μK. Assuming the same temperature in all directions, this limits the mean vibrational quantum number for the motion along the standing-wave dipole trap to $\bar{n} = 0.13$, that is, the atom is in the vibrational ground state with at least 88% probability.

CONCLUSION

Our experiment demonstrates how to capture single atoms with a three-dimensional cavity-cooling scheme. Qualitatively, our results show good agreement with the predictions of a model valid for a two-level atom, although an understanding of the remarkably good localization of the atom calls for a more detailed theoretical analysis, including polarization effects of the incident pump laser[20], the multilevel structure and even the quantum motion of the atom[21,22]. At present, our method allows the preparation of an exactly known number of atoms at low temperatures in the centre of a high-finesse optical cavity. With average trapping times exceeding 15 s, single-atom cavity physics is now at a stage where fully controlled atom–photon experiments in the strong atom–cavity coupling regime can be started.

Received 28 June 2005; accepted 26 August 2005; published 9 October 2005.

References

1. Ye, J., Vernooy, D. W. & Kimble, H. J. Trapping of single atoms in cavity qed. *Phys. Rev. Lett.* **83,** 4987–4990 (1999).
2. McKeever, J. *et al.* State-insensitive cooling and trapping of single atoms in an optical cavity. *Phys. Rev. Lett.* **90,** 133602 (2003).
3. McKeever, J., Buck, J. R., Boozer, A. D. & Kimble, H. J. Determination of the number of atoms trapped in an optical cavity. *Phys. Rev. Lett.* **93,** 143601 (2004).
4. Boca, A. *et al.* Observation of the vacuum Rabi spectrum for one trapped atom. *Phys. Rev. Lett.* **93,** 233603 (2004).
5. Maunz, P. *et al.* Cavity cooling of a single atom. *Nature* **428,** 50–52 (2004).

6. Maunz, P. *et al*. Normal-mode spectroscopy of a single bound atom-cavity system. *Phys. Rev. Lett.* **94,** 033002 (2005).
7. Mossberg, T. W., Lewenstein, M. & Gauthier, D. J. Trapping and cooling of atoms in a vacuum perturbed in a frequency-dependent manner. *Phys. Rev. Lett.* **67,** 1723–1726 (1991).
8. Doherty, A. C., Parkins, A. S., Tan, S. M. & Walls, D. F. Motion of a two-level atom in an optical cavity. *Phys. Rev. A* **56,** 833–844 (1997).
9. Horak, P., Hechenblaikner, G., Gheri, K. M., Stecher, H. & Ritsch, H. Cavity-induced atom cooling in the strong coupling regime. *Phys. Rev. Lett.* **79,** 4974–4977 (1997).
10. Vuletić, V. & Chu, S. Laser cooling of atoms, ions, or molecules by coherent scattering. *Phys. Rev. Lett.* **84,** 3787–3790 (2000).
11. Vuletić, V., Chan, H. W. & Black, A. T. Three-dimensional cavity Doppler cooling and cavity sideband cooling by coherent scattering. *Phys. Rev. A* **64,** 033405 (2001).
12. Domokos, P., Vukics, A. & Ritsch, H. Anomalous Doppler-effect and polariton-mediated cooling of two-level atoms. *Phys. Rev. Lett.* **92,** 103601 (2004).
13. Murr, K. On the suppression of the diffusion and the quantum nature of a cavity mode. Optical bistability: Forces and friction in driven cavities. *J. Phys. B* **36,** 2515–2537 (2003).
14. Guthörlein, G. R., Keller, M., Hayasaka, K., Lange, W. & Walther, H. A single ion as a nanoscopic probe of an optical field. *Nature* **414,** 49–51 (2001).
15. Mundt, A. B. *et al*. Coupling a single atomic quantum bit to a high finesse optical cavity. *Phys. Rev. Lett.* **89,** 103001 (2002).
16. Purcell, E. M. Spontaneous emission probabilities at radio frequencies. *Phys. Rev.* **69,** 681 (1946).
17. Dalibard, J. & Cohen-Tannoudji, C. Dressed-atom approach to atomic motion in laser light: The dipole force revisited. *J. Opt. Soc. Am. B* **2,** 1707–1720 (1985).
18. Taïeb, R., Dum, R., Cirac, J. I., Marte, P. & Zoller, P. Cooling and localization of atoms in laser-induced potential wells. *Phys. Rev. A* **49,** 4876–4887 (1994).
19. Cohen-Tannoudji, C. in *Fundamental Systems in Quantum Optics, Les Houches, Session LIII, 1990* (eds Dalibard, J., Raimond, J. M. & Zinn-Justin, J.) 1–164 (Elsevier Science, North-Holland, Amsterdam, 1992).
20. Cirac, J. I., Blatt, R., Parkins, A. S. & Zoller, P. Laser cooling of trapped ions with polarization gradients. *Phys. Rev. A* **48,** 1434–1445 (1993).
21. Cirac, J. I., Lewenstein, M. & Zoller, P. Laser cooling a trapped atom in a cavity: Bad cavity limit. *Phys. Rev. A* **51,** 1650–1655 (1995).
22. Zippilli, S. & Morigi, G. Cooling trapped atoms in optical resonators. Preprint at http://arxiv.org/quant-ph/0506030 (2005).

Acknowledgements

This work was supported by the Deutsche Forschungsgemeinschaft (SPP 1078 and SFB 631) and the European Union (IST (QGATES) and IHP (CONQUEST) programs). We are also grateful to S. Webster for helpful comments.
Correspondence and requests for materials should be addressed to G.R.

Competing financial interests

The authors declare that they have no competing financial interests.

PRL 96, 253001 (2006) PHYSICAL REVIEW LETTERS week ending 30 JUNE 2006

Large Velocity Capture Range and Low Temperatures with Cavities

K. Murr

Max-Planck-Institut für Quantenoptik, Hans-Kopfermann-Strasse 1, D-85748 Garching, Germany

(Received 15 January 2006; published 26 June 2006)

There are interesting modifications to the Doppler force when atoms strongly couple to an optical cavity. In particular, there is the possibility to increase the velocity capture range while maintaining a final temperature close to the Doppler limit. The mechanism is based on the multiple absorption emissions of each cavity photon. A previously reported counterintuitive Doppler effect is clarified.

DOI: 10.1103/PhysRevLett.96.253001 PACS numbers: 32.80.Pj

One of the main problems in laser cooling of atoms is to obtain a large velocity capture range and, at the same time, low temperatures [1]. In Doppler cooling, both the capture range and the lowest temperature depend on the width 2γ of the absorbtion peak. Polarization gradients lead to lower temperatures, but the capture range is also reduced. Use of bichromatic light, e.g., see [2], can significantly increase the capture range, but the temperature also increases. In general, a solution to such a problem requires the full-velocity dependence of the light forces.

Here is a study on the effect of optical cavities on the velocity selectivity, see Fig. 1. Several important works have already been concerned with the cooling of atoms inside cavities [3–12] (and references therein). The only theory that clearly addresses the velocity selectivity is presented in [3,4]. They derived a force for all velocities, deduced the capture range and found that, like the lowest temperature, it depends *only* on the cavity linewidth 2κ. Because κ is independent of the species, this so-called "cavity Doppler" force seems promising for cooling particles with a complex internal structure. However, it also suffers from the same problem encountered in the Doppler force: One has to choose between a low final temperature (low κ), or a large capture range (large κ).

Other theories [5,6] have focused on the first order velocity force $\boldsymbol{F}^v \approx -\boldsymbol{\beta}\boldsymbol{v} + \mathcal{O}(\boldsymbol{v}^2)$, but, in contrast to Refs. [3,4], all the orders in the atom-cavity interaction were included. This restriction on the velocity $\boldsymbol{v}$ leads to problems, starting with the understanding of the friction $\boldsymbol{\beta}$. Another related problem also has been reported [6]. Here, it is an intriguing effect, which purports that an atom counterpropagating laser photons would "see" them Doppler shifted to the red, rather than to the blue [6]. This counterintuitive Doppler effect is due to the presence of the cavity mirrors, it would have an impact on the motion and needs to be clarified.

This Letter extracts the essential information on the velocity-dependent light pressure for atoms coupled to an optical cavity at low saturation. We derive a force which naturally contains the Doppler force and extends (above the recoil energy) that in [3,4] to arbitrary order in the coupling g between atom and cavity field. Consequently, it is shown to be in principle possible to achieve a large velocity capture range, but with a temperature approaching that in open space. We end by showing that an atom always sees laser photons Doppler shifted in the usual way; but the atom also scatters photons into the cavity. Those are also Doppler shifted and, hence, create a light shift that now depends on the velocity. The first order in $\boldsymbol{v}$ of this light shift reproduces the anomaly [6].

Compared to open space, a cavity provides two new ingredients: First, the confinement due to the mirrors allows the cavity field and the atom to reciprocally affect each other. The Rabi splitting is an example of such a strong mutual influence [13,14]. Second, the escape of photons through the cavity mirrors offers a new loss channel. Consider first a ring cavity, as depicted in Fig. 1(a). The atom is excited [3–7] by laser photons of momentum $\hbar\boldsymbol{k}_L$, but also couples to two cavity fields, 1 and 2, counterpropagating with momenta $\hbar\boldsymbol{k}_1 = -\hbar\boldsymbol{k}_2$. All processes that start with an absorption of a laser photon and end up in stimulated emission back into the laser field will leave the atom's momentum unchanged. Those include the simplest case of a direct absorbtion + stimulated-emission process [1], but also all the other possibilities that involve the cavity. For example, a laser photon can be first absorbed, emitted into the cavity via mode 1, absorbed after a round trip, and then emitted by stimulated emission along the laser; no net momentum change. Consider now the process where a laser photon is absorbed ($+\hbar\boldsymbol{k}_L$), emitted into mode 2 ($-\hbar\boldsymbol{k}_2$), absorbed ($+\hbar\boldsymbol{k}_2$), emitted into mode 1

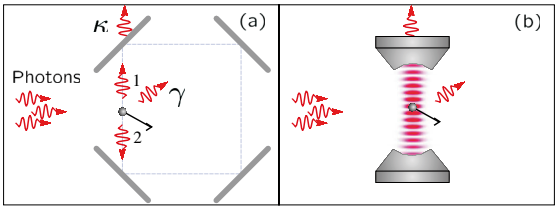

FIG. 1 (color online). An atom experiences a Doppler force which is modified due to the presence of cavity mirrors: (a) ring cavity; (b) linear cavity. The amount of light collected at the output of a mirror highly depends on the velocity of the particle.

PRL 96, 253001 (2006) PHYSICAL REVIEW LETTERS week ending 30 JUNE 2006

$(-\hbar\boldsymbol{k}_1)$, and then leaks out from a mirror. The net momentum transferred to the atom is in that case $\hbar\boldsymbol{k}_L - \hbar\boldsymbol{k}_1$. It is the same momentum as in a direct absorption + one-emission + leakage process [3,4]. The major difference is that our example is of order $g_2^2 g_1$ in the coupling between atom and the cavity modes, rather than g_1 for the direct process. Consider the number N_i^{out} of such processes, where the final emission is into mode i before the photon leaks out from a mirror. All those processes produce the same net momentum $\hbar\boldsymbol{k}_L - \hbar\boldsymbol{k}_i$, while they depend on the couplings according to which photon history is followed in the cavity prior to the last emission into mode i. One then repeats similar arguments for the number $N_{\text{s.e.}}^{\text{out}}$ of the spontaneous emission processes. Therefore, the relevant net momentum can be written $\boldsymbol{p} = \hbar\boldsymbol{k}_L N_{\text{s.e.}}^{\text{out}} - \sum_l \hbar\boldsymbol{k}_l + \sum_i (\hbar\boldsymbol{k}_L - \hbar\boldsymbol{k}_i) N_i^{\text{out}}$, for time intervals $t > (\kappa^{-1}, \gamma^{-1})$ long compared to the lifetime $1/2\gamma$ of the upper state and that of a cavity photon $1/2\kappa$. Here, $\hbar\boldsymbol{k}_l$ is the momentum of the lth fluorescence photon ($l = 1, N_{\text{s.e.}}^{\text{out}}$). In steady state one has $\langle \sum_l \hbar\boldsymbol{k}_l \rangle = \boldsymbol{0}$, $\langle N_{\text{s.e.}}^{\text{out}} \rangle = 2\gamma P_e t$, where $2\gamma P_e$ is the spontaneous emission rate (P_e is the upper state occupation probability), and $\langle N_i^{\text{out}} \rangle = 2\kappa N_{\text{cav},i} t$, given by the mean cavity photon number $N_{\text{cav},i}$ in mode i. The total steady state force thus reads $\boldsymbol{F} = \boldsymbol{F}_{k_L} + \boldsymbol{F}_1 + \boldsymbol{F}_2$:

$$\boldsymbol{F}_{k_L}(\boldsymbol{v}) = \hbar\boldsymbol{k}_L (2\gamma P_e + 2\kappa N_{\text{cav},1} + 2\kappa N_{\text{cav},2}), \quad (1a)$$

$$\boldsymbol{F}_i(\boldsymbol{v}) = -\hbar\boldsymbol{k}_i 2\kappa N_{\text{cav},i}. \quad (1b)$$

The term $\hbar\boldsymbol{k}_L 2\gamma P_e$ is the Doppler force, but here it depends on the coupling to the cavity as well as additional Doppler shifts. The force $\boldsymbol{F}_{k_L}$ is referred to as the force acting along the laser axis, although such a terminology is correct only when the $\boldsymbol{k}_i' s$ are orthogonal to $\boldsymbol{k}_L$. It is proportional to the rate at which photons are removed from the laser and shows the most interesting behavior as a function of velocity, as considered hereafter.

The diffusion constant $2D = d/dt\langle(\Delta\boldsymbol{p})^2\rangle$ is derived along the same lines [15]. Since $N_{\text{s.e.}}^{\text{out}}$ and N_i^{out} are random and statistically independent variables, the mean momentum spread reads $\langle(\Delta\boldsymbol{p})^2\rangle = \langle N_{\text{s.e.}}^{\text{out}}\rangle(\hbar k)^2 + \langle(\Delta N_{\text{s.e.}}^{\text{out}})^2\rangle \times (\hbar\boldsymbol{k}_L)^2 + \sum_i (\hbar\boldsymbol{k}_L - \hbar\boldsymbol{k}_i)^2 \langle(\Delta N_i^{\text{out}})^2\rangle$, $(k = \omega_{\text{eg}}/c \approx |\boldsymbol{k}_L|$, where ω_{eg} is the atomic transition frequency). The first two terms are those of the open space theory, except that they take into account the presence of the cavity. The two other diffusion terms are due to the dispersion in the number of photons that leak out from the cavity. We consider the regime of low atomic saturation $P_e \ll 1$ and where the internal state of the atom is treated as a dipole oscillator. Precisely, the situation resumes to linearly coupled atom-cavity oscillators. In this case, the statistics follow the Poisson law $\langle(\Delta N)^2\rangle = \langle N\rangle$, thus: $2D(\boldsymbol{v}) = (\hbar k)^2 2\gamma P_e + (\hbar k_L)^2 2\gamma P_e + \sum_i (\hbar\boldsymbol{k}_L - \hbar\boldsymbol{k}_i)^2 2\kappa N_{\text{cav},i}$.

The force and diffusion are entirely known from the excitation probability $P_e(\boldsymbol{v})$ and mean photon number per mode $N_{\text{cav},i}(\boldsymbol{v})$. Those in turn depend on the velocity through Doppler shifts. The choice of a ring cavity in order to extract the essential physics is due to the fact that it sustains running wave modes. Therefore, one can invoke the Doppler shift in a simple manner in all directions by moving to the atom's rest frame. In that way, the atom sees laser photons of frequency $\omega_L - \boldsymbol{k}_L \cdot \boldsymbol{v}$, while the cavity receives photons of frequency $\omega_L - (\boldsymbol{k}_L - \boldsymbol{k}_i)\cdot\boldsymbol{v}$ $(i = 1, 2)$. One thus calculates the expectation values for an atom at rest, includes the Doppler shifts, and obtains the excitation probability P_e and cavity-photon number in mode i $N_{\text{cav},i}$:

$$P_e = \frac{\eta_0^2}{(\Delta_a + \boldsymbol{k}_L\cdot\boldsymbol{v})^2 + \gamma^2} \frac{1}{|1 - \nu_1(\boldsymbol{v}) - \nu_2(\boldsymbol{v})|^2}, \quad (2a)$$

$$N_{\text{cav},i} = \frac{g_i^2 P_e}{[\Delta_c + (\boldsymbol{k}_L - \boldsymbol{k}_i)\cdot\boldsymbol{v}]^2 + \kappa^2}. \quad (2b)$$

Here, $\Delta_a = \omega_{\text{eg}} - \omega_L$ and $\Delta_c = \omega_{\text{cav}} - \omega_L$ are the atomic and cavity detunings, respectively, where $\omega_{\text{cav}} = c|\boldsymbol{k}_i|$ is the cavity resonance frequency. The atom-laser Rabi frequency is $2\eta_0$, while $2g_i$ is the vacuum Rabi frequency for atom-mode i, neglecting the waist profiles [1]. Of particular importance is the velocity-dependent generalized atom-mode i cooperativity parameter:

$$\nu_i(\boldsymbol{v}) = \frac{g_i^2}{(\Delta_a + \boldsymbol{k}_L\cdot\boldsymbol{v} - i\gamma)(\Delta_c + (\boldsymbol{k}_L - \boldsymbol{k}_i)\cdot\boldsymbol{v} - i\kappa)}. \quad (3)$$

Last, we introduce the effective atomic decay rate γ_{eff} and detuning Δ_{eff}

$$\gamma_{\text{eff}}(\boldsymbol{v}) = \gamma + \sum_{i=1,2} \frac{g_i^2 \kappa}{[\Delta_c + (\boldsymbol{k}_L - \boldsymbol{k}_i)\cdot\boldsymbol{v}]^2 + \kappa^2}, \quad (4a)$$

$$\Delta_{\text{eff}}(\boldsymbol{v}) = \Delta_a + \boldsymbol{k}_L\cdot\boldsymbol{v} - \sum_{i=1,2} \frac{g_i^2[\Delta_c + (\boldsymbol{k}_L - \boldsymbol{k}_i)\cdot\boldsymbol{v}]}{[\Delta_c + (\boldsymbol{k}_L - \boldsymbol{k}_i)\cdot\boldsymbol{v}]^2 + \kappa^2}. \quad (4b)$$

The excitation probability and the force now *strictly* read $P_e(\boldsymbol{v}) = \eta_0^2/(\Delta_{\text{eff}}^2 + \gamma_{\text{eff}}^2)$ (2a) and $\boldsymbol{F}_{k_L}(\boldsymbol{v}) = \hbar\boldsymbol{k}_L 2\gamma_{\text{eff}} P_e$ (1a). In particular, when the frequency $\omega_L - (\boldsymbol{k}_L - \boldsymbol{k}_i)\cdot\boldsymbol{v}$ of the emitted photons is resonant to the cavity ω_{cav}, one has $\gamma_{\text{eff}} = \gamma(1 + 2C)$, where $2C = g^2/\kappa\gamma$ (Purcell enhancement factor), with $g^2 = g_1^2 + g_2^2$. Consequently, for $C \gg 1$, the light pressure is very large for a fixed excitation probability.

Starting from a master equation [5,15], we will show elsewhere that all those results are exact solutions for a dipole oscillator, for all g_i and $\boldsymbol{v}$. We also mention the following properties: (i) As in the Doppler force, for a laser standing wave it is possible at low saturation to add the independent contributions of each laser running wave provided the force is spatially averaged along the laser axis. (ii) For a linear cavity, Fig. 1(b), the force $\boldsymbol{F}_{k_L}$ (1a) is correct if one sets $\boldsymbol{k}_i \cdot \boldsymbol{v} = 0$ in Eqs. (2)–(4), and assumes

PRL 96, 253001 (2006) PHYSICAL REVIEW LETTERS week ending 30 JUNE 2006

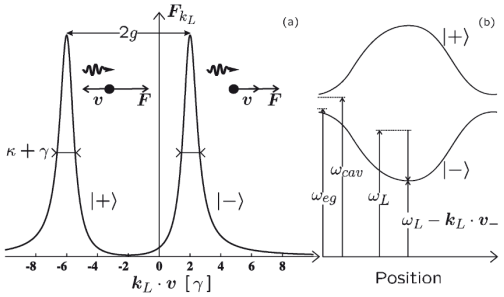

FIG. 2. (a) Example of the force $\boldsymbol{F}_{k_L}$ as a function of velocity, for ($\kappa = 0.1\gamma$, $g = 4\gamma$, $\Delta_c = \Delta_a = 2\gamma$). The scaling is arbitrary. The Doppler shift tunes the photons to be resonant with the eigenstates $|+\rangle$ and $|-\rangle$ of the atom-cavity system when $\boldsymbol{k}_L \cdot \boldsymbol{v}_\pm = -\Delta_\pm \approx -\Delta_a \mp g$, ($\Delta_\pm = \omega_\pm - \omega_L$). (b) Resonance frequencies $\omega_\pm$ of the coupled atom-cavity system as a function of the atom's position orthogonal to the cavity.

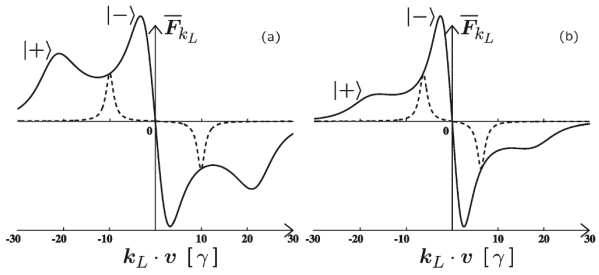

FIG. 3. Spatially averaged force $\bar{\boldsymbol{F}}_{k_L}$ for a laser standing wave as a function of velocity, for ($\kappa = 8\gamma$, $\Delta_c = 1.8\kappa$): (a) ($g = 1.3\kappa$, $\Delta_a = 10\gamma$); (b) ($g = \kappa$, $\Delta_a = 6.3\gamma$). For decreasing g or increasing Δ_c, the lowest peaks (state $|+\rangle$) disappear and one recovers the narrow Doppler peaks (dashed line). In both figures, the force is effective over a large range of velocities $\Delta v_c \approx 16\gamma/k_L$, but the temperature is close to the Doppler limit: (a) $k_B T_{k_L} \approx 2.1\hbar\gamma$; (b) $k_B T_{k_L} \approx 1.7\hbar\gamma$.

g fixed. (iii) The same spatial averaging then still holds for $\boldsymbol{F}_{k_L}$ when a laser standing wave is used. (iv) Equation (1b) cannot be used for a linear cavity, in particular, because Doppleron resonances occur [1,16].

If the atom is decoupled from the cavity $g_i = 0$, then $\nu_i = 0$ and one recovers the usual Lorentz absorption curve (2a). Hence, the presence of the cavity in Eq. (2a) is entirely contained in the parameters ν_i (3). The force in [3,4] is recovered for $\nu_i \to 0$, met for large detuning Δ_a ($\nu_i \propto 1/\Delta_a$) and dropping the usual Doppler shift in Eq. (2a) as well as the term $2\gamma P_e$ in Eq. (1a). In that case, the force (1) consists of one single peak as a function of velocity, corresponding to the cavity Lorentz shape explicit in Eq. (2b).

Figure 2(a) shows the force as a function of $\boldsymbol{v}$ ($\boldsymbol{k}_i \cdot \boldsymbol{v} = 0$). The velocity dependence of the ν_i's (3) is responsible for the appearance of two peaks. Their presence in Eqs. (2) is due to the multiple interactions a cavity photon can have with the atom prior to the occurrence of dissipation. Those multiple interactions are favored when the Doppler effect shifts the laser and cavity photons on resonance with the combined atom-cavity system, $\nu_1 + \nu_2 \to 1$, yielding a velocity selectivity on the dressed states frequencies $\omega_\pm = \omega_L - \boldsymbol{k}_L \cdot \boldsymbol{v}_\pm$. In the simple case of Fig. 2(a) (where $\Delta_a = \Delta_c$), the peaks are separated by $2g$, and each has a linewidth of $\gamma + \kappa$. The distance between the mirrors and their reflectivity determines κ and g.

In particular, for $g \approx \kappa > \gamma$, both peaks broaden and merge together. This is shown in Fig. 3 for two counterpropagating laser beams. Here, the force addresses a class of velocities (roughly $\Delta v_c \approx 2\kappa/k_L$) that is broader than that of the Doppler force ($2\gamma/k_L$). Moreover, in this "bad-cavity" limit, the friction force (per beam) along the laser is approximately $\boldsymbol{F}^v_{k_L} \approx -4\hbar \boldsymbol{k}_L (\boldsymbol{k}_L \cdot \boldsymbol{v}) P_e \gamma_{\text{eff}} \Delta_{\text{eff}} / (\Delta^2_{\text{eff}} + \gamma^2_{\text{eff}})$, where ($P_e$, Δ_{eff}, γ_{eff}) are now evaluated at $\boldsymbol{v} = \boldsymbol{0}$. Thus, combined with the diffusion term given above (with $\boldsymbol{v} = \boldsymbol{0}$), the minimum temperature is obtained for $\Delta_{\text{eff}} = \gamma_{\text{eff}}$, and is given by $k_B T^{\text{app}}_{k_L} \approx \hbar(\gamma + \gamma_{\text{eff}})/2$. Hence, with reasonable values for (g, κ) and a cavity detuning $\Delta_c \gtrsim \kappa$ (Δ_a is fixed by $\Delta_{\text{eff}} = \gamma_{\text{eff}}$), the temperature can be kept close to the Doppler limit, $\gamma_{\text{eff}} \gtrsim \gamma$. For Fig. 3, the temperature is indeed as low as $k_B T_{k_L} \approx 2\hbar\gamma$ (and is close to the approximation $k_B T^{\text{app}}_{k_L}$). One also sees in Fig. 4(a) that $k_B T_{k_L}$ remains fairly low as κ increases, whereas the capture range tends to enlarge (not shown). Finally, by increasing the coupling g, with g/Δ_c fixed and $\Delta_{\text{eff}} = \gamma_{\text{eff}}$, the peak of state $|+\rangle$ moves towards higher velocities $|\boldsymbol{v}|$ [see Fig. 3(a)], thereby increasing the capture range, while that of state $|-\rangle$ remains close to $|\boldsymbol{v}| = 0$ and ensures low temperatures. So far, the temperature along the cavity axis has not been mentioned. In a ring cavity this temperature can be high, in particular, it tends to $\hbar\Delta_c/4$ for $\Delta_c \gg \kappa$. In sharp contrast, a linear cavity gives Doppler-like temperatures for all directions [5].

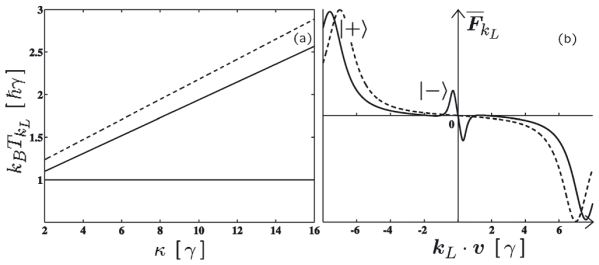

FIG. 4. Spatially averaged temperature as a function of the cavity decay rate κ, for ($g = \kappa$, $\Delta_c = 1.8\kappa$) and Δ_a such that $\Delta_{\text{eff}}(0) = \gamma_{\text{eff}}(0)$. The temperature $k_B T_{k_L}$ (solid line) [and $k_B T^{\text{app}}_{k_L}$ (dashed line)] is close to the Doppler limit $\hbar\gamma$ (horizontal line). For $\kappa = 16\gamma \gg \gamma$ it is only $k_B T_{k_L} \approx 2.5\hbar\gamma$. (b) Sub-Doppler cooling: Force (solid line) and the Doppler force (dashed line), ($\kappa = 0.2\gamma$, $g = 2\gamma$, $\Delta_c = 0.9\gamma$, $\Delta_a = 7\gamma$). The narrow peak around $v = 0$ is responsible for sub-Doppler cooling $\kappa \ll \gamma$.

PRL 96, 253001 (2006) PHYSICAL REVIEW LETTERS week ending 30 JUNE 2006

For completeness and comparison, Fig. 4(b) shows a characteristic curve for sub-Doppler cooling $k_B T_{k_L} \approx \hbar\kappa \ll \hbar\gamma$ [reached for $\Delta_a \gg (\Delta_c, g, \gamma)$]. It reveals a capture range that is close to that of the Doppler force (due to state $|+\rangle$), plus a narrower one where cavity-induced sub-Doppler cooling takes place (due to state $|-\rangle$). This is similar to polarization gradient cooling, i.e., the force has a Doppler part plus an extra contribution which ensures sub-Doppler temperatures [1]. Since the peaks here are well resolved, the friction force per beam is now $\boldsymbol{F}^{v}_{k_L} \approx -4\hbar\boldsymbol{k}_L(\boldsymbol{k}_L \cdot \boldsymbol{v})N_{\mathrm{cav}}\Gamma_-\Delta_-/(\Delta_-^2 + \Gamma_-^2)$, where $N_{\mathrm{cav}} = \sum_i N_{\mathrm{cav},i}$, and where $\Delta_- = \frac{1}{2}(\Delta_a + \Delta_c) - \frac{1}{2}\,\mathrm{Re}\sqrt{4g^2 + [\Delta_{ac} - i(\gamma - \kappa)]^2}$ and $\Gamma_- = \frac{1}{2}(\gamma + \kappa) + \frac{1}{2}\,\mathrm{Im}\sqrt{4g^2 + [\Delta_{ac} - i(\gamma - \kappa)]^2}$ ($\Delta_{ac} = \omega_{\mathrm{eg}} - \omega_{\mathrm{cav}}$) are the detuning and decay rate of state $|-\rangle$. Cooling occurs for $\Delta_- > 0$, i.e., if the laser is tuned below the dressed state $|-\rangle$. This friction force corresponds to the plots shown in [6]. Moreover, for $|\Delta_a| \gg g^2/\kappa$, it reduces to the one in [3,4], $(\Delta_-, \Gamma_-) \rightarrow (\Delta_c, \kappa)$.

We here recall and interpret a reported anomaly [6]. If one looks at Eq. (4b), and sets $\Delta_c = 0$ (and $\boldsymbol{k}_i \cdot \boldsymbol{v} = 0$), then, to first order in $\boldsymbol{v}$, one finds a term $-(g^2/\kappa^2)\boldsymbol{k}_L \cdot \boldsymbol{v}$. This term is anomalous because it is opposed to the usual Doppler shift $\boldsymbol{k}_L \cdot \boldsymbol{v}$. The origin of this, however, is very clear from our Eq. (4b). Indeed, the terms in g_i^2 ($i = 1, 2$) are familiar light shifts. Those depend on the velocity because the cavity receives photons of frequency $\omega_L - (\boldsymbol{k}_L - \boldsymbol{k}_i) \cdot \boldsymbol{v}$ and not ω_L. This means that the light shifts are Doppler shifted, and the first order in $\boldsymbol{v}$ gives such an (abnormal) correction. From a broader view, as a function of the mismatch $\delta = \Delta_c + (\boldsymbol{k}_L - \boldsymbol{k}_i) \cdot \boldsymbol{v}$, a light shift is a dispersive curve $-\delta/(\delta^2 + \kappa^2)$, whose slope is negative for $|\delta| < \kappa$. In this way, one also sees why the anomaly exists only within the range $|\Delta_c| < \kappa$, the slope at $v = 0$ being then strictly negative and extremum for $\Delta_c = 0$, yielding $-(g^2/\kappa^2)\boldsymbol{k}_L \cdot \boldsymbol{v}$. That anomaly is thus a first order velocity Doppler shift of the light shift induced by the cavity field.

In addition, we mention another (intriguing) effect. We know that an atom copropagating with laser photons, i.e. $\boldsymbol{k}_L \cdot \boldsymbol{v} > 0$, sees them Doppler shifted to the red. Thus, if the laser frequency is already below resonance $\omega_L < \omega_{\mathrm{eg}}$, the force becomes weaker as the atom accelerates. But the peak on the right side of Fig. 2(a) indicates the contrary, i.e., the force is enhanced when the atom copropagates with the laser photons $\boldsymbol{k}_L \cdot \boldsymbol{v} > 0$ despite these being red detuned $\omega_L < \omega_{\mathrm{eg}}$. The reason the force is increased is that the photons Doppler shifted further to the red now become resonant with the dressed state $|-\rangle$, i.e. $\omega_L - \boldsymbol{k}_L \cdot \boldsymbol{v}_- = \omega_- < \omega_L$, see Fig. 2(b). This effect can occur for $\Delta_c \gg \kappa$, as in Fig. 2(a), and is hence distinct from the anomaly in [6].

To summarize, we have discussed the potential of optical cavities for capturing and cooling atoms having arbitrary velocities. For low atomic saturation, the addition of a cavity leads to a rate of photon scattering with two velocity-dependent peaks. The two peaks are due to the resonances of the combined atom-cavity system, and generalize the Lorentz peak of Doppler cooling. They are visible in both the light scattered into the cavity and the fluorescence photons. The shape of the resonances strongly depends upon the cavity geometry and, hence, should allow one to enlarge the velocity capture range while maintaining the final temperature close to the standard Doppler limit. Lasers with polarization gradients should further lower the temperature, with now the advantage of a large velocity capture range.

I warmly thank G. Rempe, S. Nußmann, T. Volz, S. C. Webster, T. Puppe, P. W. H. Pinkse, J. Bochmann, A. Kuhn, D. M. Bauer, N. Syassen, T. Wilk, M. Hijlkema, and B. Weber for enlightening discussions and support.

[1] C. Cohen-Tannoudji, in *Fundamental Systems in Quantum Optics, Les Houches, Session LIII, 1990*, edited by J. Dalibard, J. M. Raimond, and J. Zinn-Justin (Elsevier Science, North-Holland, 1992), p. 1.
[2] M. Partlow, X. Miao, J. Bochmann, M. Cashen, and H. Metcalf, Phys. Rev. Lett. **93**, 213004 (2004).
[3] V. Vuletić and S. Chu, Phys. Rev. Lett. **84**, 3787 (2000).
[4] V. Vuletić, H. W. Chan, and A. T. Black, Phys. Rev. A **64**, 033405 (2001).
[5] P. Domokos and H. Ritsch, J. Opt. Soc. Am. B **20**, 1098 (2003).
[6] P. Domokos, A. Vukics, and H. Ritsch, Phys. Rev. Lett. **92**, 103601 (2004).
[7] S. Zippilli and G. Morigi, Phys. Rev. Lett. **95**, 143001 (2005).
[8] H. W. Chan, A. T. Black, and V. Vuletić, Phys. Rev. Lett. **90**, 063003 (2003).
[9] D. Kruse, M. Ruder, J. Benhelm, C. von Cube, C. Zimmermann, P. W. Courteille, T. Elsässer, B. Nagorny, and A. Hemmerich, Phys. Rev. A **67**, 051802(R) (2003).
[10] J. McKeever, J. R. Buck, A. D. Boozer, A. Kuzmich, H.-C. Nägerl, D. M. Stamper-Kurn, and H. J. Kimble, Phys. Rev. Lett. **90**, 133602 (2003).
[11] P. Maunz, T. Puppe, I. Schuster, N. Syassen, P. W. H. Pinkse, and G. Rempe, Nature (London) **428**, 50 (2004).
[12] S. Nußmann, K. Murr, M. Hijlkema, B. Weber, A. Kuhn, and G. Rempe, Nature Phys. **1**, 122 (2005).
[13] P. Maunz, T. Puppe, I. Schuster, N. Syassen, P. W. H. Pinkse, and G. Rempe, Phys. Rev. Lett. **94**, 033002 (2005).
[14] A. Boca, R. Miller, K. M. Birnbaum, A. D. Boozer, J. McKeever, and H. J. Kimble, Phys. Rev. Lett. **93**, 233603 (2004).
[15] K. Murr, P. Maunz, P. W. H. Pinkse, T. Puppe, I. Schuster, D. Vitali, and G. Rempe, quant-ph/0512001.
[16] W. Ren, J. D. Cresser, and H. J. Carmichael, Phys. Rev. A **46**, 7162 (1992).

RAPID COMMUNICATIONS

PHYSICAL REVIEW A **73**, 061402(R) (2006)

Water vapor at a translational temperature of 1 K

T. Rieger, T. Junglen, S. A. Rangwala,* G. Rempe, and P. W. H. Pinkse
Max-Planck-Institut für Quantenoptik, Hans-Kopfermann-Strasse 1, D-85748 Garching, Germany

J. Bulthuis
Department of Physical Chemistry and Laser Centre, Vrije Universiteit, De Boelelaan 1083, 1081 HV Amsterdam, The Netherlands
(Received 8 December 2005; revised manuscript received 3 March 2006; published 29 June 2006)

We report the creation of a confined slow beam of heavy-water (D_2O) molecules with a translational temperature around 1 K. This is achieved by filtering slow D_2O from a thermal ensemble with inhomogeneous static electric fields exploiting the quadratic Stark shift of D_2O. All previous demonstrations of electric-field manipulation of cold dipolar molecules rely on a predominantly linear Stark shift. Further, on the basis of elementary molecular properties and our filtering technique we argue that our D_2O beam contains molecules in only a few rovibrational states.

DOI: 10.1103/PhysRevA.73.061402 PACS number(s): 33.80.Ps, 33.55.Be, 39.10.+j

Cold dilute molecular systems are rapidly emerging as a front-line area at the interface of quantum optics and condensed matter physics [1]. An increasing subset of this activity centers around the creation of cold dilute gases of molecules possessing electric dipole moments. These in particular, owing to their long-range anisotropic interaction, hold the promise of novel physics, where two- and many-body quantum properties can be systematically studied. Cold dilute gases of dipolar molecules can be produced by forging a tight bond between two chemically distinct species of laser-cooled atoms, e.g., RbCs [2]. Alternatively, cold dilute gas ensembles can be created by buffer-gas loading [3] or electric-field manipulation of naturally occurring molecules like ND_3 [4,5] and H_2CO [6], metastables like CO [7], or radicals like YbF [8], OH [9], and NH [10]. So far all the cold molecules made available with electric-field-based methods have a Stark effect (in their relevant states) which is predominantly linear in the important range up to 150 kV/cm.

Here we report the creation of a slow beam of heavy-water (D_2O) molecules, which experience a quadratic Stark effect. The cold D_2O molecules are filtered from a room-temperature thermal gas [6] and have a translational temperature around 1 K. Because the Stark shifts are quadratic in the electric field, it follows that forces exerted by inhomogeneous electric fields are relatively small for D_2O compared to molecules with similar dipole moments but with linear Stark shifts. It is therefore by no means obvious that significant quantities of slow D_2O molecules can be produced by means of electric-field-based methods. Our experimental result therefore underlines the versatility of the velocity-filtering method. It is an enabling step toward future trapping of molecules for which the ratio of elastic to inelastic collisions is expected to be more favorable than for molecules with linear Stark shifts [11]. An additional advantage of the quadratically Stark-shifted molecules like D_2O is the possibility to perform precise spectroscopic measurements insensitive to stray electric fields, to the first order. Moreover, water is abundant in interstellar space at low densities and temperatures from a few kelvin upward, playing an important role in the chemistry of molecular clouds [12]. The conditions in these clouds are remarkably close to those achieved in our experiment, opening up the possibility to investigate in the laboratory chemical reactions under conditions found in space.

This Rapid Communication is structured as follows. First we discuss general features of Stark shifts of molecular states with particular reference to D_2O. We then present our experimental work with D_2O. This is followed by arguing from first principles that the resulting beam of D_2O is dominated by only four rotational states, despite starting with a thermal source of molecules at 300 K.

Several techniques have recently been developed to manipulate molecules [1] with electric fields. All of these exploit the Stark effect to exert a force on the molecules. In contrast to atoms, molecules can have a permanent electric dipole moment. Such molecules have much larger Stark shifts than nonpolar molecules. However, as described below, a large dipole moment alone is not enough to have a strong Stark effect. The direction and magnitude of the force exerted on the molecule in an inhomogeneous electric field depend on the details of the molecular rotational state. Assuming the Stark shift to be a monotonic function of the electric field, the molecule can be in either low-field-seeking (LFS) or high-field-seeking states, depending on the sign of the Stark shift.

The condition for having a linear Stark effect is that the component of the dipole moment $\vec{d}$ along a space-fixed direction, we can choose $\vec{z}$, is nonvanishing [i.e. $\langle \vec{d}\cdot\vec{z}\rangle \neq 0$]. Strictly speaking this requires a finite electric field, but it can be arbitrarily low. The linear Stark shift is typically found in symmetric-top molecules and is proportional to $|\vec{d}|KM$, with K and M representing the projection of the total angular momentum $\vec{J}$ on the molecular symmetry axis and on the z axis, respectively. Of course, no first-order Stark effect occurs if either M or K—or both—is zero. If the degeneracy in zero field is lifted, e.g., by fine-structure splitting, inversion doubling, nuclear quadrupole interaction in a symmetric-top molecule, or Λ doubling in linear molecules, the Stark splitting will no longer be linear in the limit of zero field. How-

*Present address: Raman Research Institute, C. V. Raman Avenue, Sadashivanagar, Bangalore 560080, India.

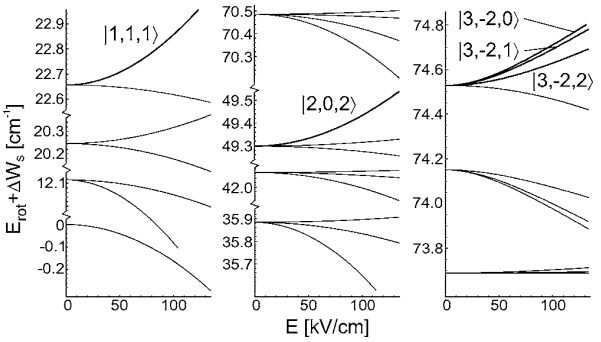

FIG. 1. The lowest rotational energies of D_2O as a function of the applied electric field E. The five most abundant states $|J,\tau,M\rangle$ in the guided beam are indicated. The Stark shifts are obtained by numerically diagonalizing the Stark Hamiltonian ($J=0,\ldots,12$), following Ref. [13].

ever, often those interactions are small enough as to lead to a nearly linear Stark splitting in the applied electric-field range.

In general, the linear Stark effect condition $\langle\vec{d}\cdot\vec{z}\rangle\neq 0$ is not satisfied in asymmetric-top molecules. Under certain conditions, however, polar asymmetric molecules can also exhibit (nearly) linear Stark shifts. If the asymmetry is weak, the states that correspond to $K\neq 0$ in the prolate- or oblate-top limit will always be close to being degenerate. Those states show nearly linear Stark shifts if they are coupled by the Stark interaction. This is the case if the dipole is along the a axis in the prolate limit, or along the c axis in the oblate limit, where we follow the convention to label the axis with the smallest moment of inertia and hence the largest rotational constant with a, the intermediate axis b, and the axis with the largest moment of inertia c. An example is the nearly symmetric- (prolate-)top molecule H_2CO.

True asymmetric-top molecules in general have quadratic Stark shifts. Exceptions can occur for some states, if the dipole is oriented along the axis of largest or smallest moment of inertia. For molecules with their dipole oriented along the b axis, we found no exceptions: all rotational states have a nonlinear Stark shift. Water, both H_2O and D_2O, presents such a case and a few levels of D_2O are depicted in Fig. 1. The quadratic behavior is obvious; only for the highest most abundant states, the $|J=3,\tau,M\rangle$ states (where τ is a pseudo quantum number labeling the state), is a deviation found. Moreover, the large rotational constants [14] for D_2O, $A=15.394\ \mathrm{cm}^{-1}$, $B=7.2630\ \mathrm{cm}^{-1}$, $C=4.8520\ \mathrm{cm}^{-1}$, imply large rotational level spacings. Avoided level crossings are neither expected nor found, and second-order perturbation theory is a reasonable approximation for the Stark shift computation of H_2O and D_2O. Moreover, since the contribution to the perturbation from each coupled pair of states is inversely proportional to the energy gap between the pair, the shift will be proportional to the density of (rotational) states, and therefore very small for the sparse rotational spectrum of D_2O and H_2O. Our choice of working with D_2O as opposed to H_2O has partly to do with the larger Stark shifts of D_2O because of its smaller rotational constants. The treatment of the general case of an asymmetric molecule, where the dipole is not necessarily along one of the principal axes, is, of course, more involved.

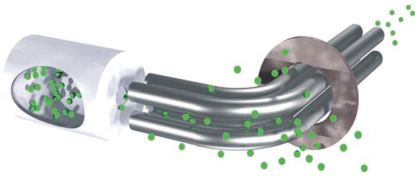

FIG. 2. (Color online) Schematic of the experiment. On the left is the effusive source, which injects thermal D_2O molecules into the four-wire guide. Neighboring electrodes have opposite polarity, creating a quadrupolar electric field. Molecules that are slow enough are guided through the first and second (not shown) 90° bends and are finally detected by a mass spectrometer.

Our apparatus [4] is depicted in Fig. 2. It consists of a room-temperature effusive thermal source, which injects D_2O molecules directly between four 50-cm-long electrodes set up in a quadrupole arrangement, with neighboring electrodes having opposite polarities. The guide has two 90° bends with a radius of curvature of 25 mm. The quadrupolar electric field defines a two-dimensional potential well. This well has a depth that depends on the internal molecular state, e.g., for the $|J,\tau,M\rangle=|1,1,1\rangle$ state with a positive Stark shift of $0.20\ \mathrm{cm}^{-1}$ at 100 kV/cm, the depth amounts to 0.29 K. Molecules with transverse kinetic energy exceeding the potential depth escape the guide. In the bends the longitudinally fast molecules escape while the slow ones are kept due to the action of the centripetal force. These are guided through two differential pumping regions into an ultrahigh vacuum chamber for mass-spectrometric detection at the end of the electrodes. Heavy water is convenient for this purpose, as the background at its mass is virtually zero. The longitudinal velocity distribution of the guided D_2O beam was determined by a time-of-flight method [6] at an escape field E of 115 kV/cm. We found a most-probable velocity of 24 m/s in the laboratory frame, corresponding to a longitudinal temperature of $\approx$1.4 K. The transverse temperature is expected to be on the order of 0.1 K, as the guide presents a smaller transverse velocity cutoff value than the corresponding longitudinal velocity cutoff.

The flux dependence on the escape field E and hence on the applied electrode voltage V is characteristic of the nature of the guided molecules' Stark shift. This can be seen as follows. Let x,y be directions orthogonal to and z be parallel to the quadrupolar axis. Let $f_{v_{x,y,z}}$ be functions proportional to the flux crossing the planes of unit area perpendicular to the x,y,z axes, respectively [15]. Then $f_{v_{x,y}}\propto\exp(-v_{x,y}^2/\alpha^2)$ is bidirectional and $f_{v_z}\propto v_z\exp(-v_z^2/\alpha^2)$ is unidirectional along the positive z axis. Here, $\alpha=\sqrt{2k_BT/m}$, k_B the Boltzmann constant, T the temperature of the reservoir the beam originates from, and m the molecular mass. Hence the total guided flux $\Phi\propto\int_0^{v_{x,\max}}dv_x\int_0^{v_{y,\max}}dv_y\int_0^{v_{z,\max}}dv_z f_{v_x}f_{v_y}f_{v_z}$, where $v_{x,y,z,\max}$ are the maximal guided velocities in each direction. As $\alpha\gg v_{x,y,z,\max}$, $\Phi\propto v_{x,\max}v_{y,\max}v_{z,\max}^2$. The maximum kinetic energy $U_{k,\max}$ is given by the escape energy of the guide, i.e., the Stark shift in E, which is proportional to the applied electrode voltage V. Hence for molecules with a lin-

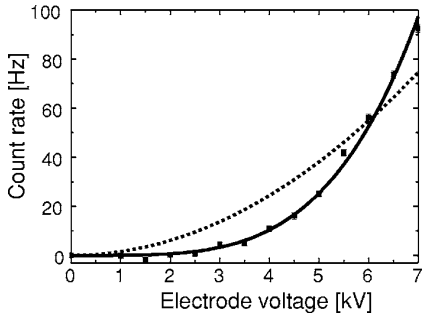

FIG. 3. Detector signal versus the electrode voltage V. The data follow a quartic law in V, as illustrated by the V^4 fit (solid line). The dotted line shows a V^2 fit attempt.

ear Stark shift, $\Phi \propto U_k^2 \propto V^2$. For molecules with a quadratic Stark shift, $U_k \propto V^2$, and hence $\Phi \propto U_k^2 \propto V^4$.

Our detector, a quadrupole mass spectrometer, converts molecules to ions by electron-impact ionization. The ions are then mass selected. Measurement on various molecules with a linear Stark shift indicate that the signal is to a good approximation proportional to the guided flux [4,6]. Scaling (for detector counting efficiencies, angular divergence of the beam exiting the guide) and corrections (velocity-dependent detection, branching ratios of ionization) are needed to convert our measured count rates (plotted in Fig. 3) to the absolute flux $\approx 7 \times 10^7$ s^{-1} at $V=7$ kV, corresponding to an electric field depth of the guide of $E=134$ kV/cm. The error margin of the flux is estimated to be of the order of a factor 2. The quartic dependence on E is clearly visible in Fig. 3 and proves the quadratic Stark shift of the guided molecules. Indeed, with the same apparatus it has been observed [4,6] that for H_2CO and ND_3 (linear Stark molecules), the flux depends quadratically on V.

As our slow beam originates from a room-temperature source, many rotational states are populated. This is illustrated in Fig. 4, where the Stark shifts of D_2O in a field of 100 kV/cm have been plotted as a function of the zero-field

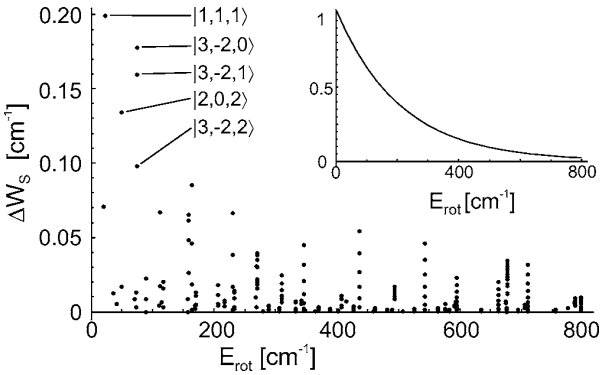

FIG. 4. Stark shifts ΔW_S in an electric field of 100 kV/cm of LFS rotational states of D_2O in its vibrational and electronic ground state, as a function of the zero-field rotational energy E_{rot}. The inset shows the Boltzmann factor at $T=300$ K. The five most Stark-rotational energy. The Stark shifts are obtained by numerically diagonalizing the Stark Hamiltonian for a rigid asymmetric rotor, following the procedure of Ref. [13]. It is known that the rigid-rotor assumption is only a coarse approximation when estimating the absolute energies of D_2O states. In the present case, however, the approximation is expected to be good if one is only interested in the Stark shifts and not in the absolute energies, because the Stark shifts are caused by the coupling of adjacent states that do not differ much in their sets of rotational quantum numbers, leading to relatively small sensitivity to the centrifugal distortion. We have also neglected hyperfine couplings, which is completely justified in the range of field strengths used in our experiments. As input for the Stark shift calculations we took the rotational constants and the dipole moment $\mu=1.87$ D, which is directed along the b axis [14]. Note that as a general trend, the Stark shifts decrease with rotational energy.

As discussed earlier the room-temperature rotational spectrum of D_2O is very sparse. The populations in the thermal gas in the effusive source can be estimated by weighting all thermally populated states with the Boltzmann factor, their orientational (M) degeneracy and the spin-statistical weight [16]. Further, only very few of these levels have large enough Stark shifts to be guided. This selection is much more pronounced for molecules with a quadratic Stark shift than for molecules with a linear Stark shift. The intuitive reason is that for molecules with a quadratic Stark shift, the electric field must first orient the dipole in space, which is harder for faster rotating molecules. Indeed, for these molecules the Stark shift [14] is approximately proportional to $1/(J+1)$. Hence, the (maximum) Stark shifts decreases with J, as can be seen for D_2O in Fig. 4. This should be compared with the dependence of the Stark shift on J of molecules with a linear Stark shift. For the generic example of a symmetric top, this shift is proportional to $|\vec{d}|KME/[J(J+1)]$ [14]. As $(K,M) \in \{-J,\ldots,0,\ldots,J\}$, the Stark shift of the maximum (K,M) for molecules with a linear Stark shift will not decrease with J. In fact, knowing that the flux of D_2O molecules is proportional to the square of the Stark shift, and assuming that this dependence holds for each state, the four most populated states contribute more than 70% of our guided flux. The partial contributions, zero-field energy, and Stark shifts of the five most abundant states are summarized in Table I. One should note that the beam purity [17] is independent of voltage changes as long as all the states are

TABLE I. The most dominant rotational states $|J,\tau,M\rangle$ of D_2O with their partial contribution to the flux, their zero-field energy, and the Stark shift ΔW_S at $E=100$ kV/cm.

State	Contribution (%)	E_{rot} (cm^{-1})	ΔW_S (cm^{-1})
$\|3,-2,1\rangle$	21	74.53	0.16
$\|1,1,1\rangle$	21	22.66	0.20
$\|2,0,2\rangle$	17	49.30	0.13
$\|3,-2,0\rangle$	13	74.53	0.18

quadratic in nature.

In conclusion, we have demonstrated the effective Stark manipulation of a polar molecule with quadratic Stark shifts over the range of applied fields of 0–135 kV/cm. This experimentally shows the feasibility of the velocity-filtering method for quadratically Stark-shifted molecular states. Using this method we have created water vapor (D_2O) at a translational temperature of $\approx$1 K. Its quadratic Stark effect combined with a large rotational spacing make D_2O a promising molecule for electric trapping [18] and even evaporative cooling.

We acknowledge financial support by the Deutsche Forschungsgemeinschaft (SPP 1116).

[1] See, e.g., Eur. Phys. J. D **31**, 149 (2004), special issue on ultracold polar molecules.
[2] J. M. Sage, S. Sainis, T. Bergeman, and D. DeMille, Phys. Rev. Lett. **94**, 203001 (2005).
[3] J. D. Weinstein, R. deCarvalho, T. Guillet, B. Friedrich, and J. M. Doyle, Nature (London) **395**, 148 (1998).
[4] T. Junglen, T. Rieger, S. A. Rangwala, P. W. H. Pinkse, and G. Rempe, Eur. Phys. J. D **31**, 365 (2004).
[5] H. L. Bethlem, G. Berden, F. M. H. Crompvoets, R. T. Jongma, A. J. A. van Roij, and G. Meijer, Nature (London) **406**, 491 (2000).
[6] S. A. Rangwala, T. Junglen, T. Rieger, P. W. H. Pinkse, and G. Rempe, Phys. Rev. A **67**, 043406 (2003).
[7] H. L. Bethlem, G. Berden, and G. Meijer, Phys. Rev. Lett. **83**, 1558 (1999).
[8] M. R. Tarbutt, H. L. Bethlem, J. J. Hudson, V. L. Ryabov, V. A. Ryzhov, B. E. Sauer, G. Meijer, and E. A. Hinds, Phys. Rev. Lett. **92**, 173002 (2004).
[9] J. R. Bochinski, E. R. Hudson, H. J. Lewandowski, G. Meijer, and J. Ye, Phys. Rev. Lett. **91**, 243001 (2003).
[10] S. Y. T. van de Meerakker, R. T. Jongma, H. L. Bethlem, and G. Meijer, Phys. Rev. A **64**, 041401(R) (2001).
[11] J. L. Bohn, Phys. Rev. A **63**, 052714 (2001).
[12] M. Spaans and E. van Dishoeck, Astrophys. J. **548**, L217 (2001).
[13] T. D. Hain, R. M. Moision, and T. J. Curtiss, J. Chem. Phys. **111**, 6797 (1999).
[14] C. H. Townes and A. L. Schawlow, *Microwave Spectroscopy*, (Dover Publications, New York, 1975).
[15] P. W. H. Pinkse, T. Junglen, T. Rieger, S. A. Rangwala, and G. Rempe, in *Interactions in Ultracold Gases*, edited by M. Weidemüller and C. Zimmermann (Wiley-VCH, Weinheim, 2003).
[16] G. Herzberg, *Molecular Spectra and Molecular Structure, I and III* (Van Nostrand Reinhold, New York, 1966).
[17] Note that the guided beam is not in internal equilibrium. The average rotational energy of the beam corresponds to that of a thermal gas of 81 K. The purity, however, is equivalent to that of a thermal gas of 23 K, as calculated from the entropy of the internal distribution.
[18] T. Rieger, T. Junglen, S. A. Rangwala, P. W. H. Pinkse, and G. Rempe, Phys. Rev. Lett. **95**, 173002 (2005).

Appl. Phys. B (2006)
DOI: 10.1007/s00340-006-2274-2

Applied Physics B
Lasers and Optics

Rapid communication

A. FRIEDENAUER[1,✉,*]
F. MARKERT[1,*,**]
H. SCHMITZ[1]
L. PETERSEN[1]
S. KAHRA[1]
M. HERRMANN[1]
TH. UDEM[1,2]
T.W. HÄNSCH[1,2]
T. SCHÄTZ[1]

High power all solid state laser system near 280 nm

[1] Max-Planck-Institut für Quantenoptik, Hans-Kopfermann-Str. 1, 85748 Garching, Germany
[2] Ludwigs-Maximilians-Universität München, Schellingstr. 4, 80799 München, Germany

Received: 20 March 2006

ABSTRACT We present a stable high power all solid state laser system emitting 1-W of continuous wave laser radiation at a wavelength of 559 nm or 275 mW near 280 nm. The system consists of a commercial 2-W fiber laser with a line width of less than 200 kHz at 1118 nm and two home-built subsequent second harmonic generation external ring cavities using LBO and BBO crystals, respectively. The system is designed to act as a detection and cooling laser for trapped Mg^+ ions.

PACS 03.67.Lx; 32.80.Qk; 42.60.By; 42.79.Nv

1 Introduction

The fact that the laser apparatus for experiments with trapped light ions (Be^+, Mg^+) is very complex and expensive is one of the main obstacles for scaling up to larger multi-beam experiments. Due to the development of high power fiber laser systems with superb beam quality and low maintenance combined with efficient frequency quadruplers, this kind of experiment comes closer into consideration as these systems cost a fraction of the formerly used dye and related pump lasers. The laser source we present in this paper is actually used to detect and cool trapped Mg^+ ions driving the transitions from the ground state $3S_{1/2}$ to the $3P_{1/2}$ or $3P_{3/2}$ levels at approximately 280 nm.

2 Laser system

Acting as fundamental beam source, we use a commercially available 2-W ytterbium fiber laser at 1118 nm with a line width smaller than 200 kHz built by Koheras. The fiber laser consists of a fiber master oscillator and a power amplifier pigtailed by a non-polarization-maintaining fiber with an FC/APC connector. The laser is tunable both by temperature for slow tuning and by a piezo-controlled optical path length of the fiber allowing for a total scan range of 80 GHz with a bandwidth of 20 kHz at 1118 nm. We double the frequency of the laser output in the infrared (IR) twice by two subsequent second harmonic generation (SHG) cavities. We use 10 mW of the second-harmonic beam at 559 nm to implement polarization spectroscopy [1, 2] to stabilize the laser frequency to an appropriate iodine transition (R(53)28-3 at 559.271 nm) using the piezo of the laser. In addition to the power of 2 W at the wavelength of 1118 nm, the fiber laser emits 1.2 W of broadband amplified spontaneous emission (ASE) peaked between 1060 nm and 1100 nm. After switching on the power amplifier the laser undergoes polarization drifts which fall off exponentially in time. After about two hours the output polarization reaches a steady state provided that the non-polarization-maintaining fiber is fixed in position. We control the polarization of the beam coming from the single-mode fiber by quarter- and half-wave plates. We reduce the amount of retroreflected light into the laser by an optical isolator, which is designed for a wavelength of 1064 nm and transmits approximately 90% of the incident power at 1118 nm (isolation ≈ 30 dB) and half of the unpolarized ASE power, ending up with 1.8 W of pump power for the first SHG cavity. Since the ASE is not resonant with the cavity mode, it is filtered out by the optical resonator. We retrieve the incoupling efficiency by subtracting the ASE power from the total power. We mode match the pump beam into the first SHG cavity using two lenses, one of these being a fiber collimator with a variable distance between the end of the fiber and the lens.

3 SHG cavities

Frequency-doubling efficiencies up to 85% have been reported [3, 4] using type II phase matching in KTP crystals at wavelengths of 1060 or 1080 nm. Unfortunately, there is no possible non-critical type II phase match (NCPM) in KTP at 1118 nm [7]. Potentially usable crystals for doubling 1118 nm include potassium niobate (KNB, effective nonlinearity $d_{\text{eff}} = -12.1$ pm/V), lithium niobate (LNB, $d_{\text{eff}} = -4.4$ pm/V) or lithium triborate (LBO, $d_{\text{eff}} = 0.84$ pm/V). Although the niobate crystals have higher effective nonlinearities, the main advantage of LBO is its very high optical quality, high damage threshold and its moder-

✉ Fax: +49-89-32905-200, E-mail: axel.friedenauer@mpq.mpg.de
*Both A. Friedenauer and F. Markert contributed to this work equal parts.
**Present address*: Johannes-Gutenberg-Universität Mainz, Staudinger Weg 7, 55128 Mainz, Germany

ate NCPM temperature of 89 °C compared to 351 °C for KNB and 219 °C for MgO:LNB, which would be suitable for high-power applications.

For the first SHG cavity we use non-critically phase-matched, type I, α-cut lithium triborate (LBO) which is antireflective coated both for the fundamental and for the harmonic waves. The cutting angles of the crystal are $\theta = 90°$, $\varphi = 0°$; therefore, we obtain a round non-astigmatic green beam out of the cavity which can be coupled into the next cavity via two spherical lenses. The 18-mm-long crystal is placed inside an oven temperature controlled to within 20 mK. Theory predicts a phase-matching temperature of 89 °C, but we found optimum harmonic generation at 94 °C that might be due to improper heat contact between the copper oven and the crystal despite a thin indium foil in between. The crystal is placed in the smaller focus of a folded ring cavity (see Fig. 1). The cavity has a small folding angle of 10° (full angle between incident and reflected beams) at both focusing mirrors to minimize astigmatism. The total length of the ring cavity is 400 mm to ensure a large free spectral range (FSR = 750 MHz) and therefore a large resonance width of the longitudinal cavity modes.

As an input coupler we use a plane mirror with a reflectivity of $R = 97.5\%$ for the fundamental (M1, antireflective (AR) coated on the outside of the cavity) to impedance match the losses inside the cavity. The second mirror, highly reflective (M2, $R > 99.98\%$), is mounted on a small stacked piezo with high resonance frequency (Thorlabs model AE020304D04, $\nu_{\mathrm{res}} \approx 18$ kHz loaded). We glued the piezo to a disk made of lead to absorb vibrations and reduce the resonance frequency of the mirror mount. The dimension of this mirror is very small, allowing for a high servo bandwidth ($3 \times 3 \times 2\,\mathrm{mm}^3$). Furthermore, two curved mirrors of focal length $f = 25$ mm are used, one of them highly reflective at the fundamental (M3, $R > 99.98\%$), the other acting as an output coupler highly reflective at the fundamental (M4, $R > 99.9\%$) and highly transmissive at the harmonic wavelength ($T > 95\%$). The output coupler is shaped as a 'zero lens' and AR coated for the harmonic on the convex side. We modeled the cavity including linear and conversion losses of the crystal and reflection losses of the mirrors to determine the optimum crystal length of 18 mm. We derived the optimum focus inside the crystal from calculations following Boyd–Kleinman theory [5] to be 27.3-μm beam waist ($1/e^2$ of the intensity) and adjusted the distance between the curved mirrors to match this value at the plateau of the stability region (geometric distance between focusing mirrors M3 and M4: $d = 62$ mm). For stabilizing the length of the cavity we use the polarization-locking scheme of [6]. We obtain 1 W of green output power at 559 nm. For long-term operation, one can increase the stability of the system by further tilting the input polarization with respect to the crystal axis, sacrificing some output power for a stronger error signal. In this way we obtain a stable output power of 950 mW, corresponding to a conversion efficiency of the LBO resonator of larger than 52.7%. We stress that we give the available output power relative to the laser power in front of the cavity rather than correcting for coupling efficiency, Fresnel losses and output coupler loss.

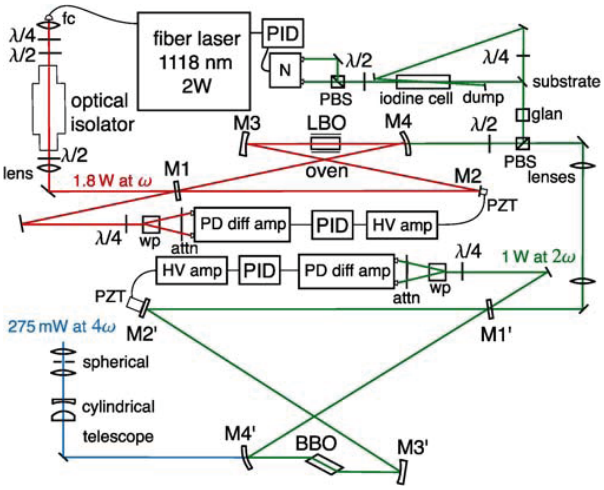

FIGURE 1 Optical setup of the laser system. The light coming from the fiber laser is collimated by the fiber collimator (fc) and passes the optical isolator after polarization adjustment by quarter- and half-wave plates (λ/4 and λ/2). After passing another half-wave plate the beam is mode matched (lens) into the LBO cavity consisting of mirrors M1, M2, M3 and M4. The light reflected at M1 passes a quarter-wave plate and a Wollaston prism (wp), is attenuated (attn) and falls on a photodiode (PD) differential amplifier. That signal goes to a proportional-integral-derivative (PID) servo and after amplification (HV amp) is fed to the piezo (PZT) on which the mirror M2 is mounted. The second-harmonic beam generated in the LBO crystal leaves the cavity via the output coupler M4 and 10 mW are separated from the beam for the iodine lock using a half-wave plate and a polarizing beam splitter (PBS). With this beam we implement polarization spectroscopy [2] using a Glan laser polarizer (glan) and a New Focus Nirvana photodetector (N). The larger part traversing the PBS is mode matched in the BBO cavity consisting of mirrors M1', M2', M3' and M4' using two mode-matching lenses. The generation of the error signal is identical to the first cavity. The ultraviolet beam generated in the BBO crystal leaves the cavity via M4' and is projected into a Gaussian TEM00 mode and collimated with the help of cylindrical and spherical telescopes. The whole setup fits on a breadboard measuring $90 \times 30\,\mathrm{cm}^2$ and is moveable

The output of the first cavity is coupled into an astigmatism-compensated second cavity based on a Brewster-cut BBO crystal, which we heat to approximately 50 °C in order to prevent water from condensing on the hygroscopic, polished surfaces of the crystal. The BBO crystal ($4 \times 4 \times 10\,\mathrm{mm}^3$) is mounted on a rotational and a linear translation stage which preserves distances and angles between the crystal and the focusing mirrors. Again, calculations following Boyd–Kleinman theory are carried out leading to an ideal focus of 19.4 μm. Mode matching the incoupling beam to the mode of the second SHG cavity is performed by two lenses mounted on 3D translational stages to ease realigning. The layout of the second cavity is similar to the first, differing only in the reflectivities of the mirrors and the folding angle of the cavity at both mirrors (full angle 27.4°) to compensate for the astigmatism caused by the Brewster-cut BBO crystal. We implemented this cavity using mirrors (M2', M3') with $R > 99.93\%$ and the

	LBO cavity	BBO cavity
Highly reflective (HR) mirrors fundamental	99.98%	99.93%
Output coupler HR fund.	99.9%	99.8%
Input coupler fund.	97.5%	98.4%
Distance between focusing mirrors	62 mm	59.4 mm
Total cavity length	400 mm	470 mm
Full folding angle	10°	27.4°
Incoupling power	1.80 W	0.95 W
Output power	0.95 W	0.275 W
Doubling efficiency	52.7%	28.9%

TABLE 1 Mirror reflectivities, measures and technical data of the SHG cavities

output coupler (M4') $R > 99.8\%$ at 560 nm and $T > 94\%$ at 280 nm. We project 95% of the astigmatic beam exiting the second cavity into a Gaussian TEM00 mode using a cylindrical telescope and collimate the beam using a spherical cleaning telescope. We end up with 275 mW of ultraviolet output power. Measures, mirror reflectivities and efficiencies of both cavities are summarized in Table 1.

4 Resonances

We discovered a 14-GHz-broad frequency region between 1118.409 nm and 1118.339 nm where we observe the following: when scanning the cavity length in one direction the transmission fringes are broadened while by scanning it backwards the fringes are narrowed. We were not able to lock the cavity in this frequency domain. We reproduced this phenomenon using several lasers, cavities and crystals. We note that all crystals were bought from the same crystal manufacturer (Crystals of Siberia). This frequency domain (quadrupled to the ultraviolet) does not overlap with the resonant transitions of Mg^+ isotopes from the ground state $3S_{1/2}$ to the $3P_{1/2}$ or $3P_{3/2}$ levels. But, it imposes restrictions for two-photon stimulated Raman transitions via detuned levels. It seems as if the index of refraction of the crystal changes with light intensity in the crystal. Previously, resonances of OH groups in LBO crystals have been found [8] with a comparable width however at different wavelengths than observed here.

5 Stability

We observe fluctuations in the ultraviolet (UV) output power within 2% deviation from the mean value. Furthermore, on microsecond time scales we notice regular drops of the UV output power smaller than 4%. Drops larger than 7% appear less than once a minute. In addition, we discover a sensitivity to long-term temperature drifts of the environment which resulted in oscillations as large as 10% of the output power as the temperature changed by 2 K, but we were able to reduce these drifts to 5% by proper thermal isolation of the crystal oven. The other problem is that the output polarization of the laser changes as the heat sink of the power amplifier of the fiber laser changes in temperature. Thus, the beam which is no longer parallel polarized with respect to the input polarizer of the optical isolator is not completely transmitted through the optical isolator. One has to manually adjust the output polarization of the fiber with the help of the quarter- and the half-wave plates to retrieve optimum transmission through the optical isolator. One solution to this issue could be an active stabilization of the temperature of the heat sink of the laser with the help of a Peltier element.

6 Conclusion

In summary, we presented a laser system consisting of a commercial ytterbium fiber laser and two subsequent external second harmonic generation ring cavities with an output power of 275 mW near 280 nm. This corresponds to an overall conversion efficiency of 15.2%.

ACKNOWLEDGEMENTS We thank Ove Poulsen, Jim Bergquist and Dietrich Leibfried for their genuine input and triggering ideas. We gratefully acknowledge financial support by the Deutsche Forschungsgemeinschaft and the Max-Planck-Institut für Quantenoptik.

REFERENCES

1 C. Wieman, T.W. Hänsch, Phys. Rev. Lett. **36**, 1170 (1976)
2 C.P. Pearman, C.S. Adams, S.G. Cox, P.F. Griffin, D.A. Smith, I.G. Hughes, J. Phys. B **35**, 5141 (2002)
3 R. Paschotta, K. Fiedler, P. Kürz, R. Henking, S. Schiller, J. Mlynek, Opt. Lett. **19**, 1325 (1994)
4 Z.Y. Ou, S.F. Pereira, E.S. Polzik, H.J. Kimble, Opt. Lett. **17**, 640 (1992)
5 G.D. Boyd, D.A. Kleinman, J. Appl. Phys. **39**, 3597 (1968)
6 T.W. Hänsch, B. Couillaud, Opt. Commun. **35**, 441 (1980)
7 All crystal data taken from SNLO program by Sandia National Laboratories
8 L. Kovács, K. Polgár, A. Péter, R. Capelletti, Mikrochim. Acta Suppl. **14**, 523 (1997)

VOLUME 93, NUMBER 4 PHYSICAL REVIEW LETTERS week ending 23 JULY 2004

Quantum Dense Coding with Atomic Qubits

T. Schaetz, M. D. Barrett,* D. Leibfried, J. Chiaverini, J. Britton, W. M. Itano, J. D. Jost, C. Langer, and D. J. Wineland

Time and Frequency Division, NIST, Boulder, Colorado 80305-3328, USA

(Received 27 April 2004; published 22 July 2004)

We report the implementation of quantum dense coding on individual atomic qubits with the use of two trapped $^9Be^+$ ions. The protocol is implemented with a complete Bell measurement that distinguishes the four operations used to encode two bits of classical information. We measure an average transmission fidelity of 0.85(1) and determine a channel capacity of 1.16(1).

DOI: 10.1103/PhysRevLett.93.040505 PACS numbers: 03.67.Lx, 32.80.Qk

Quantum dense coding [1] enables the communication of two bits of classical information with the transmission of one quantum bit or "qubit" (two-level quantum system). Two parties, Alice and Bob, each hold one qubit of a maximally entangled pair that has been previously prepared and distributed. With this starting point, Bob applies one of four possible unitary operations (each identified with the states of two classical bits) to his qubit and sends it to Alice. Alice then performs a Bell measurement [2] of both qubits; the outcomes of these measurements tell her which of the four operations Bob applied and the corresponding two-bit classical number.

Some of the elements of this protocol were first demonstrated in optics, where the qubit states were represented by a photon's states of polarization [3]. The protocol was also simulated in nuclear magnetic resonance using temporal averaging [4]. Dense coding has been investigated theoretically [5–7] and experimentally [8,9] in the context of continuous variables. It has also been considered for more than two entangled bits [10–14] or entangled degrees of freedom [15], but here we limit our discussion to the case of two qubits.

In addition to the communication applications, implementation of the protocol serves as a benchmark for comparison of quantum information processing (QIP) in different physical realizations [16]. For trapped-ion QIP, it tests the viability of specific tools required for large-scale processing [17,18], including the ability to separate ion qubits and individually detect them. From a significantly different perspective, it can also be viewed as a demonstration of increased efficiency for determination of quantum dynamics using QIP. For example, Ref. [19] shows that the optimal way to estimate the effect of a black box (here a rotation operator) on one qubit, given only one use of the box, is to apply it to one qubit of a maximally entangled pair and measure both qubits in a Bell-state basis (see also Ref. [20]). This strategy coincides with the dense-coding protocol on two qubits.

We implement the basic protocol [1] using two trapped atomic ion qubits. We realize it on demand, without the need for postselection of data, and with the ability to transfer and detect all four states corresponding to Bob's two bits of classical information. Since the experiment was implemented in one location, it is not useful for long-distance communication, although it could be extended to this purpose with the use of efficient atom-photon coupling [21,22]. In our implementation (outlined in Fig. 1), after the pair of entangled qubits is prepared, we let Bob use the experimental apparatus first to encode his qubit; he then turns over the apparatus to Alice so she can decode the message using Bob's and her qubit.

The qubits are composed of the $|F = 2, M_F = -2\rangle$ and $|F = 1, M_F = -1\rangle$ ground-state hyperfine levels of $^9Be^+$, labeled $|\downarrow\rangle$ and $|\uparrow\rangle$, respectively, where we use the formal equivalence between a two-level system and a spin-$\frac{1}{2}$ magnetic moment in a magnetic field (Bloch-vector representation) [23,24]. The ions are confined in a multizone linear rf-Paul trap similar to the one described in [25]. The ions are located on the axis of the trap structure, which we call the z direction. In a given trap zone, the

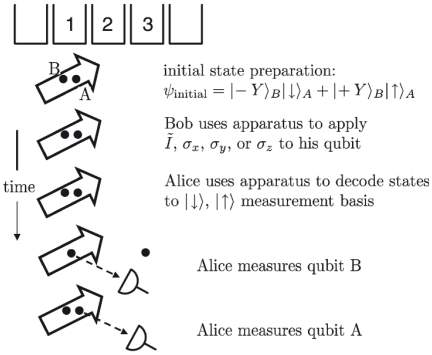

FIG. 1. Schematic diagram of the dense-coding implementation using atomic qubits. In the top part of the figure, the trap zones used in the experiment (not to scale) are designated with numbers. The z axis of the trap is parallel to the horizontal direction in the figure. The large arrows indicate schematically the laser beams used to implement the various operations. The dashed arrows indicate laser-induced fluorescence that is detected to determine the state of each ion ($|\downarrow\rangle$ fluoresces, $|\uparrow\rangle$ does not). To facilitate separate detection of qubits A and B, qubit B is measured first, then transferred to a nonfluorescing state, followed by detection of qubit A.

VOLUME 93, NUMBER 4 PHYSICAL REVIEW LETTERS week ending 23 JULY 2004

ions' motion along z can be described by normal modes corresponding to the center-of-mass (frequency $\omega_{\text{c.m.}}$) and "stretch" ($\omega_{\text{STR}} = \sqrt{3}\omega_{\text{c.m.}}$) modes, where the mode amplitudes are equal and in the same or opposite directions, respectively [26]. We adjust the trap potential to make $\omega_{\text{c.m.}}/2\pi = 3.71$ MHz, corresponding to a separation of 3.76 μm between ions. At the start of each experiment, the ions are laser cooled to the motional ground state and optically pumped into the internal states $|\downarrow\rangle_1 \otimes |\downarrow\rangle_2$ [26].

To implement the dense-coding protocol, we will need to realize single qubit gates (rotations) and a two-qubit universal logic gate [2]. For a single-qubit gate on ion i, the states $|\downarrow\rangle_i$ and $|\uparrow\rangle_i$ are coupled with stimulated Raman transitions excited with two laser beams (designated "blue" and "red" to indicate their relative detuning) that overlap both ions [27]. The k vectors of these beams are oriented such that $\vec{k}_{\text{blue}}$ is approximately perpendicular to $\vec{k}_{\text{red}}$ and $\Delta\vec{k} \equiv \vec{k}_{\text{blue}} - \vec{k}_{\text{red}} \simeq \sqrt{2}|\vec{k}_{\text{blue}}|\hat{z} \equiv \hat{z}2\pi/\lambda_{\text{eff}}$, where λ_{eff} is the effective wavelength of the Raman transition. By tuning the difference frequency of the laser beams to $(\omega_{\text{blue}} - \omega_{\text{red}})/2\pi = \omega_0/2\pi = (E_\uparrow - E_\downarrow)/h \simeq 1.25$ GHz, we implement the rotation of the qubit state on the Bloch sphere

$$R_i(\theta, \phi_i) \equiv \begin{pmatrix} \cos\frac{\theta}{2} & -ie^{-i\phi_i}\sin\frac{\theta}{2} \\ -ie^{+i\phi_i}\sin\frac{\theta}{2} & \cos\frac{\theta}{2} \end{pmatrix}, \quad (1)$$

where we use the conventions

$$|\downarrow\rangle \equiv \begin{pmatrix} 0 \\ 1 \end{pmatrix}, \qquad |\uparrow\rangle \equiv \begin{pmatrix} 1 \\ 0 \end{pmatrix}. \quad (2)$$

The angle θ is proportional to the duration of the Raman pulse. The phase factor $\phi_i = \Delta\vec{k}\cdot\vec{x}_i + \phi_{\text{blue},i} - \phi_{\text{red},i}$ is the phase difference between the Raman beams at the position $\vec{x}_i$ of the ith ion.

To implement a universal logic gate between the ions, the Raman laser beams can be configured to apply state-dependent optical dipole forces. We choose the polarizations of the beams so that these forces along the z direction are related by $\vec{F}_\downarrow = -2\vec{F}_\uparrow$ [28,29]. We adjust the frequency difference between the Raman beams and therefore the frequency of the optical dipole force to be equal to $\omega_{\text{STR}} + \delta$ ($|\delta| \ll \omega_{\text{STR}}$). With the above choice of $\omega_{\text{c.m.}}$, the ions are separated by a distance $17.0 \times \lambda_{\text{eff}}$, so that if the ions are in the opposite state, the dipole force can (off resonantly) excite the ions' stretch mode. (If they are in the same state, the stretch mode is not excited.) By applying these forces for a gate time $\tau_G = 2\pi/\delta$ and adjusting their magnitude appropriately, we realize a geometric phase gate G_ϕ, which implements the operation [29]

$$\begin{aligned} G_\phi : a|\downarrow\rangle|\downarrow\rangle + b|\downarrow\rangle|\uparrow\rangle + c|\uparrow\rangle|\downarrow\rangle + d|\uparrow\rangle|\uparrow\rangle \\ \rightarrow a|\downarrow\rangle|\downarrow\rangle + ib|\downarrow\rangle|\uparrow\rangle + ic|\uparrow\rangle|\downarrow\rangle + d|\uparrow\rangle|\uparrow\rangle. \end{aligned} \quad (3)$$

We will need to implement single-qubit rotations on one ion without changing the state of the other ion; this can be accomplished in one trap zone even though the Raman beams overlap both ions. To see how this is done, consider the following example [18,30]. Suppose we want to prepare the state $(|\downarrow\rangle_1 + |\uparrow\rangle_1) \otimes |\downarrow\rangle_2$ from the state $|\downarrow\rangle_1|\downarrow\rangle_2$ (for simplicity we omit normalization factors). We first apply a Raman pulse acting equally on both ions to implement the rotations $R_1(\frac{\pi}{4}, -\frac{\pi}{2}) \otimes R_2(\frac{\pi}{4}, -\frac{\pi}{2})$. The spins rotate into a state represented pictorially by $|\searrow\rangle_1|\searrow\rangle_2$. The spacing of the ions is now changed by $\lambda_{\text{eff}}/2$. A second Raman pulse of the same duration is applied to both qubits such that the laser phase on qubit 1 is the same, but because of the change in ion separation, the phase on qubit 2 is shifted by π. This carries out the operation $R_1(\frac{\pi}{4}, -\frac{\pi}{2}) \otimes R_2(\frac{\pi}{4}, +\frac{\pi}{2})$. Whence, qubit 2 is rotated back into its initial state while qubit 1 completes a $\theta = \frac{\pi}{2}$ rotation. Pictorially, application of the second Raman pulse implements the transformation $|\searrow\rangle_1|\searrow\rangle_2 \rightarrow |\rightarrow\rangle_1|\downarrow\rangle_2 = (|\downarrow\rangle_1 + |\uparrow\rangle_1) \otimes |\downarrow\rangle_2$. Generalizing this, we can apply the Pauli operators σ_x, σ_y, and σ_z to ion 1, which, up to global phase factors, correspond to the operators $R_1(\pi, 0)$, $R_1(\pi, \frac{\pi}{2})$, and $R_1(\pi, 0)R_1(\pi, \frac{\pi}{2})$ respectively.

Finally, we will need to detect both qubits individually in the $|\downarrow\rangle$, $|\uparrow\rangle$ basis. This is accomplished through state-dependent laser scattering ($|\downarrow\rangle$ fluoresces strongly, while $|\uparrow\rangle$ has negligible fluorescence [30]). We first separate qubits 1 and 2 into different trap zones as described in Ref. [25]. Qubit 1 remains in trap zone No. 1 (Fig. 1), while qubit 2 is transferred to an auxiliary zone (zone No. 3 in Fig. 1) located approximately 340 μm away. After detection of the state of qubit 1 [31], it is optically pumped to the state $|\downarrow\rangle_1$, and then a π pulse [$R_1(\pi, 0)$] is applied to transfer it to the state $|\uparrow\rangle_1$. Following this, both qubits are recombined in zone 1 and detected. Since qubit 1 does not fluoresce, we detect the state of ion 2 with less than 1% error due to the presence of ion 1.

With these tools, the dense-coding protocol is implemented as follows (Fig. 1). We first need to prepare the entangled state ψ_{initial} that Bob and Alice initially share. We let qubits 1 and 2 correspond to Bob's and Alice's qubits, respectively. We apply the operator $R_B(\frac{\pi}{2}, -\frac{\pi}{2}) \otimes R_A(\frac{\pi}{2}, -\frac{\pi}{2})$ followed by application of G_ϕ to the state $|\downarrow\rangle_B|\downarrow\rangle_A$. This leads to the transformations

$$\begin{aligned} |\downarrow\rangle_B|\downarrow\rangle_A \rightarrow (|\downarrow\rangle_B + |\uparrow\rangle_B)(|\downarrow\rangle_A + |\uparrow\rangle_A) \rightarrow \\ |-Y\rangle_B|\downarrow\rangle_A + |+Y\rangle_B|\uparrow\rangle_A \equiv \psi_{\text{initial}}, \end{aligned} \quad (4)$$

where $|\pm Y\rangle$ correspond to Bloch eigenvectors aligned along the $\pm y$ directions with the properties $\sigma_y|\pm Y\rangle = \pm|\pm Y\rangle$. Therefore, the entangled state shared by Alice and Bob is a maximally entangled state, but for experimental convenience, they choose different bases for their initial states.

VOLUME 93, NUMBER 4 PHYSICAL REVIEW LETTERS week ending 23 JULY 2004

Bob, using the method of individual ion addressing described above, encodes his qubit with two classical bits of information by applying one of four operators according to the identification scheme: $(00) \leftrightarrow \tilde{I}_B$, $(01) \leftrightarrow \sigma_{yB}$, $(10) \leftrightarrow \sigma_{zB}$, and $(11) \leftrightarrow \sigma_{xB}$, where $\tilde{I}$ is the identity operator. Now, Bob turns over his bit and the rest of the apparatus to Alice.

To decode the message that Bob encoded on his qubit, Alice takes both qubits and applies the operator G_ϕ followed by the operator $R_B(\frac{\pi}{2}, -\frac{\pi}{2}) \otimes R_A(\frac{\pi}{2}, -\frac{\pi}{2})$. Finally, Alice measures the states of each qubit as described above. Ideally, she finds the correlations between the detected states and Bob's two bit classical message according to $|\downarrow\rangle_B|\downarrow\rangle_A \leftrightarrow (00)$, $|\downarrow\rangle_B|\uparrow\rangle_A \leftrightarrow (01)$, $|\uparrow\rangle_B|\downarrow\rangle_A \leftrightarrow (10)$, and $|\uparrow\rangle_B|\uparrow\rangle_A \leftrightarrow (11)$.

The approximate durations of the various pulses in the experiment were as follows: $\pi/2$ $[R(\frac{\pi}{2}, \phi)]$ pulses, 0.7 μs; π pulses, 1.4 μs; G_ϕ, 10 μs; and delays between pulses were a minimum of 2 μs (to avoid pulse overlaps from switching transients). The duration to change the separation of the ions by $\lambda_{\text{eff}}/2$ was 11 μs, the duration to separate or recombine ions for individual detection was 250 μs, the duration for fluorescence detection of each ion was 400 μs, and the time to recool and optically pump the ions before each experiment was about 1 ms.

In practice, each of the above operations is imperfect. These imperfections are caused primarily by intensity fluctuations of both Raman beams, drifts in the detuning δ over the duration of many experiments, imperfect initial state preparation, and imperfect detection. A serious problem is caused by fluctuations of the ambient magnetic field. The qubit spin flip frequency $\omega_0/2\pi$ has magnetic field dependence of 2.1 MHz/G; therefore, field fluctuations (up to 10 mG) can cause dephasing of the qubit states when averaged over many experiments. However, these field fluctuations occur on a time scale that is long compared to the duration between application of the first common $\pi/2$ pulse and the time of ion separation for detection, so we may employ the technique of spin echoes [24] to correct the dephasing. These $R_B(\pi, 0) \otimes R_A(\pi, 0)$ spin-echo pulses were inserted between the G_ϕ operations and the application of Bob's qubit encoding. They do not perfectly correct for field drifts due to the finite time for Bob to apply his operator, but they help suppress these dephasing effects. Aside from adding global phase factors, the spin-echo pulses do not change the protocol. Figure 1 schematically outlines the experiment, omitting the spin-echo pulses.

For each choice of Bob's operator, we measure the fidelity of the actual output state relative to the ideally expected output state

$$F = \langle \psi_{\text{ideal}} | \rho_{\text{out}} | \psi_{\text{ideal}} \rangle, \tag{5}$$

where ρ_{out} is the density matrix of the output state. These data are included (in bold lettering) in Table I, where we also display the probabilities for detecting all other (undesired) states. Using the data from Table I, we calculate the channel capacity C with the use of Eq. (12.67) from Ref. [2], and find $C = 1.16(1)$. In the ideal situation, where no errors occur, we would find $C = 2.00$, corresponding to a channel capacity of two bits, as expected. In [3], two of Bob's operations could not be distinguished, so that only three states of classical information could be transferred (a "trit" vs two bits). Under ideal conditions, this would give a channel capacity of 1.58 bits. Our value for the channel capacity is only slightly above the value of 1.13 found in Ref. [3] for the case of trits, apparently due to the higher fidelity for each of the three detected operations [32]. However, in that experiment, only those transmissions where the appropriate coincidences were detected were used in the data analysis, whereas here, Table I entries are based on all experiments, without postselection.

TABLE I. Correlations between Bob's applied operator (top row) and Alice's state measurements of both qubits (left column). The entries correspond to the probabilities measured by Alice for each basis state. Ideally, the entries in bold should equal 1 and all other entries should equal zero.

	$\tilde{I}$	σ_y	σ_z	σ_x
$\|\downarrow\rangle_B\|\downarrow\rangle_A$	**0.84(2)**	0.07(1)	0.08(1)	0.02(1)
$\|\uparrow\rangle_B\|\downarrow\rangle_A$	0.07(1)	0.01(1)	**0.84(1)**	0.04(1)
$\|\downarrow\rangle_B\|\uparrow\rangle_A$	0.06(1)	**0.84(1)**	0.04(1)	0.08(1)
$\|\uparrow\rangle_B\|\uparrow\rangle_A$	0.03(1)	0.08(1)	0.04(1)	**0.87(1)**

In summary, we have implemented the quantum dense-coding protocol on atomic qubits using two trapped $^9Be^+$ ions. For the two bits of classical information encoded using quantum operations on a single qubit, we find an average transmission fidelity $\langle F \rangle = 0.85(1)$. We also determine a channel capacity $C = 1.16(1)$, which exceeds that which could be obtained in a perfect experiment (without entanglement) where a quantum bit is used to transmit classical information ($C = 1$). The techniques demonstrated here may eventually be useful for communication, but perhaps more significantly in the near term, they will facilitate the implementation of scalable quantum computation using trapped ions [17,33]. In the future, use of smaller trap electrodes to speed up ion separation and gate operations, coupled with better detection, should significantly increase the speed of such protocols.

This work was supported by ARDA/NSA under Contract No. MOD 7171.04 and by NIST. We thank J. Bollinger and P. Schmidt for helpful comments on the manuscript. T. S. acknowledges a Deutsche Forschungsgemeinschaft research grant. This paper is a contribution of the National Institute of Standards and Technology, not subject to U. S. copyright.

*Present Address: Physics Department, Otago University, New Zealand.

[1] C. H. Bennett and S. J. Wiesner, Phys. Rev. Lett. **69**, 2881 (1992).
[2] M. A. Nielsen and I. L. Chuang, *Quantum Computation and Quantum Information* (Cambridge University Press, Cambridge, 2000), 1st ed.
[3] K. Mattle, H. Weinfurter, P. G. Kwiat, and A. Zeilinger, Phys. Rev. Lett. **76**, 4656 (1996).
[4] X. Fang *et al.*, Phys. Rev. A **61**, 022307 (2000).
[5] M. Ban, J. Opt. B Quantum Semiclassical Opt. **1**, L9 (1999).
[6] S. L. Braunstein and H. J. Kimble, Phys. Rev. A **61**, 042302 (1999).
[7] T. C. Ralph and E. H. Huntington, Phys. Rev. A **66**, 042321 (2002).
[8] X. Li *et al.*, Phys. Rev. Lett. **88**, 047904 (2002).
[9] J. Mizuno, K. Wakui, A. Furusawa, and M. Sasaki, quant-ph/0402040.
[10] S. Bose, V. Vedral, and P. L. Knight, Phys. Rev. A **57**, 822 (1998).
[11] J. C. Hao, C. F. Li, and G. C. Guo, Phys. Rev. A **63**, 054301 (2001).
[12] H. J. Lee, D. Ahn, and S. W. Hwang, Phys. Rev. A **66**, 024304 (2002).
[13] A. Wójcik and A. Grudka, Phys. Rev. A **68**, 016301 (2003).
[14] O. Akhavan and A. T. Rezakhani, Phys. Rev. A **68**, 016302 (2003).
[15] K. Shimizu, N. Imoto, and T. Mukai, Phys. Rev. A **59**, 1092 (1999).
[16] See, for example, http://qist.lanl.gov/
[17] D. J. Wineland *et al.*, J. Res. Natl. Inst. Stand. Technol. **103**, 259 (1998).
[18] D. Kielpinski *et al.*, Science **291**, 1013 (2001).
[19] A. Acín, E. Jané, and G. Vidal, Phys. Rev. A **64**, 050302 (2001).
[20] A. M. Childs, J. Preskill, and J. Renes, J. Mod. Opt. **47**, 155 (2000).
[21] J. I. Cirac, P. Zoller, H. J. Kimble, and H. Mabuchi, Phys. Rev. Lett. **78**, 3221 (1997).
[22] In this context, we note that an eavesdropper intercepting the qubit sent from Bob to Alice could not gain any knowledge about the encoded message without access to the second qubit in the entangled pair. This would hold even for imperfect entanglement, as long as the imperfection is unbiased as, for example, a depolarizing error [M. A. Nielsen (private communication)].
[23] R. P. Feynman, F. L. Vernon, and R. W. Hellwarth, J. Appl. Phys. **28**, 49 (1957).
[24] L. Allen and J. H. Eberly, *Optical Resonance and Two-Level Atoms* (Dover, Mineola, NY, 1987).
[25] M. A. Rowe *et al.*, Quantum Inf. Comput. **2**, 257 (2002).
[26] B. E. King *et al.*, Phys. Rev. Lett. **81**, 1525 (1998).
[27] The laser beam waists (approximately equal to the beam diameters) at the ions were approximately 30 μm, and the beam positions were adjusted to give equal intensity on both ions.
[28] D. J. Wineland *et al.*, Philos. Trans. R. Soc. London, Ser. A **361**, 1349 (2003).
[29] D. Leibfried *et al.*, Nature (London) **422**, 412 (2003).
[30] M. A. Rowe *et al.*, Nature (London) **409**, 791 (2001).
[31] In our previous experiments [25], the separation was achieved with only a 95% success probability and the motion was excited substantially, leading to poor detection efficiency. Aided by a smaller separation electrode in the current apparatus (100 μm wide vs 800 μm wide in Ref. [25]), separation was accomplished with no detected failures and the small heating (about ten quanta) led to more efficient state detection.
[32] From Ref. [3], we estimate the fidelity for the three cases using $F_i = (S/N)_i/[(S/N)_i + 1]$ and find $F_{|\Psi^+\rangle} \simeq 0.94$, $F_{|\Psi^-\rangle} \simeq 0.93$, and $F_{|\Phi^-\rangle} \simeq 0.90$.
[33] D. Kielpinski, C. Monroe, and D. J. Wineland, Nature (London) **417**, 709 (2002).